Titre: Title:	Synthesis and Chemical and Morphological Characterization of Ruthenium-Based Nanoparticles
Auteur: Author:	Roksana Bavandsavadkouhi
Date:	2016
Type:	Mémoire ou thèse / Dissertation or Thesis
Référence: Citation:	Bavandsavadkouhi, R. (2016). Synthesis and Chemical and Morphological Characterization of Ruthenium-Based Nanoparticles [Thèse de doctorat, École Polytechnique de Montréal]. PolyPublie. https://publications.polymtl.ca/2402/

URL de PolyPublie: PolyPublie URL:	https://publications.polymtl.ca/2402/
Directeurs de recherche: Advisors:	Edward Sacher, & Arthur Yelon
Programme: Program:	Génie métallurgique

UNIVERSITÉ DE MONTRÉAL

SYNTHESIS AND CHEMICAL AND MORPHOLOGICAL CHARACTERIZATION OF RUTHENIUM-BASED NANOPARTICLES

ROKSANA BAVANDSAVADKOUHI

DÉPARTEMENT DE GÉNIE PHYSIQUE

ÉCOLE POLYTECHNIQUE DE MONTRÉAL

THÈSE PRÉSENTÉE EN VUE DE L'OBTENTION

DU DIPLÔME DE PHILOSOPHIAE DOCTOR

(GÉNIE MÉTALLURGIQUE)

DÉCEMBRE 2016

UNIVERSITÉ DE MONTRÉAL

ÉCOLE POLYTECHNIQUE DE MONTRÉAL

Cette thèse intitulée :

SYNTHESIS AND CHEMICAL AND MORPHOLOGICAL CHARACTERIZATION OF RUTHENIUM-BASED NANOPARTICLES

présentée par : BAVANDSAVADKOUHI Roksana

en vue de l'obtention du diplôme de : Philosophiae Doctor

a été dûment acceptée par le jury d'examen constitué de :

M. MARTINU Ludvik, Ph. D., président

M. SACHER Edward, Ph. D., membre et directeur de recherche

M. YELON Arthur, Ph. D., membre et codirecteur de recherche

M. MEUNIER Michel, Ph. D., membre

M. GUAY Daniel, Doctorat, membre externe

DEDICATION

To my parents, Zohreh and Vandad

ACKNOWLEDGEMENTS

This thesis has been completed with the support and encouragement of numerous people. It is my pleasure to express gratitude to all those who contributed in many ways to make it an unforgettable experience for me.

First and foremost, I would like to express my utmost appreciation and gratitude to Professor Edward Sacher and Professor Arthur Yelon for their unconditioned support and dedicated time. Their guidance helped me in all the time of research and writing of this thesis. I could not have imagined having better advisors and mentors for my PhD study.

Professor Edward Sacher, the director of my thesis, has trusted me in my research career over the past four years and has given me the honor of working with him. Without his generous support, scientific insight, and invaluable guidance, this thesis would have been impossible. During the course of my PhD studies, I enjoyed the pleasure of being his student and benefited from his enlightening supervision, encouragement, and dedication.

Professor Arthur Yelon was my co-director, to whom I would like to express my gratitude for his contributions and priceless help. Under his guidance, I successfully overcame many difficulties and also enjoyed his incredible knowledge and insight, constructive criticism and his extensive discussions around my research work.

Mme. Josianne Lefebvre, research associate in the “Laboratoire pour l'Analyse de la Surface des Matériaux” (LASM), has always inspired me with her scientific approach, enthusiasm, and motivation. I had the pleasure of working with her during these years and her continuous encouragement helped me face the different obstacles that I encountered during my research. I extend my sincere thanks to all members of the Department of Engineering Physics, and all those who contributed directly or indirectly to the dissertation. In particular, I wish to thank Lyne Dénommé and Elisabeth Delépine for helping me to resolve administrative affairs.

Moreover, I would like to express my appreciation to the members of my thesis exam committee, Professors Ludvik Martinu, Michel Meunier, Daniel Guay, and Michael Buschmann, for their valuable time and their encouraging comments.

Several people have helped me with my experimental research studies. I especially thank Jean-Phillipe Massé, research associate in the “Centre de Caractérisation Microscopique des

Matériaux" $(CM)^2$, for not only implementing the TEM measurements, but also kindly responding my scientific questions. My gratefulness goes to Patricia Moraille, research associate at the "Laboratoire de Caractérisation des Matériaux", Phillipe Plamondon, research associate at $(CM)^2$ for their advice and help. I thank Professor Remo A. Masut, responsible at Laboratoire D'épitaxie et de Caractérisation de Semi-Conducteurs Composés for letting me use his equipment, and Nima Nateghi, for showing me how to use it. I also thank Professor Gianluigi Botton, the scientific director at the Canada Research Chair in Electron Microscopy of Nanoscale Materials at McMaster University, and Professor Shuhui Sun, at the "Institut National de la Recherche Scientifique", INRS, for their insightful ideas and contribution in our collaborative research studies. Finally, I thank Drs. Gaixia Zhang (INRS) and Long Chen (PNNL) for their helpful advice.

I express my gratefulness to Sorouch Hafezian, for helping me with French transcriptions and scientific discussions. I warmly thank my friends, Laura Karina Mireles, Qiliang Wei, Simon Loquai, Jaber Shabanian, Laleh Dashtban, Maryam Fereydoon, Hamed Jazayeri, Ali Seifi, Marzieh Ghasemi, and Saman Choubak, for their support and presence during my PhD studies. Further, my special thanks go to my colleagues with whom I shared an office, Fabrice Pougoum, Jincheng Qian, and Erika Herrera.

Last but not least, I would especially like to express my deepest gratitude to my husband, Hossein, who has always supported me during stressful and difficult moments. You should know that your support and encouragement was worth more than I can express on paper. I express my gratitude toward my family. My brother, Behnam, and my sister-in-law, Zeinab, and my lovely niece, Benita, have always encouraged me with their support and wishes. My profound appreciation goes to my parents, Zohreh and Vandad, for their unconditioned love and everlasting support. I am utterly indebted to my beloved parents for they have been nourishing my insatiable desire for knowledge throughout my life. You made me live the most unique, magic, and carefree childhood that has made me who I am now! I simply cannot thank them enough.

The work, presented in this thesis, was supported by the Natural Sciences and Engineering Research Council (NSERC) of Canada. I gratefully acknowledge this support.

RESUME

Le développement de sources d'énergie verte, renouvelable avec des rendements élevés, sont nécessaires comme alternatives aux combustibles fossiles. Les piles à combustible à membrane échangeuse de protons et les piles à combustible à méthanol direct sont des candidats prometteurs pour les sources d'énergie fixes et portables. Cependant, l’électrocatalyseur le plus couramment utilisé, le platine (Pt), est dispendieux et la réserve mondiale est limité. En outre, la cinétique des réactions des réductions de l'oxygène et l'oxydation du méthanol sur Pt sont lentes, ce qui entraîne une perte de performance. Par conséquent, trouver un électrocatalyseur alternatif ou réduire la charge de Pt par alliage, et l'amélioration de la performance catalytique, sont d'une grande importance dans la commercialisation de technologies de piles à combustible.

Parmi les différents candidats pour les catalyseurs contenant une faible concentration de Pt, les alliages bimétalliques PtRu peuvent répondre aux exigences de performance, tout en réduisant les coûts et en augmentant la durabilité. Notre but est de synthétiser ces catalyseurs en utilisant la méthode de dépôt en phase vapeur, et de réaliser *in-situ* et *ex-situ* des analyses pour déterminer en détail la structure et la chimie de la surface, où se fait la catalyse. Par conséquent, cette thèse est divisée en deux phases : d'abord, la préparation et la caractérisation de pures nanoparticules de ruthénium (Ru NPs) déposés sur graphite pyrolytique hautement orienté (HOPG). En combinant cette information avec nos informations précédemment obtenu sur le Pt [1], la deuxième phase comprend la préparation et la caractérisation des alliages de PtRu NPs déposées sur le même substrat.

Les Ru NPs fonctionnent comme des catalyseurs efficaces pour des réactions spécifiques, telles que la méthanation et la synthèse de Fischer-Tropsch [2]. Dans la première phase de cette thèse, il est notre but de présenter une caractérisation physique et chimique des surfaces, par spectroscopie de photoélectrons par rayons X (XPS), sensible à la surface, et en utilisant la technique d'analyse des composantes de pics symétriques développée dans notre laboratoire, pour révéler les composants précédemment obscurcis.

Les Ru NPs étaient déposés par évaporation (0,25 à 1,5 nm d’épaisseur nominale) sur HOPG. Notre utilisation de l’analyse de composant par pics symétriques par XPS a révélé des informations détaillées sur des pics, non préalablement identifiées, d’oxyde en surface initialement formée, ainsi que sur la structure électronique de la bande de valence et sa variation

avec la taille des nanoparticules, une information qui est d'une grande importance dans l'utilisation de ces NP en catalyse.

Chacun des spectres du Ru caractérisés par XPS (3d, 3p et 3s) contient trois composantes symétriques, ainsi que des composantes O1s de deux oxydes métalliques, montrant un oxyde assez complexe initialement formé. Les spectres de la bande de valence du Ru (4d et 5s) démontrent clairement une perte de métallicité, une augmentation simultanée de l'écart Kubo, et un transfert significatif de la densité d'électrons de valence du 4d aux 5s orbitales (connu sous le nom d'électron spill-over), quand le dépôt diminue en dessous de 0,5 nm.

En plus des caractérisations des surfaces par XPS, une indication de la morphologie a été obtenue à partir de la microscopie électronique en transmission (TEM). Les microphotographies TEM en fonction du taux de dépôt montrent qu'à un taux qui ne permet pas la dissipation de l'énergie de condensation des NP, celles-ci, bien qu'initialement séparées sont capables de diffuser latéralement, de s'agréger et à coalescer de façon partielle. Cela indique une liaison faible des NPs sur le substrat HOPG. De plus, le carbure de Ru se forme à des taux faibles et élevée pour des épaisseurs supérieures à 0,25 nm, dû à la réaction des NPs de Ru réagissant avec la vapeur d'hydrocarbure résiduel, sous l'influence de la chaleur de condensation libérée lors du dépôt du Ru, et non pas par réaction de Ru avec le substrat d'HOPG.

Dans la deuxième phase de cette thèse, nous avons caractérisé la formation des alliages PtRu NPs (1:1), déposées sur HOPG, en utilisant XPS et par la spectroscopie de masses d'ion secondaire à mesure de temps de vol *in-situ*, angle élevé annulaire et champ sombre / microscopie électronique à balayage par transmission, et spectroscopie de perte d'énergie des électrons *ex situ*. Nous avons utilisé trois ordres de dépôt de métal : Pt déposé sur Ru, Ru déposé sur Pt et les deux métaux déposés en même temps, puis suivi les évolutions des alliages en fonction de la température de recuit. Les spectres C1s, O1s, Ru3d et Pt4f niveau de cœur et le Ru4d, 5s et Pt5d, 6s niveau de valence ont été employés pour décrire les interactions d'alliage entre les métaux. Pour toutes les méthodes de dépôt, le Ru diffuse à la surface des NPs à travers le Pt, et non l'inverse. Certains chercheurs ont affirmé que le Pt [3-5], un autre a montré que le Ru [6, 7], se trouve à la surface des NPs. Cette incohérence a présenté un défi pour déterminer la structure optimale. Dans notre étude, chacune des méthodes de préparation a produit une structure de surface qui diffère de celles des autres, même après un recuit prolongé à des températures supérieures à 700 ° C, ce qui suggère pourquoi il y a une telle confusion dans la littérature concernant la caractérisation physico-chimique de PtRu NPs.

ABSTRACT

The development of green, renewable energy sources, with high efficiencies, is required as an alternative for fossil fuel. Both proton exchange membrane and direct methanol fuel cells are promising candidates for stationary and portable power sources. However, the most commonly used electrocatalyst, Platinum (Pt), is expensive and the world's supply is limited. In addition, both the oxygen reduction and methanol oxidation reactions kinetics on Pt are sluggish, which results in performance loss. Therefore, finding an alternative electrocatalyst or reducing the Pt loading by alloying, and improving catalytic performance, are of great importance in the commercialization of fuel cell technologies.

Among various low-Pt catalyst candidates, bimetallic PtRu nanoparticles (NPs) may well meet performance requirements, along with reducing cost and increasing durability. It is our aim to synthesize such catalysts, using vapor deposition, and to carry out *in-situ* and *ex-situ* analyses to determine the surface structure and chemistry in detail, because the surface is where catalysis takes place. Hence, this thesis is divided into two phases: first, the preparation and characterization of pure Ruthenium (Ru) nanoparticles deposited onto highly oriented pyrolytic graphite (HOPG). By combining this information with our previously obtained information of pure Pt [1], the second phase involves the preparation and characterization of PtRu NPs deposited onto the same substrate.

Ru NPs function as effective catalysts in specific reactions, such as methanation and Fischer-Tropsch syntheses [2]. In the first phase of this thesis, it is our purpose to physicochemically characterize their surfaces, at which catalysis occurs, by surface-sensitive X-ray photoelectron spectroscopy (XPS), using the symmetric peak component analysis technique developed in our laboratory, to reveal previously obscured components.

Ru NPs were deposited by evaporation (0.25-1.5 nm nominal deposition range) onto HOPG. Our use of symmetric peak component XPS analysis has revealed detailed information on a previously unidentified surface oxide initially formed, as well as on the valence electronic structure and its variation with nanoparticle size, information that is of potential importance in the use of these NPs in catalysis.

Each of the several Ru core XPS spectra characterized (3d, 3p and 3s) was found to be composed of three symmetric components, of which two were metal oxide O1s components, giving evidence of a rather complex, previously unidentified oxide that is initially formed. The Ru valence band (4d and 5s) spectra clearly demonstrate a loss of metallicity, a simultaneous increase of the Kubo gap, and an abrupt transfer in valence electron density from the 4d to the 5s orbitals (known as electron spill-over), as the deposition is decreased below 0.5 nm.

In addition to their surfaces being characterized by XPS, an indication of morphology was obtained from transmission electron microscopy (TEM). TEM photomicrographs, as a function of deposition rate, show that, at a rate that gives insufficient time for the NP condensation energy to dissipate, the initially well-separated NPs are capable of diffusing laterally, aggregating and partially coalescing. This indicates weak NP bonding to the HOPG substrate. Carbide is formed, at both high and low deposition rates, at Ru deposition thicknesses greater than 0.25 nm, as Ru NPs react with residual hydrocarbon vapor, under the influence of the heat of condensation released on Ru deposition, and not by Ru reaction with the HOPG substrate.

In the second phase of this thesis, we characterized the formation of 1:1 PtRu NPs, deposited onto HOPG, using *in-situ* XPS and time-of-flight secondary ion mass spectrometry, *ex-situ* high-angle annular dark-field/scanning transmission electron microscopy, and electron energy loss spectroscopy. We used three different orders of metal deposition: Pt deposited onto Ru, Ru deposited onto Pt and both metals deposited simultaneously, and then followed the evolutions of the alloys as a function of annealing temperature. The C1s, O1s, Ru3d and Pt4f core level and the Ru4d,5s and Pt5d,6s valence level spectra were employed to describe the alloying interactions between the metals. For all deposition methods, Ru diffused to the NP surface through the Pt, and not the reverse. Although some researchers claimed that Pt was found at the surface [3-5], some other proposed that it was Ru [6, 7]. This inconsistency has presented a challenge in determining the optimum structure. In our study, each of the preparation methods was found to produce a surface structure that differed from those of the others, even after prolonged annealing at temperatures over 700ºC, suggesting why there is such confusion in the literature concerning the physicochemical characterization of PtRu NPs.

TABLE OF CONTENTS

LIST OF TABLES

LIST OF FIGURES

LIST OF SYMBOLS AND ABBREVIATIONS

CO	Carbon monoxide
CNT	Carbon nanotube
CV	Cyclic voltammetry
DMFC	Direct methanol fuel cell
ESCA	Electron Spectroscopy for Chemical Analysis
E-beam	Electron beam
EDS (or EDX)	Energy Dispersive X-ray Spectroscopy
EELS	Electron energy loss spectroscopy
FWHM	Full width half maximum
FIB	Focused ion beam
HOPG	Highly oriented pyrolytic graphite
HAADF	High angle annular dark field
IMFP	Inelastic mean free path
MOR	Methanol oxidation reaction
NPs	Nanoparticles
OER	Oxygen evolution reaction
PEMFC	Proton exchange membrane fuel cells

PVD	Physical vapor deposition
STEM	Scanning transmission electron microscopy
SEM	Scanning electron microscopy
SCLS	Surface core level shift
TOF-SIMS	Time-of-Flight secondary ion mass spectrometry
TEM	Transmission electron microscopy
XPS	X-ray photoelectron spectroscopy

CHAPTER 1 INTRODUCTION AND ORGANIZATION OF THE THESIS

1.1 Proton Exchange Membrane Fuel Cells (PEMFC) & Direct Methanol Fuel Cells (DMFC)

The increase of environmental pollution challenges, fossil fuel depletion, the fluctuation of oil prices, and climbing global energy demand necessitate the alternative of efficient energy-converting devices, instead of fossil fuel. Over the last few years, this demand has been satisfied, to some extent, by using fuel cells, which are recognized as clean, silent, power sources with high efficiencies. These fuel cells have been proposed as appropriate power generators, which convert the chemical energy of fuel (such as hydrogen, methanol, ethanol, etc.) into electrical energy with minimal environmental pollution [8-10]. There are five different main categories of fuel cells, in which their classification is generally based on the electrolytes used. One of the best known, and used, is the proton exchange membrane fuel cell (PEMFC). This fuel cell uses hydrogen as a fuel and oxygen from the air as an oxidant. PEMFCs have high energy conversion efficiencies, good performance capabilities, and quick startup at low temperatures, which make them the most promising candidates for portable and transportation applications [10, 11]. The main components of fuel cells are anode, cathode, and electrolyte. In PEMFCs, at the anode, catalyst causes the hydrogen to split into H^+ and electrons. The positively charged hydrogen ions and electrons reach to the cathode by passing through the proton exchange membrane electrolyte and an external circuit, respectively. At the cathode, the electrons and H^+ combine with oxygen to produce water as the only final product [12]. The electrochemical reactions in both anode and cathode, along with the overall reaction are:

At the anode: $H_2 \rightarrow 2H^+ + 2e^-$

At the cathode: $\frac{1}{2} O_2 + 2H^+ + 2e^- \rightarrow H_2O$

Overall reaction: $H_2 + \frac{1}{2} O_2 \rightarrow H_2O$

The direct methanol fuel cell (DMFC) is a variation of the PEMFC, which has advantages over PEMFC systems. The DMFC uses methanol as a fuel, without the need of reforming reactions.

One of the drawbacks with PEMFC is the hydrogen fuel, due to difficulties related to its storage, transportation and infrastructure issues. Methanol is liquid at room temperature, making it easier and safer for storage and use in fuel cells. In addition, the methanol oxidation process in DMFCs transfers six electrons, while the hydrogen oxidation reaction in PEMFCs transfers only two electrons. This indicates that reactions in DMFCs produce three times as much energy as than those of in PEMFC [13, 14]. DMFCs, methanol is oxidized at the anode to produce carbon dioxide, while oxygen molecules from the air are reduced to OH^- at the cathode. Hence, water is produced by combining OH^- with the electrons and protons coming from the anode. The anodic, cathodic, and overall reactions in DMFCs are:

At the anode: $CH_3OH + H_2O \rightarrow CO_2 + 6H^+ + 6e^-$

At the cathode: $3/2\ O_2 + 6H^+ + 6e^- \rightarrow 3H_2O$

Overall reaction: $CH_3OH + 3/2\ O_2 \rightarrow CO_2 + 2H_2O$

The mechanism of this reaction is still a matter of discussion, and different reaction mechanisms have been proposed. The most accepted theory for methanol oxidation consists of two steps: (1) methanol adsorption onto the substrate, (2) oxidation of adsorbed carbon-containing intermediates by adsorbed OH to generate carbon dioxide [15].

The kinetics of oxygen reduction at the cathode is much slower than the methanol oxidation reaction at the anode, and the reaction mechanism is more complex. The cathode reaction in DMFCs is essentially similar to that of PEMFC. Two pathways have been proposed for the oxygen reduction reaction. One is a direct four-electron pathway, and the other is a peroxide pathway [9, 16].

Heterogeneous catalysis by NPs has attracted great attention, due to its relevance in industrial applications. While catalyst deactivation, during operation, is of vital concern [17], narrow size distribution, uniform particle structure, abundant distribution over the support and elevated effective surface area are all necessary for superior catalytic performance [13]. In PEMFCs, Pt NPs are usually the leading choice as the electrocatalyst for hydrogen oxidation at the anode. The hydrogen oxidation reaction is much easier and intrinsically rapid, compared to the oxygen reduction reaction. In the case of using hydrogen generated *in-situ* by reforming other fuels (such as methanol, propane, natural gas, etc.), the Pt electrocatalyst would be quickly poisoned by even the small quantity of carbon monoxide (CO) present in the reformed fuel. Because CO is preferentially adsorbed at the Pt electrocatalyst surface, preventing the dissociative adsorption of hydrogen, this results in a performance loss of the electrocatalyst. To circumvent this issue, other electrocatalysts that provide better CO tolerance are required. Based on many research studies that have been carried out in this area, bimetallic PtRu shows better tolerance to CO than Pt [18].

The electrocatalyst for oxygen reduction at the cathode of PEMFCs is usually Pt or Pt-based alloys. The oxygen reduction reaction at the cathode is much slower than the hydrogen oxidation reaction at the anode. This may be related to the strong O – O bond, highly stable Pt – O or Pt – OH, and the possible formation of peroxide (H_2O_2) intermediate species during the reduction reactions occurring at the Pt surface. However, regarding the complexity of the multi-electron process of the oxygen reduction reaction, disagreements remain on the mechanism for the intermediate species and also on improving the slow kinetics of the oxygen reduction reaction at the cathode [18-20].

In DMFCs, the cathode reaction is essentially identical to that in PEMFCs, but the anode reaction involves methanol oxidation. The slow reaction kinetics of methanol oxidation is due to several factors, such as the associated six-electron transfer process, the adsorption of the reaction intermediate (CO) on the surface of the electrocatalysts and the related poisoning of the electrocatalyst. At present, bimetallic PtRu is known as the state-of-the-art anode electrocatalyst for DMFCs, which can ameliorate the poisoning effects of CO, and shows significantly higher electrocatalytic activity than pure Pt [13, 21]. Two mechanisms have been suggested for the enhanced CO-tolerance associated with PtRu bimetallic catalysts. One is the “reaction-pair”, also called the “bifunctional mechanism”, which indicates the role of Pt in methanol dehydrogenation, while the role of Ru is to provide oxygen-containing species that can easily oxidize the CO adsorbed on Pt sites [15, 22]. The other mechanism is the “electronic effect”, also called the “ligands effect”, positing that the presence of Ru can modify the electronic structure of nearby Pt atoms. Therefore, the change of electronic structure of Pt atoms can affect Pt-adsorbate bonding and, consequently, the electrocatalytic activity of the catalysts [23, 24].

Over the past few years, much effort has been devoted to the development of PEMFC and DMFC technology, applied to most of the stationary and portable devices. There remain several factors preventing the commercialization of these fuel cells, including the high cost involved in the maintenance of the electrolyte and high loading of costly electrocatalyst, low durability, and the lack of refueling infrastructure [10]. Several of the primary, crucial concerns in PEMFCs and DMFCs are the cost, durability, and performance of their electrocatalysts [11]. Hence, this thesis has been directed to the synthesis and characterization of a Pt alloy electrocatalyst, followed by a deep study on the surface chemical species, in order to reduce the cost and increase the durability of the catalyst. Details concerning several challenges presented by electrocatalysts, and the governing factors on their performance, are discussed in the next section.

1.2 Ru-based Nanoparticle Catalytic Activity in PEMFCs and DMFCs (Problem Identification)

Ru NPs are particularly effective in methanation and Fischer-Tropsch syntheses [2], and also show both a high oxygen evolution reaction (OER) activity and an elevated stability in acidic fuel cell environments [25]. They have been supported on several materials, such as SiO_2, Al_2O_3, zeolites and carbon substrates, where their catalytic properties are significantly influenced by both the substrate and its pretreatment [26]. Among these supports, carbon has been widely studied [27-30]. It was found that the characteristics of the substrate used may modify the growth of the deposited NPs and, thus, affect their electronic properties. Moreover, NP distribution and adhesion may also be affected, influencing the overall device performance [31].

One carbon substrate commonly used to study NPs is highly oriented pyrolytic graphite (HOPG), due to its inert, well-defined, conducting surface, as well as little, if any, electronic interaction with the NPs [27, 32]. Determining the adhesion of Ru NPs to HOPG is of interest since it is regarded as a main feature in the optimization of catalytic activity.

Since the operating temperatures in both PEMFCs and DMFCs are low, the use of an electrocatalyst, to improve their slow electrode kinetics, is inevitable. In order to identify a proper electrocatalyst for PEMFCs and DMFCs, one should follow these criteria: (i) the electrocatalysts should be stable under the operating conditions of these fuel cells, which use acidic electrolyte and usually operate at < 100 °C, (ii) the cost of the electrocatalyst, which is included in the type and loading used, and (iii) the adsorption capacity, a narrow nanoscale size distribution, high dispersion on support, and effective surface area are all necessary factors for a high performance catalyst [10, 13].

1.2.1 Challenges for Pt NP electrocatalysts

Based on the literature, Pt is the most electroactive catalyst in PEMFCs and DMFCs, because of its chemical adsorption properties of both the fuel and the oxidant[10]. However, Pt catalysts still have some drawbacks. First, due to the need of large Pt loading as the electrode catalyst and the depletion of Pt as a natural resource; its use becomes more and more expensive. Second, trace impurities in the reforming fuel, such as CO, may adsorb on the Pt, which hinder active sites, and cause electrocatalyst poisoning. In addition, due to producing CO as an intermediate species in the methanol oxidation reaction in DMFCs, Pt will again be poisoned. Third, the degradation of Pt catalysts is one of the major factors that reduce the lifetime of a PEMFC. catalyst durability is of great importance in lengthening PEMFC operation life, along with enhancing reliability and reducing the total lifetime cost [33]. The degradation of Pt catalysts is considered to be due to agglomeration, leading to increased NP size, the oxidation of the Pt catalyst that occurs at elevated potentials, and the dissolution of Pt catalysts into the electrolyte. Generally, This is due to their high specific surface energy [34]. The smaller sizes of nanoparticles mean higher specific surface areas, making them more inclined to agglomerate [35]. Gonzalez *et al*. [36] found that, based on the duration tests in PEMFCs, Pt alloyed with non-precious metal catalysts presents higher stability against dissolution than the pure Pt catalysts. In a review, by Shao *et al*. the authors suggested that the alloyed metals might increase the resistance of Pt to oxidation [33]. Therefore, alloying Pt with other metals can improve catalyst durability [33, 37, 38].

Thus, in order to improve the performance of PEMFCs and DMFCs, reduce the cost of electrocatalysts, and remove the prohibitive factors preventing commercialization of these fuel cells, some alternate electrocatalysts have been studied [9, 10]. Among various low-Pt and Pt-free catalysts, PtRu bimetallic materials are considered to be among the most promising catalysts in such fuel cells, due to their lower cost, high electrocatalytic activity, high tolerance for CO, superior performance in decomposing methanol, and high activity in oxidizing CO to form CO_2 [39-43].

Adding a second metal, to form bimetallic NP catalysts, can improve catalytic performance. One of the reasons is thought to be the modification of the bimetallic system d-band structure[44]. For instance, the formation of PtRu alloys increases their d-orbital vacancy[45] because of the less occupied d orbitals of Ru (d^7), compared to those of Pt (d^9). It has been suggested that the increased ability of the PtRu bimetallic surface to take on electrons results in the enhancement of the oxidation process [45]. Moreover, water dehydrogenation occurs more readily on Ru, while methanol dehydrogenation occurs more readily on Pt [13, 46]. Thus, Ru can provide preferential sites for OH adsorption by dehydrogenating water [47]. These OH species then cause the complete removal of CO by oxidizing it to CO_2. In addition, the introduction of a second metal can change the d-band center of the bimetallic system, due to the variations in the d-band structure. This is because of the changes in the electronic structure of the bimetallic system and the direct electron interactions between two constituent metals. This leads to changes in the bond strength between the component metals. Ling, et al. [44] found that the deposition of Pt onto nanoporous gold results in the d-band center of the bimetallic system being altered and decreased from -3.93 to -4.24 eV. Such a lowering of the d-band center is essential to weaken the binding strength between Pt active sites and intermediate poisoning species. Thus, alloying reduces the poisoning effect and improves the catalytic activity of Pt [44]. However, the kinetic energy that they used probes the whole NP, not only the NP surface. Since the catalysis occurs at the surface, the authors made assumptions that it applies to the surface. We note that the shift of the d-band center may be only one of several contributions to improved catalytic activity.

1.2.2 Challenges for PtRu NP electrocatalysts

The compositions, morphologies, and structures of PtRu alloy NP systems are of great importance for their surface catalytic activities [6]. In order to understand their role in electrocatalysis, so as to improve performance, one must determine and understand the PtRu NP surface structure. Unfortunately, this remains an issue. Some researchers maintain that Pt diffuses into Ru [3-5], while the others claim the reverse [6, 7, 48]. There is also disagreement as to whether Pt [3-5] or Ru [6, 7] is found at alloy NP surfaces, and as to which form surface oxides [3, 6, 49]. This inconsistency has presented a challenge in determining the optimum structure of the PtRu catalyst. Despite this, most *theoretical* papers contain calculations based on the assumptions that there are no surface contaminants, and that Pt is always at the surface [50]. As we show here, both are incorrect. Many *experimental* papers also assume the same, probably following the theoretical assumptions. Because of this, determining the structures of PtRu alloy NPs is an essential key to interpreting their catalytic behaviors and optimizing their performance.

Another important issue in electrocatalysts is their preparation method. Different preparation methods, solid phase or liquid phase methods, may result in different particle sizes and surface compositions. Conventional preparation methods, such as deposition-precipitation and impregnation usually have poor control of metal distribution and surface composition [51-53]. Generally, due to the chemical reduction steps in the liquid phase methods, impurities are included in the structure. The solid phase methods are cleaner and simpler, and one of its sub-groups; physical vapor deposition, is employed to prepare the metal and alloy NPs in this thesis. Since electrocatalysis is a surface phenomenon, any variation in the preparation process could lead to differences in the NP surface [54]. For instance, using a preparation method that produces small and well-separated particles will result in more electrocatalyst atoms with a higher surface area to participate in the reaction, which will improve the utilization of the electrocatalyst. On the other hand, using a preparation method that synthesizes large particles, or even agglomerated particles, diminishes the accessible surface area, decreasing durability, along with decreasing the catalyst activity, and finally, reduces the lifetime of the fuel cell. The effect of the preparation methods on the electrocatalysts surface is a subject that has not been addressed sufficiently.

1.3 Objectives of the Thesis

The general objective of this thesis is the formation of Ru-based NPs onto HOPG, as a substrate, by physical evaporation and the subsequent investigation of their surface chemistry and structure, to be employed and optimized as electrocatalysts to enhance the performance of PEMFCs and DMFCs.

1.3.1 Specific objectives

(1) Preparation of pure Ru NPs deposited onto HOPG, to investigate its oxidation states, surface chemical species, and electronic structure of NPs, and also to determine the adhesion of Ru NPs to HOPG.

(2) To obtain well-separated and small sized Ru NPs, and to perform morphological studies on them.

(3) To prepare PtRu bimetallic NPs deposited in several ways (metal 1 over metal 2, and both metals simultaneously), onto HOPG and to investigating their evolutions as a function of annealing temperature.

(4) To investigate the surface chemical reactions between metals and inevitable adventitious gases (hydrocarbons and oxides), on annealing.

(5) To study the variations in electronic structure, phase and crystal structure of NPs during the annealing process.

1.4 Outline of the Thesis

We investigate the chemical, compositional, and structural properties of NP surfaces, where catalysis activities take place. This is done by the synthesis and characterization of Ru-based NPs deposited onto HOPG and their subsequent analyses by several *in-situ* and *ex-situ* surface and bulk techniques. This approach provides a more comprehensive knowledge of the surface constitution that will help to optimize catalytic activity and fuel cell performance.

This thesis consists of five chapters. The current chapter; chapter 1, provides an introduction to fuel cells, especially PEMFCs and DMFCs, several main challenges due to Pt and PtRu electrocatalysts, followed by explaining the general and specific objectives and organization of the thesis. Chapter 2 includes the basic principles of the several surface and bulk experimental tools that were employed in this thesis to investigate the Ru-based NPs. The principle results of this thesis are described in the chapters 3 and 4, and in the appendices.

Chapter 3 presents the preparation of Ru NPs, which are deposited onto HOPG at different thicknesses, using low and high deposition rates. *In-situ* XPS characterization and *ex-situ* morphological studies of Ru NPs were carried out in order to investigate the behavior of these NPs. This knowledge was used with our group's previous study on Pt NPs [1] in the preparation of the PtRu NPs.

Chapter 4 describes the synthesis and characterization of the PtRu bimetallic NPs using three different orders of deposition, deposited onto HOPG. The differences among these three PtRu NPs, in terms of surface and bulk characteristics, are studied by using several analytical and morphological techniques. We wish to fully understand the surface chemistry and structure of PtRu bimetallic NPs, to help us to understand the reasons necessary for catalysis optimization.

Chapter 5 focuses on the discussions and conclusions of this thesis and recommendations for future work.

CHAPTER 2 EXPERIMENTAL APPROACH

This work proceeded in two phases, using physical deposition of the metals: one concerns the synthesis of Ru NPs, and the other, the preparation of PtRu NPs, both on HOPG, using three different orders of metal deposition. The preparation protocols of these two phases are described in detail in the Experimental sections of chapters 3 and 4. Several surface and bulk analytical techniques were employed to study surface chemistry, composition, and crystal structure. This chapter discusses the basic principles of these techniques. More specific procedures for each technique are given in the chapters 3 and 4.

2.1 Physical Vapor Deposition (PVD)

Physical vapor deposition (PVD) is one of the methods used to produce nanoparticles. PVD employs physical processes, such as heating or sputtering, to produce a vapor, which is followed by condensation onto the substrate [55]. Particles or thin films coated by PVD exhibit excellent coating adhesion, durability and high purity [56]. PVD is partitioned into various sub-groups. One such sub-group, electron beam evaporation, is described in the following section. This is the method utilized in this thesis, to prepare all the NPs.

2.1.1 Electron beam (e-beam) evaporation

The e-beam evaporation method is of great interest due to its high efficiency in material utilization, the structural and morphological control of particles by adjusting the deposition rate, and the significant distribution of the evaporant on the substrate. Figure 2.1 depicts a typical e-beam evaporator. In this technique, the filament is heated to produce a beam of electrons. Their path is directed and bent by the deflecting and focusing magnets located in the chamber. The electron beam concentrates large amounts of heat onto a very small area in order to evaporate the material to be deposited. The material evaporated is able to move freely in the vacuum chamber until it condenses onto the substrate surface; this is because deposition in e-beam evaporation systems is always conducted under high vacuum conditions, in which the evaporated particles move from the source to the substrate without colliding with residual gases [57]. E-beam evaporators have the lowest deposition rate (0.01-0.03 Å/s); in our study, this turns to an advantage, as discussed in the Chapter 3. This technique has been particularly fruitful in the production of alloys by evaporating two or more materials.

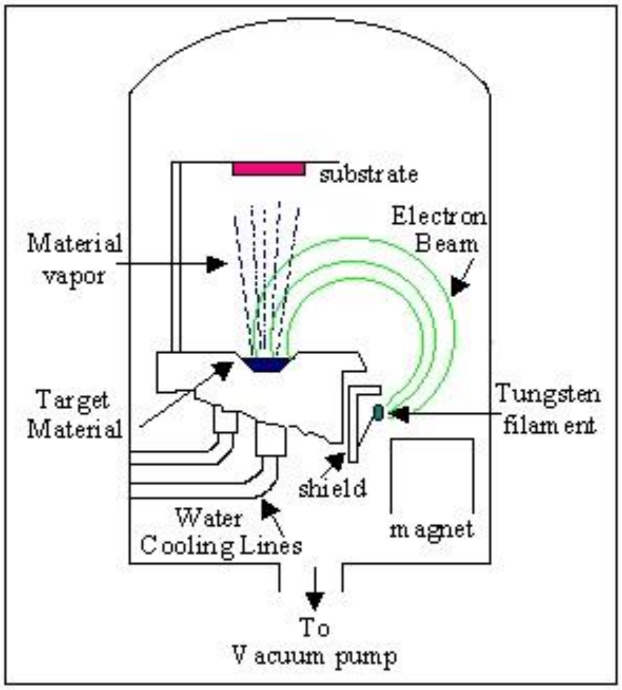

Figure 2.1: Schematic of electron beam evaporation equipment [58].

2.2 Surface Analysis Techniques

Obtaining a complete description of a surface is always beneficial for surface applications, such as for catalysts and sensors. For this purpose, several surface analysis techniques are required to investigate the surface atomic composition and electronic structure of surface components. Here, two of the most useful surface techniques, XPS and TOF-SIMS, are discussed.

2.2.1 X-ray Photoelectron Spectroscopy (XPS)

X-ray photoelectron spectroscopy, also known as ESCA (Electron Spectroscopy for Chemical Analysis), is a surface technique that is capable of probing depths of 3 – 5 nm. It has been employed for decades and has provided some of the most fundamental information about the elemental composition, chemical state and electronic structure of the surface [59, 60].

As shown in Fig. 2.2, XPS is performed by exciting a sample surface with mono-energetic x-ray photons (usually Mg or Al Kα or synchrotron radiation). The process is based on the photoelectric effect, which causes both core and valence level electrons to be emitted from the sample surface, when the energy of the x-ray photons is larger than their binding energy.

Einstein equation gives the relation between kinetic and binding energies:

$$E_b = h\upsilon - E_k - \Phi \tag{2.1}$$

where E_b is the binding energy of the core electron, $h\upsilon$ is the energy of the exciting x-ray photon; E_k is the kinetic energy of the electron measured by the analyzer; and Φ is the work function (the amount of energy the particle loses in overcoming the surface potential of the sample) [61]. The binding energy of the core electron depends upon several factors, such as the element, the orbital from which the electron is ejected, and the chemical environment of the atom from which the electron is emitted. Hence, the binding energy and intensity of a photoelectron peak permit identification and quantification of all surface elements: the peak intensities measure the quantity of a material at the surface, while the peak positions provide the elemental and chemical composition [60].

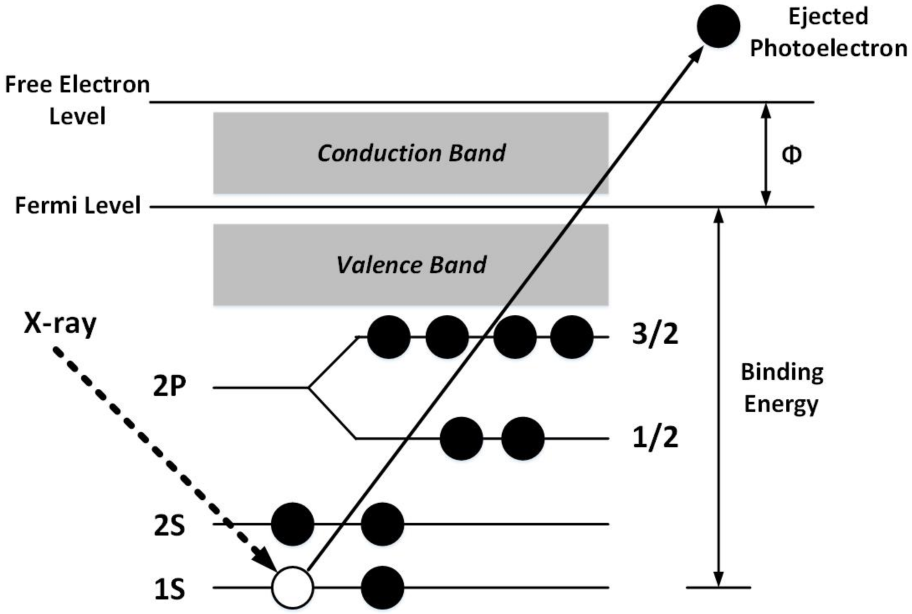

Figure 2.2: Schematic of XPS principle.

The distance that an electron can traverse in solid depends on the both material and electron kinetic energies. The surface sensitivity of the XPS is based analyzing those ejected electrons at a particular energy (defined as the pass energy in the instrument) that have not lost energy through inelastic electron-electron collisions. The inelastic mean free path (IMFP, λ) is the depth at which ~ 37 % of the electrons are attenuated. The IMFP values are found in the "universal curve", which gives λ for various materials and kinetic energies; the depth probed is taken as 3x the value of λ, the depth at which ~ 95 % of the electrons are attenuated. More details regarding the "universal curve" are given elsewhere [61].

XPS analysis is performed using two types of scans; a lower resolution survey scan and high resolution scan. The former displays all detectable elements at the surface and measures their amounts; the latter, which takes much longer, reveals chemical state and chemical environmental differences. The high resolution scan also separates differences between surface and bulk electronic state contributions that are statistically significant, as found for some transition metals [62]. XPS spectra plot intensity vs. binding energy. Figure 2.3 illustrates a typical XPS spectrum obtained in a survey scan. In that spectrum, there are photoemissions from core and valence levels, as well as x-ray excited Auger emissions. High resolution scans can be carried out on each peak from either core or valence levels.

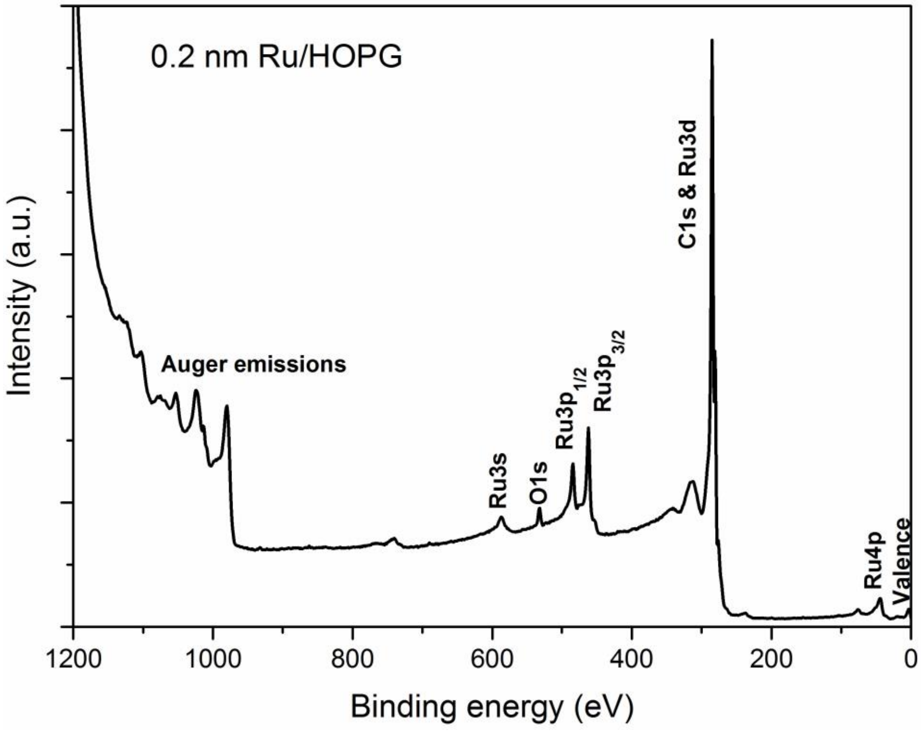

Figure 2.3: XPS survey spectrum of Ru NPs deposited onto HOPG, excited by Mg kα.

In XPS spectra, orbitals having angular momenta (i.e., p, d, f) appear as doublets at different binding energies. This is known as spin-orbit splitting; LS coupling in light atoms (generally with atomic number less than 30) and jj coupling in heavier atoms (in our case) [63, 64], as shown in Fig. 2.3 (Ru3$p_{1/2}$ and Ru3$p_{3/2}$). For any electron in an orbital having orbital angular momentum, coupling between magnetic fields of spin (s) (or total spin angular momentum (S)) and angular momentum (l) (or total orbital angular momentum (L)) occurs. Both LS and jj coupling could be used in XPS doublets, although the latter is easier to use. Therefore, the XPS peaks are labeled using the nomenclature nl_j where n is the principle quantum number, l is, as mentioned above, the orbital corresponding to the angular momentum quantum number and $j = l + s$ (where s is ± 1/2). The peaks related to each orbital with different j values also have specific area ratios based on the respective degeneracy of each spin state. Therefore, the relative intensities of the doublet peaks are determined by $(2j_1+1)/(2j_2+1)$, where j_1 and j_2 are the j values for each component of the doublet [63]. The area ratios and j values of spin-orbit doublets are presented in Table 2.1. These ratios must be considered when doing curve-fitting of the p, d and f core level spectra. In order to quantify the intensity of XPS peaks, the proper modeling of the background signal is required. Among various types of background subtraction, the Shirley technique [65] was employed in this thesis, due to its ease of use. In this background subtraction method, the background intensity at any given binding energy is proportional to the intensity of the total peak area above the background in the lower binding energy peak range [66]. In some cases, because of some inherent uncertainties in the Shirley background subtraction of the spectra, the ratio between the doublets might not follow the exact area ratios in Table 2.1. These small changes in the ratio do not affect other peak component parameters, such as binding energies and atomic component fractions, although the changes lead to better curve-fitting.

Table 2.1: Spin-orbit splitting parameters.

Subshell	*j* values	Area ratio
s	1/2	n/a
p	1/2, 3/2	1:2
d	3/2, 5/2	2:3
f	5/2, 7/2	3:4

Different types of bonds of an element appear at different binding energies. In other words, the binding energy of a core electron is sensitive to the chemical environment of the emitting atom. This effect is called a "chemical shift". For instance, a carbon of a carbonyl group will have slightly different position and intensity than that of a carbon in a carbide group, in the C1s XPS spectrum. Chemical shift information is a very powerful tool for identifying the functional group, chemical environment or oxidation state [62].

Another notable benefit of XPS is its ability to quantify surface atomic concentrations, with good precision. In this technique, the number of ejected electrons is proportional to the number of atoms at the surface. In fact, by using the peak intensity and the relative sensitivity factor, the relative atomic fraction of each element can be determined [67].

Figure 2.4 illustrates the components of our XPS. The specifications of all the instruments used in this thesis are explained in the experimental sections of chapter 3 and 4. The main components of our XPS are the X-ray source, the electron collection lens, the electron energy analyzer, the electron detector, the readout and data processing.

Our XPS system enabled us to perform *in-situ* synthesis and characterization of the metal and alloy NPs. In this thesis, *"in-situ"* refers to the synthesis and characterization of the samples without exposure to air. The synthesis of NPs was accomplished by an e-beam evaporator, and annealing steps were carried out using the sample heating stage present in the preparation chamber. The analyses were done using an X-ray source located in the analysis chamber. The entire experiments and analyses were performed under UHV conditions ($< 3 \times 10^{-8}$ torr).

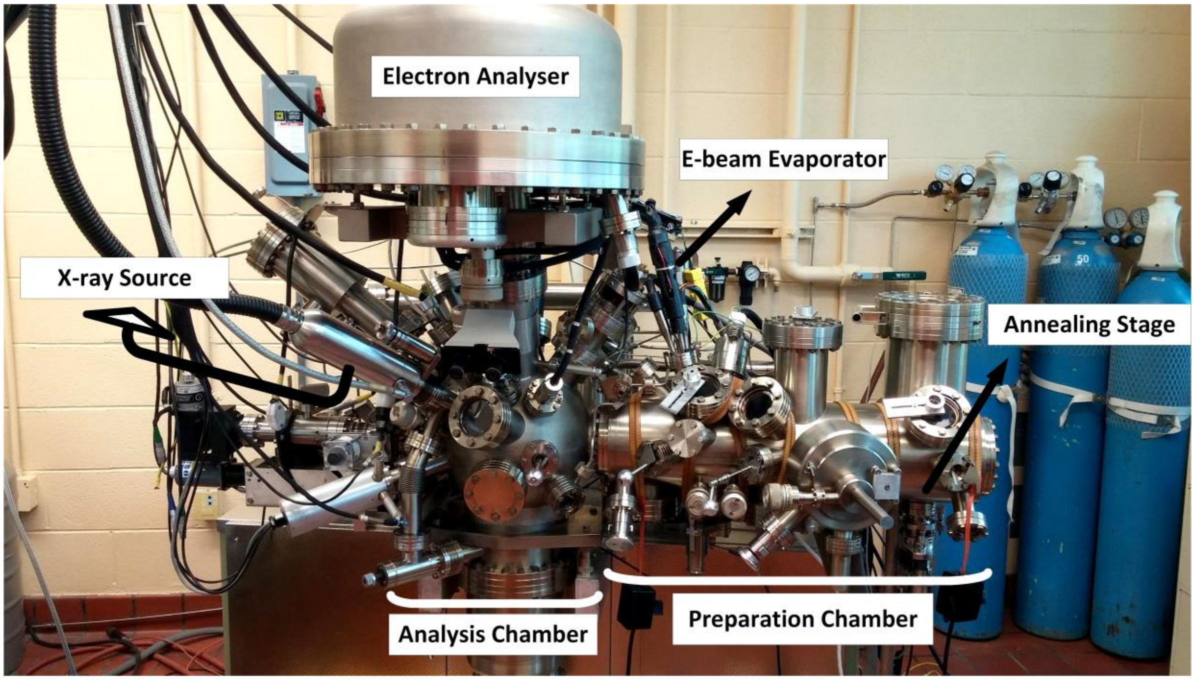

Figure 2.4: A photo of our XPS (VG ESCALAB 3 MARK II).

In our XPS data analysis, we have employed the symmetric peak XPS component analysis method, developed in our laboratory, to identify the surface, volume, electronic and contaminant features of several First, Second and Third Transition Series metal NPs [32, 68-72], showing its validity in the characterization of metal NP surface chemistry and structure.

Historically, metal core level XPS spectra were found to exhibit asymmetries to the higher binding energy side. Based on the Doniach and Šunjić [73] theory, proposed to fit the spectrum, this asymmetry had come to be considered a natural occurrence, attributable to the promotion of electrons near the Fermi level to empty states just above it; however, this proposal does not explain asymmetries found in non-metals, such as HOPG and carbon nanotubes (CNTs) [68, 69, 74], where the promotion of electrons envisaged by Doniach and Šunjić does not occur.

Our symmetric peak component XPS analysis method [68, 69, 74] posits that the apparently asymmetric XPS peaks are, in fact, symmetrical, and that the asymmetry is due to smaller peak components immediately adjacent to the zerovalent metal peak component, on the higher energy side, where peaks due to compounds of the metal are found. Indeed, in some cases, the asymmetry has been found to change with time, exposure to oxygen and irradiation [68, 69], which is not in accord with the Doniach and Šunjić model [73]. For instance, a freshly prepared film of Co, in a previous study by our group [75], showed a totally symmetrical 2p doublet; after remaining in the XPS vacuum chamber for several hours, both doublet components became significantly more asymmetrical, with new peaks appearing in the C1s and O1s spectra. This indicates that the inevitable contamination could be a source of metal peak asymmetry. In other words, the experimentally obtained asymmetric XPS peaks are composed of several overlapping minor symmetric peaks rather than a single asymmetric peak [68].

Thus, our use of additional symmetric peaks to account for the asymmetry reveals the presence of component peaks that are otherwise hidden when using asymmetric components; as expected, these component peaks have energies independent of experimental conditions. As explained in the review by Sacher [68], three principles must be employed when applying the symmetric peak component analysis to asymmetric spectra: i) the minor peaks, adjacent to the major peak, whose presence causes the asymmetry, must have a previously identified physical or chemical basis, ii) ligand field effects that occur in some metals, such as Co, must be considered, iii) a chemical bond between two different elements must be quantitatively observed in the XPS spectra of both elements. Again, as noted in the review by Sacher [68] on the subject, these previously hidden component peaks give information on NP surface contamination, oxidation, electronic configuration, and interfacial bonding. In every case [32, 68-72], this information has been confirmed from other sources. Consequently, symmetric component peak analysis is employed in this thesis, and permits us to indicate the electronic structures of Ru and PtRu NPs used in catalysis, their extents of adhesion to the substrates normally used, as well as the contaminants that are found on their surfaces. Symmetric peak component analysis is also capable of distinguishing differences in the chemical and physical environment of an element. Hence, the information previously obtained on pure Pt [1] and our present results on Ru were used to determine the interactions between them in the alloys, and helped distinguish between pure metal and alloy component peaks.

In our Ru study (Chapter 3), the errors in peak positions are estimated to be ≤ ±0.4 eV, with reproducibility ≤ ±0.2 eV and, in area ratios, ≤ ±10 %, with reproducibility ≤ ±5 %. In our PtRu study (Chapter 4), the errors in peak positions are estimated to be ≤ ±0.3 eV, with reproducibility ≤ ±0.2 eV and, in area ratios, ≤ ±3%, with reproducibility ≤ ±2%. These values were obtained through numerous repetitions of each of the spectra obtained.

2.2.2 Time-of-Flight Secondary Ion Mass Spectrometry (TOF-SIMS)

Time-of-flight secondary ion mass spectrometry (TOF-SIMS) is a very sensitive surface analytical technique, with an average probe depth of 1-2 nm, high mass resolution, and high sensitivity (~1ppm). This technique provides detailed elemental and molecular compositions at the surface of solid materials, for both insulating and conducting samples. It also distinguishes the different isotopes of the same element [76].

TOF-SIMS is accomplished by focusing a pulsed beam of energetic primary ions onto a sample surface, producing secondary ions and ion clusters, to be emitted from the very outermost surface of the sample. The primary ions are typically Ga^+, Cs^+, Bi^+, and O^-, with energies of 1-25 keV. After the surface is bombarded by the primary ions, the secondary ions are electrostatically accelerated into a field-free drift region, and a time-of-flight analyzer is employed to measure the mass of the emitted positive and negative ions and clusters [76, 77].

There are three operational modes in TOF-SIMS: (1) surface spectroscopy, that can provide mass spectral information, (2) surface imaging in the XY dimension across a sample, which provides spatial distributions of different species and (3) depth profiling, which gives information in the Z direction (into the sample) for in-depth elemental and molecular analysis [78].

TOF-SIMS instruments typically consist of an ultrahigh vacuum system, a particle gun, a flight path (which is either circular or linear), using electrostatic analyzers or reflecting mirrors in order to direct the particle beam, the mass detector system, and a computer and software for system control and analysis. Figure 2.5 illustrates the schematic of a TOF-SIMS instrument [78].

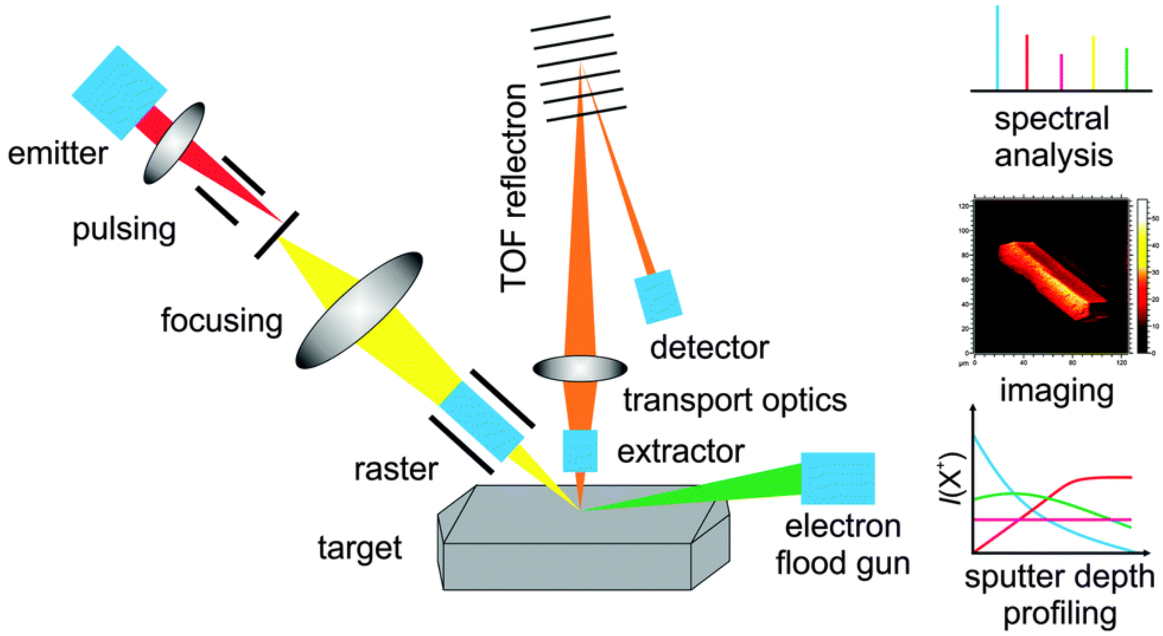

Figure 2.5: Schematic of a TOF-SIMS instrument and the three operational options for mass spectrometric of a surface, imaging, and depth profiling [79].

Both XPS and TOF-SIMS techniques are powerful surface techniques. In XPS, while the surface portion shows a significant role in signal strength, the bulk contribution to the signal is still evident. However, in TOF-SIMS, signals only come from the first 1-2 nm of surface constituents (only a few atomic layers). XPS produces quantitative analyses, while TOF-SIMS is qualitative. We have combined information from both these complementary techniques in characterizing our surfaces.

2.3 Bulk Analysis Techniques

The aim to implement bulk analyses is to fully investigate the chemical and structural differences between surface and bulk of Ru and PtRu NPs deposited onto HOPG. Here, a brief description of the three powerful bulk analysis techniques, HR-TEM, HAADF/STEM, and EELS are presented.

2.3.1 Transmission Electron Microscopy (TEM)

Transmission electron microscopy (TEM) is a powerful microscopy technique, operating on the basic idea similar to the light microscope, although energetic electrons are used instead of light. The TEM imaging technique is capable of producing high-resolution images (down to 1 nm in size) that reveals information on the size and morphology of NPs or thin films. Figure 2.6

illustrates the main components of a typical TEM. First, monochromatic electron beam is generated by an emission source, which may be a tungsten filament, or a lanthanum hexaboride (LaB_6) source. Coherent small beam can be achieved by using condenser lens. The condenser aperture is employed to remove the high-angle electrons. The focused electron beam then interacts with the samples with a part of transmitted electrons, and also scattered ones. The sample needs to be thinned, using various sample preparation methods, to be electron transparent. High angle electrons are blocked by the objective aperture, enhancing the contrast. Then, the transmitted and unscattered electrons pass through the intermediate lens and objective lens and form enlarged images. Finally, the image is projected on a fluorescent screen, to form an image that the user can observe. The image can be managed by adjusting the voltage of the electron emission source to control the speed of electrons that directly correlate to electron wavelength. The lighter areas of the image represent the places where a greater number of electrons are transmitted, while the darker areas reflect the dense regions of the sample, with less transmitted electrons. The TEM experiment is carried out under high vacuum, providing a clean environment where electrons will not be scattered [80].

For this study, a high-performance TEM with a Schottky type field emission electron gun, at an accelerating voltage of 200 kV, was employed. In many types of electron microscopes, the field emission gun is used to produce a narrow electron beam (down to < 0.05 nm), high long-term stable currents, with up to three orders of magnitude greater current density or brightness than conventional emitters. These result in significantly improved signal-to-noise ratio, spatial resolution, and the image quality [81].

TEM was used to evaluate the effect of the deposition rate on the morphology and size of pure Ru NPs deposited onto HOPG substrate. The chemical and compositional analyses of Ru NPs were determined with an energy dispersive X-ray spectroscopy (EDS or EDX), which is integrated into the TEM instrument. This technique determines elemental identification through the measurement of characteristic X-ray energies. The number and energy of the X-rays emitted from a sample can be measured by an X-ray detector in the EDS. The energies of the X-rays are characteristic of the emitting element, so that EDS provides the elemental composition of the sample. The technique can be quantitative and provides spatial distribution of elements through mapping [82].

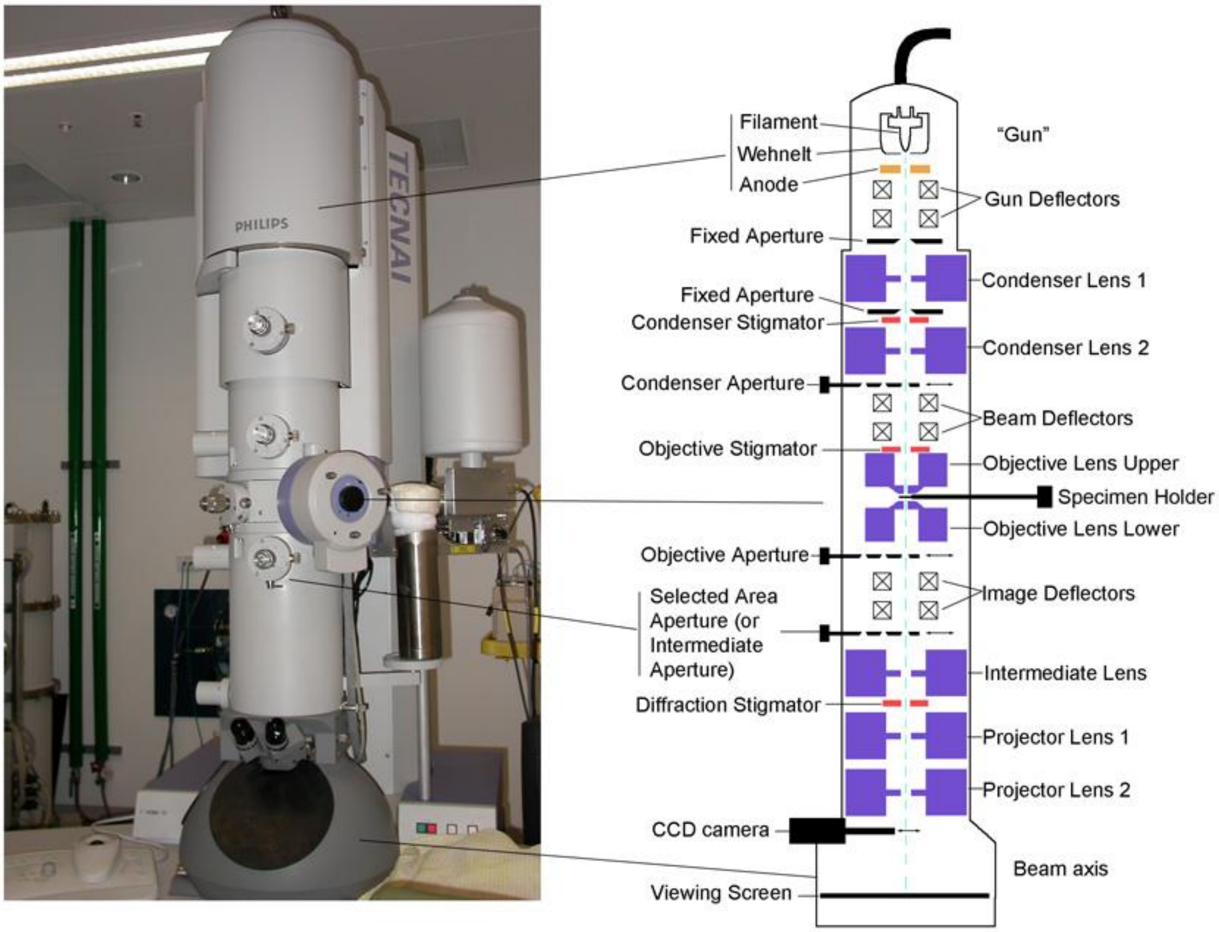

Figure 2.6: A diagram of the internal structure of a TEM alongside an example of a TEM instrument [83].

2.3.2 High-Angel Annular Dark-Field / Scanning Transmission Electron Microscopy (HAADF/STEM)

Scanning transmission electron microscopy (STEM) combines the principles of TEM and scanning electron microscopy (SEM). One of its principal advantages over TEM is in providing signals that cannot be spatially correlated in TEM, including secondary electrons, scattered beam electrons, and electron energy loss [84]. In addition, in STEM, the beam converges, instead of focusing, in order to create a probe to be scanned over the sample. The plane where the beam converges is called the focusing plane. The STEM operates in a manner similar to a SEM. The STEM technique scans a fine, highly focused beam of electrons over the sample in a raster pattern. A STEM image is obtained by displaying the integrated intensities of the electrons in synchronization with the incident probe position. Its primary advantage over conventional SEM imaging is the improvement in spatial resolution [84, 85].

Beam electrons may be elastically scattered by the nuclei of sample atoms. In STEM, the images, which are formed by beam electrons scattered through a relatively large angle, are collected with an annular dark-field detector. High-angle annular dark-field (HAADF) imaging is a method of mapping samples in the STEM [84]. The dark-field imaging in TEM is different from that in STEM. It is performed by moving the objective aperture (tilting the electron beam), and collecting the diffracted electrons. The HAADF signal is directly proportional to the density, thickness, and the atomic number of the sample. Thus, these make it possible to produce images that show contrast due to the mass-thickness (where the signal is proportional to the number of atoms) or Z contrast images (where the signal is proportional to the atomic number (Z) of the sample) [86, 87].

Electron energy loss spectrometry (EELS) is an analytical technique that characterizes transmitted electrons to determine the amount of the kinetic energy they have lost in interactions with the sample, giving rise to the electron energy loss signal. This spectrometry permits obtaining chemical and elemental information from the same sample region on which STEM imaging was performed. This information acquires through characteristic ionization edges corresponding to excitations of inner shell electrons into the first available unoccupied states. EELS data typically consist of either energy loss spectral information from the sample (spectroscopy) or images (elemental mapping) that create by selecting electrons with a specific loss energy by a slit so as to image them. Therefore, the element distribution in a specimen can be visualized. Overall, this technique provides information on the elemental mapping of heterogeneous nanoparticles, the elemental identity, elemental distributions, chemical and compositional properties, and phase structure, at atomic resolution [88-90].

Due to the different signal collection characteristics of the HAADF and EELS detectors in the STEM instrument, both type of measurement can be performed simultaneously. In fact, the HAADF detector collects scattered electrons from a high-angle annulus around the beam, which permits the transmitted electron beam (unscattered electrons) to pass through the center hole of the annular dark field detector to reach the EELS detector. However, proper control of the detector angles is pivotal in both data collection efficiency and its interpretation. Moreover, STEM devices are equipped with a central or low-angle annular bright field detector that has the possibility of collecting transmitted electron beams, in order to display bright field or phase signal. In fact, in bright field imaging, the electrons have either not been scattered at all or have been inelastically scattered at low angles. This imaging reveals largely crystallographic information [85, 87]. Figure 2.7 depicts the diagram of a STEM with its different detectors including: annular dark field with high and medium angle, bright field and low angle bright field, and EELS spectroscopy.

In this study, HAADF/STEM, along with EELS, were used in order to investigate the atomically-resolved structure, the morphology, the various phases, the distributions of Ru and Pt, and the internal crystal structures of the PtRu NPs. In addition, the focused ion beam (FIB) technique was employed because of the advantage it offers in determining the relative positions of elements with respect to the HOPG substrate, when used to prepare cross-sections. This technique uses a beam of ions instead of electrons. The focused ion beam can directly modify the sample surface, by using the sputtering process. By manipulating the energy and intensity of the ion beam, it is possible to carry out very precise nano-machining to remove unwanted material, or even top layers of a sample [84].

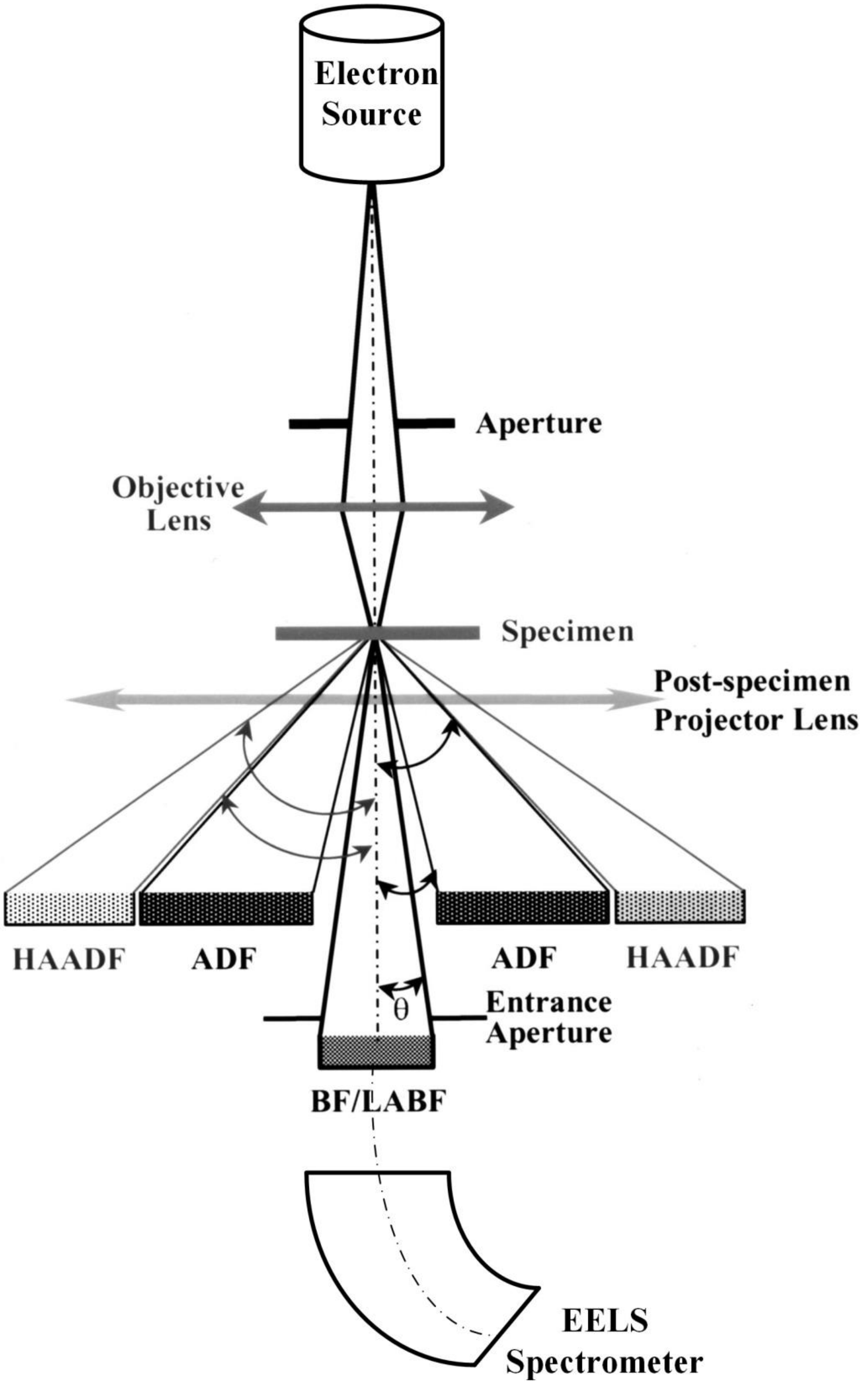

Figure 2.7: Schematic of HAADF-STEM-EELS.

CHAPTER 3 X-RAY PHOTOELECTRON SPECTROSCOPIC AND MORPHOLOGIC STUDIES OF RU NANOPARTICLES DEPOSITED ONTO HIGHLY ORIENTED PYROLYTIC GRAPHITE[1]

3.1 Introduction

Investigating the physicochemical and morphological behavior of Ru NPs deposited onto HOPG is of great importance, not only because Ru NPs act as effective catalysts in specific reactions, but also because alloying it with Pt creates a favorable catalyst in fuel cell technology, as discussed in Chapter 1. Therefore, a knowledge of the physicochemical characteristics of Ru before alloying, in addition to what we already know of the physicochemical characteristics of Pt, helps to understand the complicated PtRu alloy structure, especially at the surface.

Here, we first describe the preparation method of high purity Ru NPs, using physical vapor deposition. Then, the core- and valence-level electronic structures of Ru evaporated onto HOPG as a function of deposition, are described. Both high and low deposition rates were used, and examined by TEM measurements. A comprehensive discussion of these findings is presented in this chapter.

3.2 Synthesis of Ru NPs, *in-situ* and *ex-situ* characterization methodes

HOPG, grade ZYA, 1 cm × 1 cm × 2 mm, was obtained from SPI, Inc. It was cleaved with adhesive tape immediately prior to each experiment and quickly inserted into the spectrometer. A high resolution scan of freshly cleaved HOPG was performed prior to each deposition, and exhibited no trace of organic oxides.

XPS was carried out in a VG ESCALAB 3 MARK II (Thermo VG Scientific) XPS spectrometer, using a non-monochromated Mg Kα X-ray source (1253.6 eV). Ru (American Elements) was deposited in the preparation chamber of the instrument, at a pressure of $< 3 \times 10^{-8}$ Torr, using a Quad-EVC evaporator (Mantis Deposition, Ltd.); several nominal thicknesses (0.25, 0.5, 1.0, and

---

[1] This chapter is published in *Applied Surface Science*, Volume 355 (2015), 279-289.

1.5 nm) were deposited onto HOPG, at both low (0.13 nm/min) and high (1.3 nm/min) deposition rates. The thickness was monitored by a quartz crystal microbalance placed near the sample.

After sample transfer through a gate valve, without exposure to atmosphere, XPS was performed in the analysis chamber, at a base pressure of $< 2 \times 10^{-9}$ Torr. High-resolution spectra were obtained at a perpendicular takeoff angle, using a pass energy of 20 eV (step size: 0.05 eV; step dwell time: 200 ms). The instrument resolution was 0.7 eV. Core level spectra were obtained for the Ru3d, Ru3p, Ru3s, C1s, and O1s electron emissions, and valence band spectra were obtained for the 4d and 5s emissions.

After Shirley background removal, the component peaks were separated with the VG Avantage software, using mixed Gaussian-Lorentzian functions; the Gaussian: Lorentzian ratios used for Ru3d, 3p and 3s were 50: 50, 80: 20 and 89: 11, respectively, as determined by the best fit of the software. The binding energy was calibrated by placing the principal C1s peak at 284.6 eV; this commonly used procedure adjusts the energy scale, precisely placing the binding energy positions of both core and valence spectra, as well as the position of the Fermi level.

The peak widths employed in the component separations, given as full widths at half maxima (fwhm), were those previously found in our research group studies, except for the valence band, which was fit according to the results of Shen *et al.* [26]. Relative concentrations were obtained from high resolution spectra, using sensitivity factors regularly confirmed with standard samples.

Transmission electron microscopic characterizations were limited to determining the size and state of aggregation of the deposited Ru NPs. This was done using a JEOL JEM-2100F microscope, equipped with a LaB_6 filament, operating at 200 kV and having its own energy dispersive X-ray analyzer (EDX, Phoenix). Samples were prepared, as we have done previously, by using a scalpel to scrape small pieces of the NP-containing HOPG substrate onto a Cu TEM grid. The NP size determination was performed using ImageJ software, which is an open source image analysis tool developed by the US National Institutes of Health [91].

3.3 Results

3.3.1 XPS Spectra

The Ru3d, Ru3p, Ru3s, C1s, and O1s core level XPS spectra were analyzed, using symmetric peak components. Spectra were followed as a function of Ru deposition, over a nominal deposition range of 0.25-1.5 nm. The intensities of all the Ru spectra increase, while that of the C1s spectrum decreases with Ru thickness, indicating that most, if not all, of the C1s signal comes from the substrate. All of the Ru core level spectra were found to be composed of three symmetric component spectra.

3.3.2 C1s-Ru3d Spectra

The complexity of the overlapping C1s and Ru3d core level XPS spectra is well known to workers in the field, and has been a reason for avoiding the deconvolution of the Ru3d spectrum. Rather, the less intense Ru3p or 3s spectra are commonly used [25, 26, 92-96], with a resultant increase in uncertainty. Here, we show that a foreknowledge of the HOPG structure, as revealed by XPS [97], and an understanding of the Ru3d$_{5/2}$,3d$_{3/2}$ spin-orbit component ratios and their energy separations, makes the use of this spectrum possible, revealing structure not previously seen. That is, the composite C1s-Ru3d spectrum was peak-separated knowing the positions of the C1s components of HOPG (see reference [69] and Table 3.1), knowing that the Ru3d$_{5/2}$ and 3d$_{3/2}$ components have a 3:2 area ratio, and knowing that each spin-orbit pair is separated by the same constant energy difference. The three 3d components, as a function of increasing binding energy, are referred to as Ru1, Ru2 and Ru3; their area ratios are 1: 0.17: 0.08.

Figure 3.1a shows the evolution of the spectrum as a function of Ru deposition at the higher deposition rate of 1.3 nm/min. The component peak data for all the spectra accumulated in this study, for a nominal Ru deposition of 1.5 nm, are presented in Table 3.1. Figure 3.1b is obtained by fitting the known C1s peak positions [69], followed by the deconvolution of the Ru3d$_{5/2}$,3d$_{3/2}$ doublet, using the expected 3:2 spin-orbit peak area ratio and a constant 3d$_{5/2}$-3d$_{3/2}$ peak component energy separation. We found, as mentioned earlier, that three Ru components were required, as in Zhang *et al.* and Chen *et al.* studies of Pt [70] and Pd [71], respectively. Their attributions are discussed below.

In addition, a new C1s component was required for depositions of 0.5 nm and above, its energy position (283.2 eV), identifying it as Ru-C$_n$, the result of Ru reacting with C; we do not know the value of n. Although this may represent a solution of C and Ru, which is known to occur, we refer to it as carbide. The metal components of carbides are normally found ~ 1 eV higher than the main peak; In this case, it is expected to fall under the Ru1 peak (see Table 3.1). That is, the atomic ratio of Ru1, in Table 3.1, is somewhat overestimated, with a commensurate change in the area ratios given above. This is discussed later.

The relative atomic percentages given in the right hand column of Table 3.1 are based on Ru3d$_{5/2}$. Because of their spin–orbit relationship, the same values are obtained for Ru3d$_{3/2}$. While atomic percentages differing by a few percent are obtained when based on the Ru3p or Ru3s spectra, those for the Ru3d spectra are deemed more precise because of their substantially higher relative magnitudes, as explained in the next sections.

Table 3.1: Peak components and attributions for a nominal deposition of 1.5 nm Ru evaporated onto HOPG.

Element	Label	Binding energy (eV)	FWHM (eV)	Identification	Relative atomic %
C1s	C1	284.6	1.0	Undamaged alternant hydrocarbon structure	12.8
	C2	286.1	1.6	Damaged alternant hydrocarbon structure	11.6
	C3	287.3	1.6	Free radical defects	4.5
	C4	288.9	3.5	Shake-up of C2	13.0
	C5	291.6	3.5	Shake-up of C1	8.3
	C6	282.7	1.5	Carbide	27.5
O1s	O1	529.4	1.8	Ru oxide	1.2
	O2	530.9	1.8	Ru oxide	1.9
	O3	532.5	1.8	C─OH	0.5
Ru3d$_{5/2}$	Ru1	279.6	1.1	Ru^0	13.6
	Ru2	280.5	1.1	Ru oxide	2.2
	Ru3	281.3	1.1	Ru oxide	1.2
Ru3d$_{3/2}$	Ru1'	283.8	1.1	Ru^0	*
	Ru2'	284.7	1.1	Ru oxide	
	Ru3'	285.5	1.1	Ru oxide	

Table 3.1: (Continued) Peak components and attributions for a nominal deposition of 1.5 nm Ru evaporated onto HOPG.

	Ru1	460.7	2.9	Ru^0	**

Ru3p$_{3/2}$	**Ru2**	**462.3**	**2.9**	**Ru oxide**	
	Ru3	**464.0**	**2.9**	**Ru oxide**	
Ru3s	**Ru1**	**585.4**	**8.9**	**Ru^0**	**
	Ru2	**593.8**	**8.9**	**Ru oxide**	
	Ru3	**599.3**	**8.9**	**Ru oxide**	
Valence band	**Ru5s**	**0.8**	**1.3**	**Ru 5s**	
	Ru4d$_{5/2}$	**2.2**	**2.7**	**Ru 4d$_{5/2}$**	
	Ru4d$_{3/2}$	**5.0**	**2.7**	**Ru 4d$_{3/2}$**	

*All relative atomic percentages are identical to those for Ru3d$_{5/2}$.

**All relative atomic percentages are similar to those for Ru3d$_{5/2}$ but are less precise (see text).

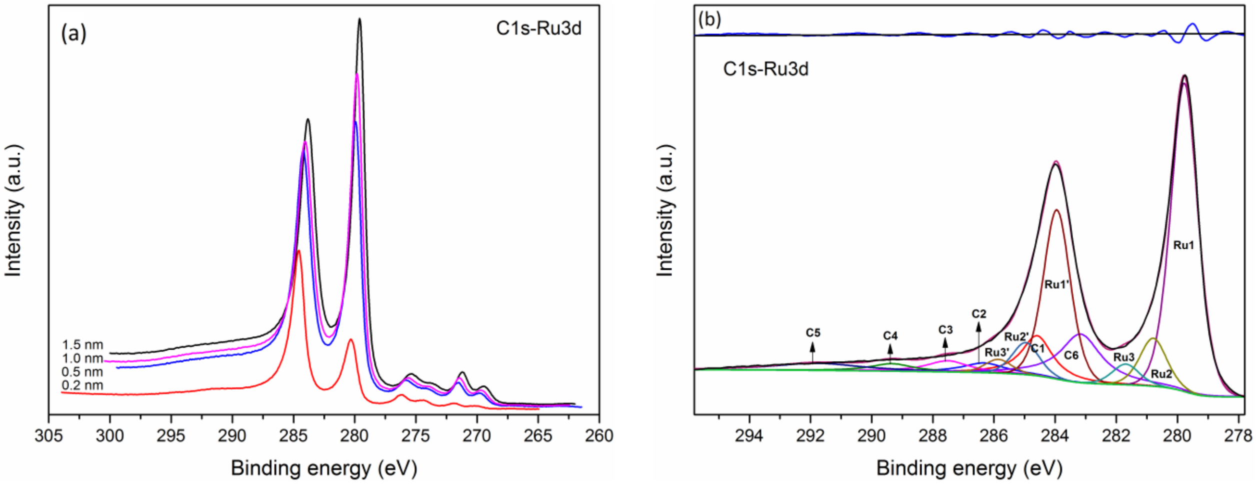

Figure 3.1: XPS spectra for Ru deposited onto HOPG. (a) Evolution of the C1s-Ru3d spectrum as a function of Ru thickness. (b) Deconvolution of the C1s - Ru3d spectrum for a nominal deposition of 1.5 nm. The residual is included, to show the goodness of fit.

3.3.3 A Comparison with Earlier Work – Lack of Electronic Structural Differences between Ru NP Surface and Volume

While we have found no evidence for the existence of a Ru NP surface layer having an electronic configuration different from that of the bulk, other authors [98, 99] have reported a "surface core level shift" (SCLS) for the Rud$_{5/2}$ component peak in Ru (0001) single crystals. Lizzit *et al.* [98] used a synchrotron source photon of 352 eV, giving photo-emitted electrons of ~ 50 eV, which have an attenuation length, λ, of ~ 5 Å. At their take-off angle of 40° from the horizontal, the probe depth, 3λ sin 40º, is just under 10 Å. Their energy resolution was < 0.08 eV. Their cleaned crystal had no measurable C1s or O1s components, and showed the sharp LEED pattern expected. Using Doniach-Šunjić (asymmetric) peak shapes, they found three components in the Ru3d$_{5/2}$ spectrum: S$_1$, attributed to the first layer of atoms, at ~ 279.7 eV; b, attributed to the bulk, at ~ 280.1 eV; S$_2$, attributed to the second layer of atoms, at ~ 280.3 eV. Weissenrieder *et al.* [99] also used a synchrotron, at a slightly higher photon energy, and confirmed the existence of the three Ru3d$_{5/2}$ components, at about the same energies. That is, the bulk-related peak is straddled by two smaller surface-related peaks.

It must be noted that there is a fundamental difference between the type of samples used to obtain these results, and ours. Their samples are single crystals, whose SCLSs arise because of the increasing asymmetry of atom-atom interactions of the surface layers, as compared to the volume. Energy minimization may involve contraction or expansion of the outer layers, but they remain commensurate with the layers beneath. In our case, using nanoparticles, this cannot be: because of the high radius of curvature, the bulk crystal is surrounded by outer layers that cannot remain commensurate. Indeed, in the case of Au nanoparticles [100], the model that best fit the size-dependent melting point data included a liquid-like outer layer, whose thickness was 6.2 Å, almost twice the van der Waals diameter. Thus, the nature of our NP surfaces precludes the types of interactions leading to the presence of SCLSs.

As noted above, the two groups that found SCLSs for Ru (0001) used asymmetric peaks to deconvolute their spectra. This appears to be an artifact, due to the fact that no background was subtracted from the data, as is commonly done. Because of this, the background on the lower binding energy side of the Rud$_{5/2}$ component peak is lower in amplitude than that at the higher binding energy side, and the component peak background used is merely an extension of the low binding energy side; in order to fill the space between the low binding energy extension and the actual data, asymmetric peaks must, *of necessity*, be used.

While we do not have access to the original data of Lizzit *et al.* [98], we used graphical means to duplicate them. We then subtracted a standard Shirley background, and fit the data with symmetric peaks; we discovered that the same three peaks found by the Lizzet group, at about the same binding energies, fit the data. It was similar use of background subtraction and symmetric peaks which led to the discovery that the asymmetry of the Co2p spectrum was caused by peaks pertaining to both Co_3O_4 and carbide contaminants at the Co NP surface [32].

3.3.4 Ru3p Spectra

The evolution of the Ru3p spectrum with deposition, at the higher deposition rate, is shown in Fig. 3.2a. The deconvolution of the Ru3p spectrum into symmetric components is shown in Fig. 3.2b. Again, three component peaks were necessary for the deconvolution. The difference in relative magnitudes from those for the 3d components is due to the lower precision associated with the less intense 3p peaks, as well as the difference in depths probed (~ 4 nm, compared to ~ 4.5 nm for Ru3d). Their area ratios, with less precision than for the 3d spectrum, are 1: 0.10: 0.04. Again, because of the presence of a Ru3p carbide contribution under the Ru1 peak, the area ratio of Ru1 is somewhat overestimated.

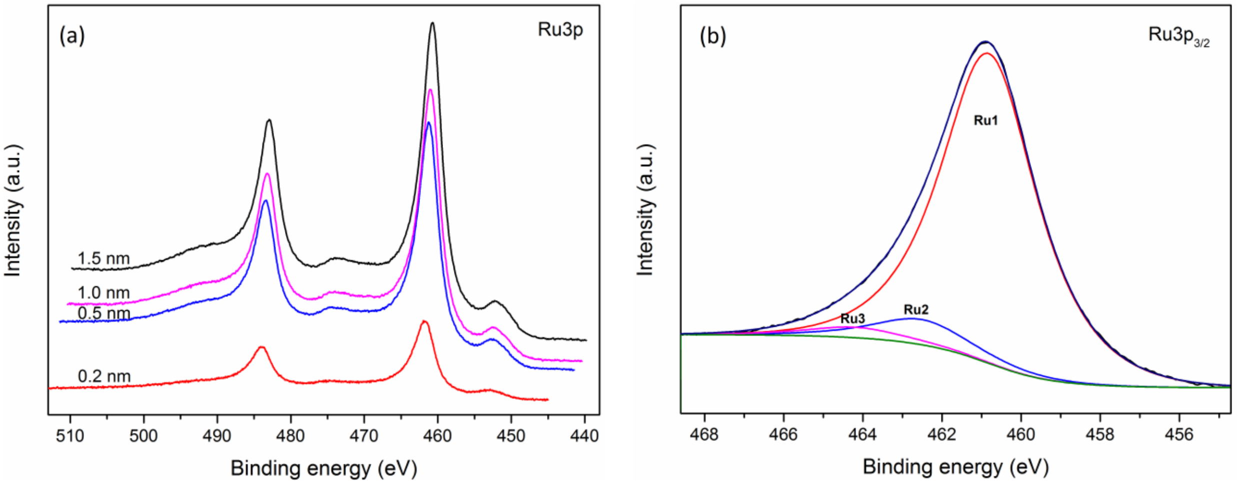

Figure 3.2: XPS spectra for Ru deposited onto HOPG. (a) Evolution of the Ru3p spectrum as a function of Ru thickness. (b) Deconvolution of the Ru3p spectrum for a nominal deposition of 1.5 nm.

3.3.5 Ru3s Spectra

The evolution of the Ru3s spectrum with deposition, at the higher deposition rate, is shown in Fig. 3.3a. As found for the other Ru core level spectra, that of Ru3s can also be separated into three symmetric components (Fig. 3.3b). The difference in relative magnitudes from those for the 3d and 3p components, is, as previously noted, due to the lower precision associated with the even less intense 3s peaks, as well as the difference in depths probed (~ 3.5 nm, compared to ~

4.5 nm for Ru3d). Their area ratios, with less precision than for the 3d and 3p spectra, are 1: 0.10: 0.08; here, too, the area of Ru1 is somewhat overestimated because of an unknown carbide contribution.

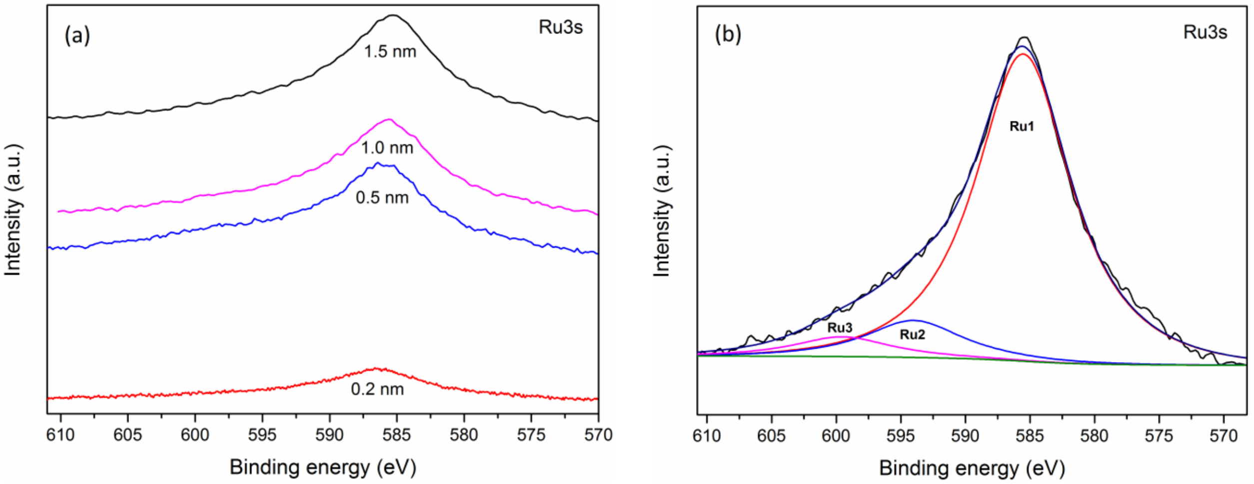

Figure 3.3: XPS spectra for Ru deposited onto HOPG. (a) Evolution of the Ru3s spectrum as a function of Ru thickness. (b) Deconvolution of the Ru3s spectrum for a nominal deposition of 1.5 nm.

3.3.6 O1s Spectra

The evolution of the spectrum is shown in Fig. 3.4a. Three components were found (Fig. 3.4b). The peaks at 529.97 and 531.38 eV (O1 and O2) are in an energy region where metal oxides are found, and that at 532.61 eV (O3), indicates C-OH. While the attributions of O1 and O2 will be discussed later, there are two possible sources of C-OH: the oxidation of the free radicals [68, 69, 74] created by fracturing the graphene structure [69, 101] when the HOPG is peeled prior to each experiment or the oxidation of adventitious carbon deposited onto the Ru NPs.

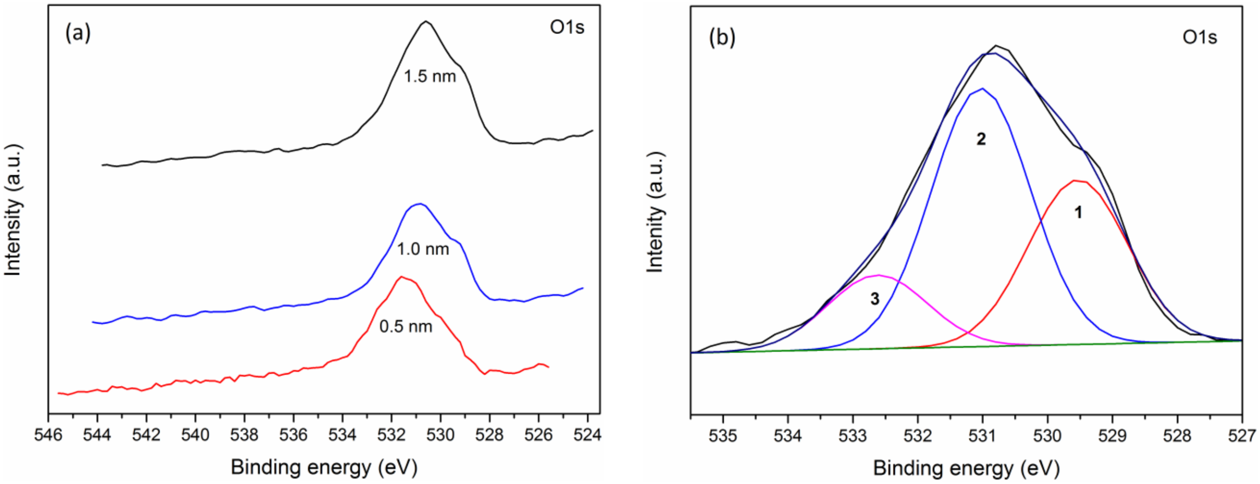

Figure 3.4: XPS spectra for Ru deposited onto HOPG. (a) Evolution of the O1s spectrum as a function of Ru thickness. (b) Deconvolution of the O1s spectrum for a nominal deposition of 1.5 nm.

3.3.7 Valence Band

The evolution of the spectrum is shown in Fig. 3.5a, where a decrease in the amount deposited results in a shift away from the Fermi level. This is believed to signal the opening of the Kubo gap at the Fermi level, as discussed below. As previously reported by Shen *et al.* [26], the spectrum was adequately fit with three components, as shown in Fig. 3.5b. In order of increasing binding energy, they were attributed [26] to Ru5s, $4d_{5/2}$ and $4d_{3/2}$ electron emissions.

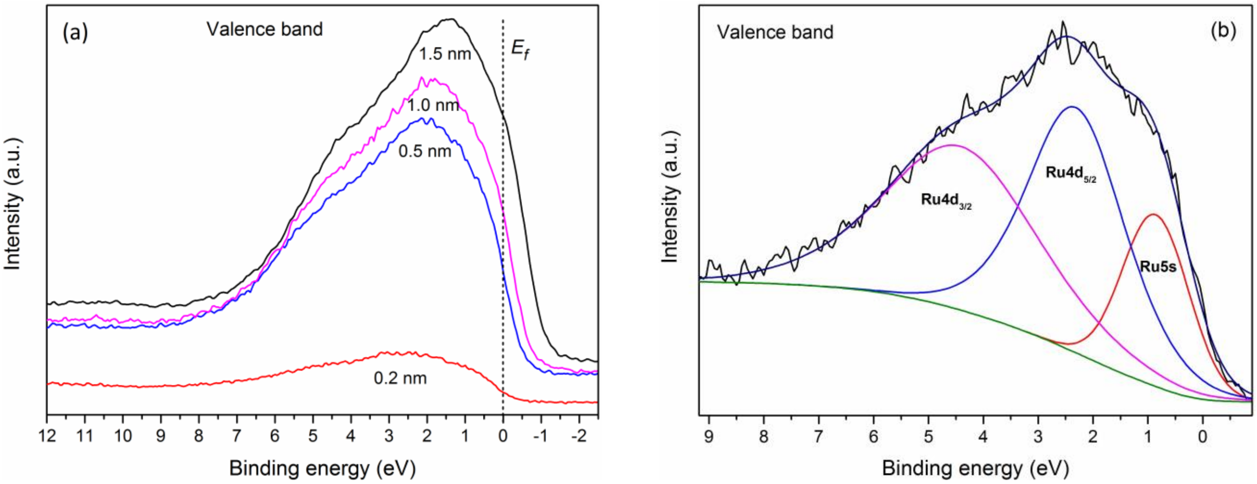

Figure 3.5: XPS spectra for Ru deposited onto HOPG. (a) Evolution of the valence band spectrum as a function of Ru thickness. (b) Deconvolution of the valence band spectrum for a nominal deposition of 0.25 nm.

3.3.8 XPS Analysis of Ru NPs as a Function of Deposition Rate

Nominal Ru thicknesses of 0.25 and 1.5 nm, deposited onto HOPG at both low (0.13 nm/min) and high (1.3 nm/min) deposition rates, were compared. No significant differences were observed in the positions and amplitudes of the core level and valence band spectra as a function of deposition rate.

3.3.9 XPS Analysis of Ru NPs as a Function of Nominal Thickness

Figure 3.6a presents the evolutions of the binding energies of the various C1s components and, Fig. 3.6b, their fwhm values, as a function of the nominal thickness of the Ru deposition. While peak C1 was fixed at 284.60 eV as a reference, the binding energies of C2-C5 show slight increases with Ru thickness. Figure 3.7a shows the Ru binding energies, and Fig. 3.7b, their fwhm values. The changes in Ru binding energy are in the opposite sense from those of C1s, suggesting a charge transfer from HOPG to the Ru NPs. We have noted similar behavior for Pt NPs deposited onto HOPG [69]. The fwhm values of the C1s peak components (Fig. 3.6b) remain constant with Ru deposition, while those of the Ru components (Fig. 3.7b) decrease sharply before leveling off, probably indicating the nominal thickness at which Ru NPs crystallize.

As noted, the C1s carbide peak (~283 eV) appears only at depositions greater than 0.25 nm. When it is present, the Ru1: Ru2: Ru3 atomic ratio (averaged over the 3d, 3p and 3s spectra) is 1: 0.13: 0.07. When it is absent (2.5 nm Ru deposition), the ratio is 0.60: 0.13: 0.07. That is, in the absence of carbide, the amplitude of the Ru1 component was reduced from 13.6 to 8.2 atomic percent, with the rest (5.4 atomic percent) being due to the overlapping Ru1 component of the carbide. We can now state that the Ru: C ratio in what we have been calling carbide is 5.2: 27.5 (Table 3.1), or 1: 5.3; this is clearly an overestimation because the Ru signal is attenuated by the deposited hydrocarbon over layer, whose thickness is unknown, and the true Ru contribution will be somewhat larger. In any case, this does not appear to constitute a true carbide and may, as we suggested earlier, represent a solution of C and Ru. Whether this solution exists in the interfacial region of the hydrocarbon layer or in that of the Ru NP surface is presently unknown.

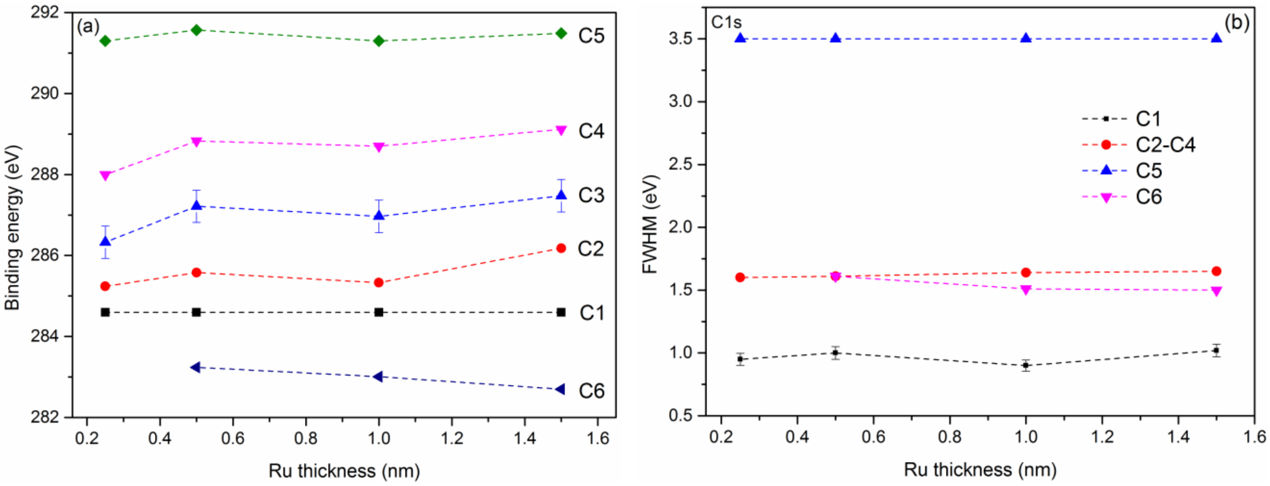

Figure 3.6: Evolutions of C1s binding energy (a), and fwhm (b), as a function of Ru thickness.

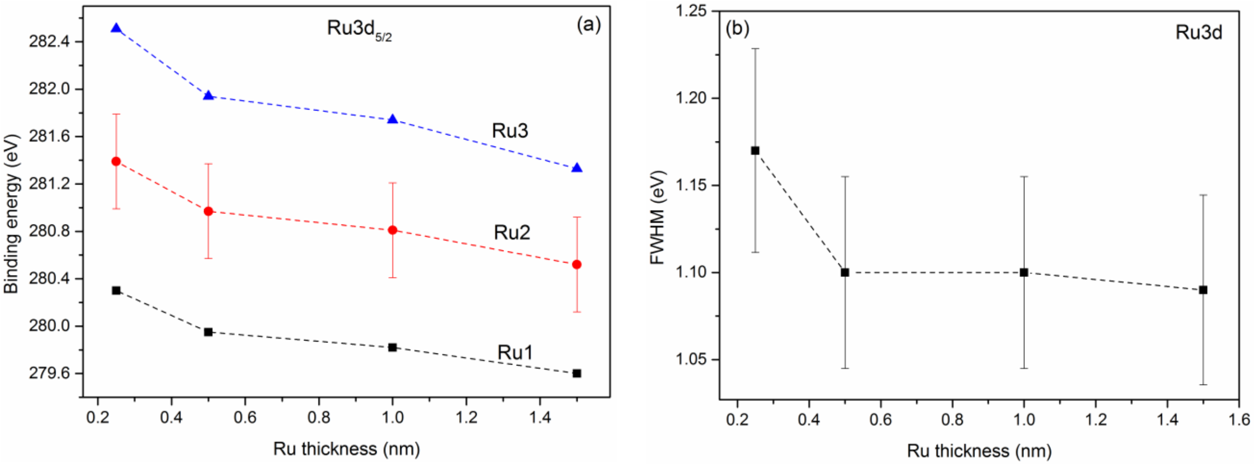

Figure 3.7: Evolutions of Ru3d binding energy (a), and fwhm (b), as a function of Ru thickness.

3.3.10 Ru NP Size and State of Aggregation

Figure 3.8 shows TEM photomicrographs of nominal 1.5 nm Ru transferred from fresh HOPG to Cu grids, after deposition at high (1.3 nm/min) and low (0.13 nm/min) rates. The EDX spectra in Fig. 3.9 confirm the identities of the NPs. The size distributions are illustrated in the histograms (Fig. 3.10), where the average diameters of high and low deposition rates are 4.3 ± 0.4 and 1.8 ± 0.25 nm width, respectively. The photomicrographs show that, at the higher deposition rate, larger, poorly separated (i.e., aggregated and partially coalesced) NPs were consistently found.

Smaller NPs were consistently found at the lower deposition rate, showing essentially no NP agglomeration or coalescence.

The aggregation and partial coalescence found at the higher deposition rate indicate that Ru is weakly bonded to the HOPG surface, despite the expected effect of the HOPG → NP electron transfer noted above. Such effects were observed for film growth in an electron microscope fifty years ago [102] and explained theoretically a decade ago [103], as due to the heat of condensation, that is, the heat released by the substance on condensation of the metal vapor, to compensate for the drop in entropy [104]. At the higher temperatures provided by the more rapid liberation of the Ru heat of condensation on deposition (~ 600 kJ mol^{-1}), the NPs have sufficient energy to diffuse laterally across the surface, but not enough to melt the nanoparticles completely. Only coalescence or partial coalescence occurs. Thus, the nanoparticles are capable of reaching a more stable configuration, in order to decrease the surface energy [103]. Lateral diffusion and coalescence of particles on the substrate was found in previous studies by our group [105-107] of copper (Cu) deposited onto both HOPG and Dow Cyclotene, a low permittivity polymer. It was found that Cu does not diffuse into the volume; rather it diffuses laterally on the substrate, to form larger clusters, at room temperature and even on prolonged annealing. Again, this indicates the poor adhesion and the weak interfacial interactions between nanoparticles and certain substrates.

This tendency for Ru NPs to diffuse is well known, and several studies have been published, specifying methods to minimize it; these include activating the carbon support by creating nucleation sites at the surface, such as by ion bombardment [92, 93], which may be followed by an oxidation process [31, 94], and Ar$^+$ bombardment of the surface prior to NP deposition, using a magnetron-sputter gas-aggregation source [28], which deposit metals at a higher deposition rate than the e-beam evaporator in our XPS instrument.

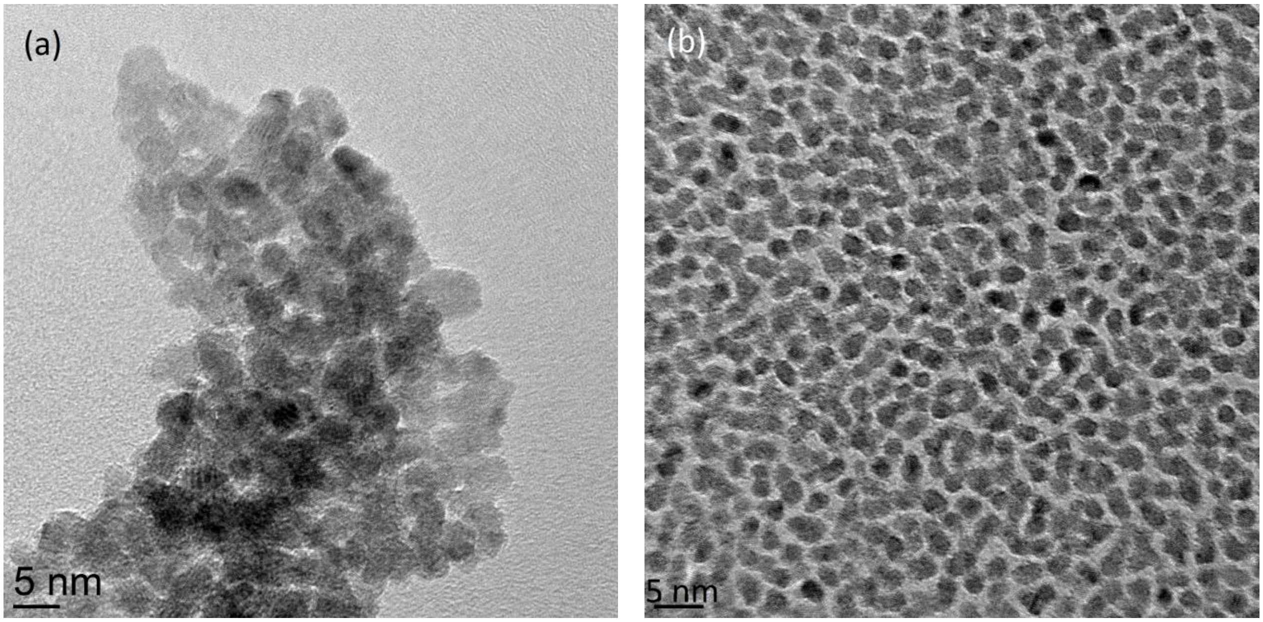

Figure 3.8: TEM photomicrographs of nominal 1.5 nm Ru NPs evaporated at (a) high (1.3 nm/min), and (b) low (0.13 nm/min) deposition rates.

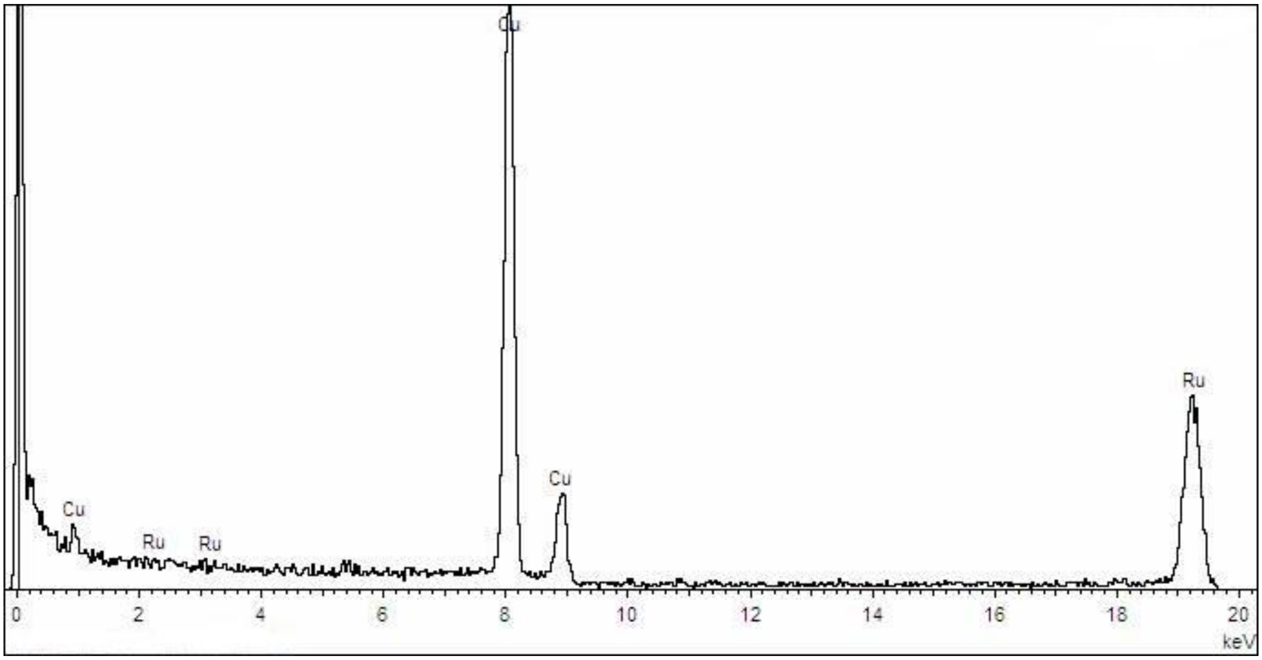

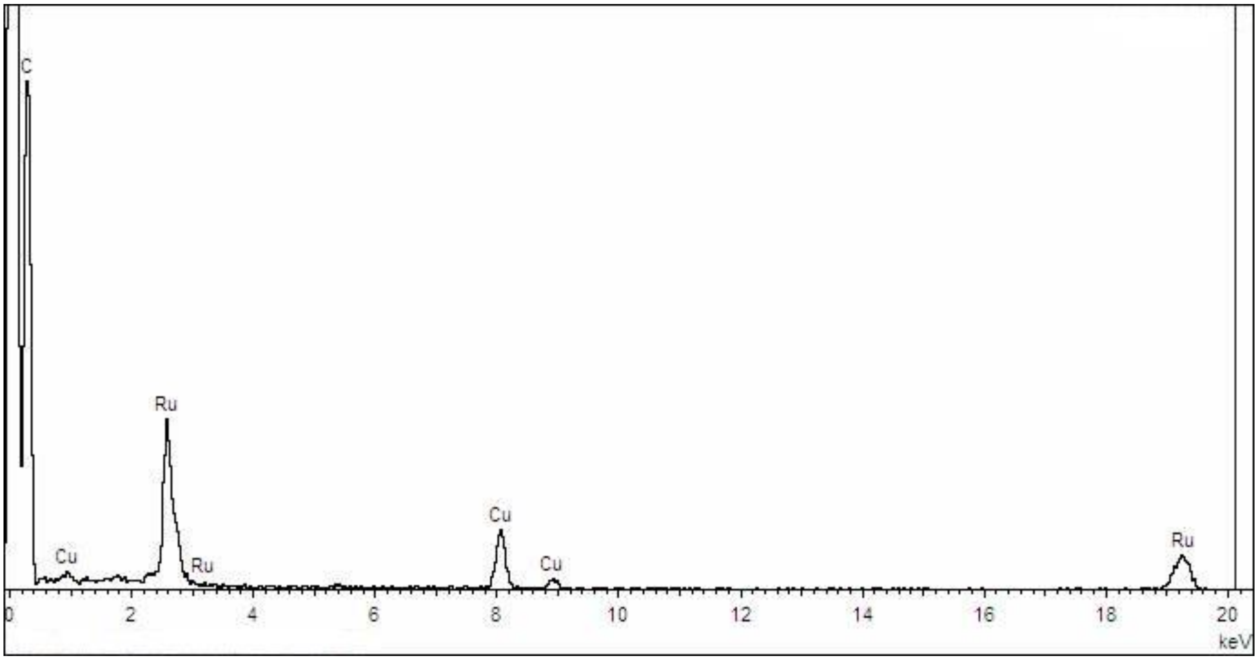

Figure 3.9: EDX spectra of the Ru nanoparticles shown in Figure 3.8. The Cu peaks come from the support grid.

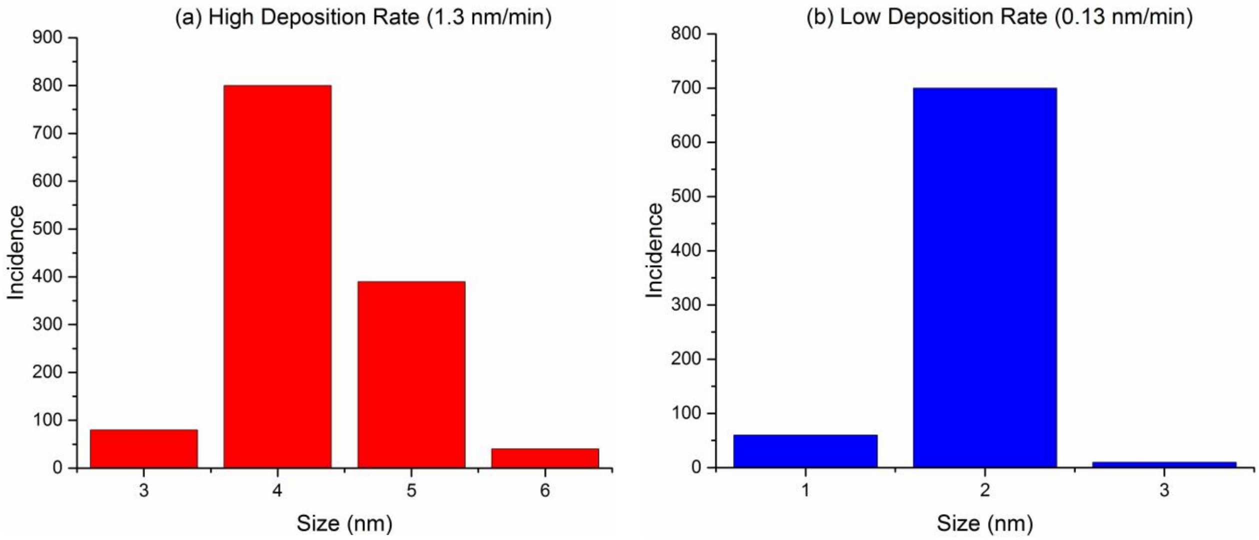

Figure 3.10: Size distributions of Ru NPs deposited onto HOPG at: (a) high, (b) low deposition rates.

3.4 Discussion

3.4.1 Ru Nanoparticle Reaction with Residual Gases.

Ru NPs are capable of reacting with residual gases, such as hydrocarbons, water vapor and oxygen, which are present in trace amounts, even under UHV conditions. Water vapor and oxygen are certainly the only sources available for the formations of the various peaks found in the O1s spectrum. The presence of trace residual hydrocarbons is most probably the principal source of carbide formation since, as mentioned earlier, the ready diffusion of Ru NPs precludes Ru-HOPG covalent bond formation; such bond formation would have prevented diffusion, as in our group prior studies [32, 68-71]. At the interface, Ru NPs react with residual hydrocarbon, under the influence of the heat released by NP condensation, to form carbide. Figure 3.11 shows the evolution of the carbide formed, which appears at depositions above 0.25 nm, when the rate and amount of heat production are sufficiently elevated to provoke this reaction. This carbide exists as a surface layer around each NP and, as in Fe study of Yang and Sacher [95], acts as a protective coating, limiting NP coalescence but not lateral diffusion, again indicating weak substrate bonding. This layer is also the source of the C-OH peak, appearing in the O1s spectrum at ~ 532.5 eV in Table 3.1; the corresponding C1s peak falls at ~ 286 eV, where HOPG already has a component peak.

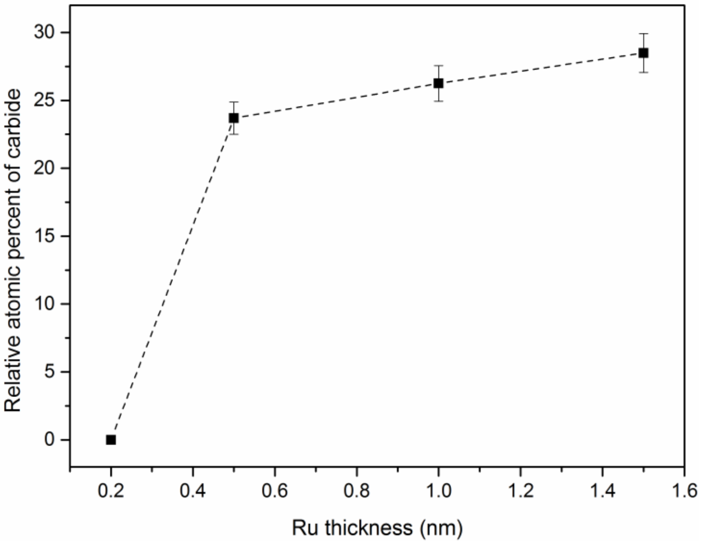

Figure 3.11: Evolution of the carbide content as a function of Ru thickness.

3.4.2 Relationships among the Ru components

The Ru3:Ru1 area ratio (both $d_{3/2}$ and $d_{5/2}$ give the same result), shown in Fig. 3.12, remains constant, indicating that the two components are directly associated. This was also found in Zhang *et al.* and Chen *et al.* studies of Pt [70] and Pd [71], respectively, where the metal 1 component was attributed to zerovalent metal at the NP surface, and metal 3, to the surface metal oxide. In both those cases, the metal 2 component was attributed to zerovalent metal in the NP volume; it was already known that both Pt and Pd have different electronic structures for their surface and volume components. In corroboration of the surface/volume attributions, the surface:volume ratios of both Pt and Pd decreased with increasing NP size, as expected.

While we have not found any prior literature references to differences in electronic structure between Ru NP surface and volume, other authors [98, 99] have found a “surface core level shift” (SCLS) for the $Rud_{5/2}$ component peak in Ru (0001) single crystals. As discussed in Appendix A, this does not apply to our situation. Further, as shown in Fig. 3.12, the Ru2:Ru1 area ratio *decreases slightly* with Ru deposition, which is the opposite of what is expected for surface: volume components, except for a flattened NP, whose growth involves adding surface rather than volume. As seen in Fig. 3.8, this is certainly not the case. Rather, we attribute this component to another Ru surface species, whose identification is discussed below.

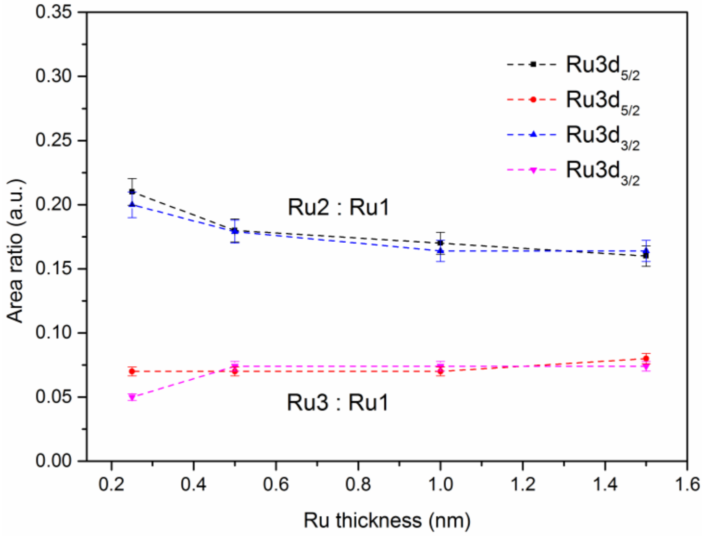

Figure 3.12: Evolutions of Ru2:Ru1 and Ru3:Ru1 area ratios, as functions of Ru thickness.

3.4.3 Initial oxidation of Ru NPs

We have found that the Ru3:O1 ratio is constant as a function of nominal thickness, at ~ 1: 1, which indicates that RuO is *initially* formed on the NP surface, although the final oxidation product is known to be RuO_2 [17]. Our result is in agreement with those of Pelliccione *et al.* [96], who found this ratio for Ru electrodeposited onto Pt NPs: at the lowest potentials used, the initially formed Ru:O ratio is 1:1, which converts to 1:2 (RuO_2) on increasing the potential. This possibility was also suggested by Herd *et al.* [108].

In our search for an explanation of the Ru2 component, we constructed correlation plots of all the Ru and O components as a function of the amount deposited. As may be seen from Fig. 3.12, the Ru3:Ru1 ratio is constant as a function of deposition, while the Ru2:Ru1 ratio quickly becomes so, indicating that both are surface-related. In addition, Fig. 3.13 shows that the Ru3:O1 and Ru2:O2 ratios quickly become constant at values of 1:1 and 1.3:1, respectively, indicating that both represent surface oxides, and the Ru3: Ru2 ratio, as shown in Fig. 3.13, is 0.5: 1. We note that this constancy supports our contention that the carbide component does not materially contribute to Ru2 or Ru3.

It appears, then, that two oxides are simultaneously formed, rather than one, having an overall Ru: O ratio in close proximity to 1: 1. Their difference lies in the fact that the Ru3-O1 oxide is more ionic than the Ru2-O2 oxide, as shown by the positions of the binding energy peaks. This may argue for the formation of a complex, mixed-valence oxide on the Ru NP surface. On further oxidation, this eventually becomes RuO_2, known to form on complete oxidation [97]. We note the existence of other examples of mixed-valence oxidized Ru species present in larger complexes [109], such as Ruthenium Red ($Ru_3O_2N_{14}Cl_6H_{42}$, ammoniated ruthenium oxychloride). Other mixed-valence Ru complexes are also known [110]. Further, although a different explanation was offered, a recent paper on the initial oxidation of Rh NPs [111] reported two O1s metal oxide peaks with associated $Rh3d_{5/2}$ component peaks.

While both RuO_3 [97, 112] and RuO_4 [26] have been posited as being present during Ru oxidation, it is doubtful that the former exists under our experimental conditions [113], and the latter, with its high vapor pressure, evaporates quickly under vacuum.

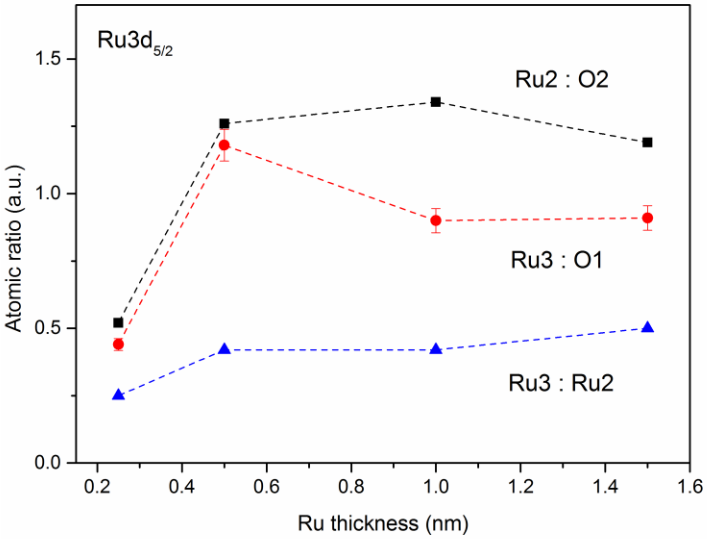

Figure 3.13: Evolutions of Ru2:O2, Ru3:O1, and Ru3:Ru2 atomic ratios, as functions of Ru thickness.

3.4.4 Valence Band Electronic Configuration

The positions of all core level spectra remain constant as a function of Ru thickness. However, in the case of the valence band spectra, the binding energies of the three components decrease with increasing deposition. Indeed, they are linear when plotted against the reciprocal of the amount deposited (Fig. 3.14); the use of the amount deposited as a variable, rather than NP size, was necessitated by the fact that the NPs deposited are not spherical, and do not lend themselves to any truly quantitative measurement of size. In fact, in deriving his theory of the gap, Kubo used the concept of nuclearity (the number of atoms in the NP), so as to avoid problems in describing size [114].

The spectra shift away from the Fermi level as the amount deposited decreases, as may be seen in Fig. 3.5a. This indicates that metallicity is ultimately lost with decreasing NP size. The response to a change in dimensions seen in Fig. 3.14 is expected for an increase in the Kubo gap at the Fermi level [115]. Vijayakrishnan *et al*. [116] found similar results for Pd and Ag NPs, and asked, but did not answer, whether initial-state effects have a significant role in the increase of the Kubo gap. Based on Yang and Sacher work [117], we can answer this question in the affirmative: initial-state effects were found to vary in the manner shown in Fig. 3.14 while final-state effects vary in the opposite sense.

As noted in Zhang *et al.* and Chen *et al.* studies of Pt [70] and Pd [71], experimental evidence, in the literature, indicates that the electronic structure of the NP surface differs from that of the volume. References found there indicate that, in both cases, there was an electron transfer, from d to s orbitals, on going from volume to surface. While this does not happen in the present case (the deconvolution of Ru$d_{5/2}$ does not show a difference in surface and volume components), we have used our valence band data to discern what happens when the NP becomes small enough that surface atoms form a significant fraction of the total number of atoms. A plot of the 5s: 4d peak area ratio is shown in Fig. 3.15, where it may be seen that, as the amount of Ru deposited decreases, and the surface content increases, so does the 5s orbital content. We note that this occurs abruptly, exactly where the Kubo gap increases to where the electron density of states at the Fermi level becomes zero (Fig. 3.5a) and the NP, non-metallic; this is exactly the condition under which a carbide component does not form. The loss of d orbital electron density is referred to [118] as spill-over (or spill-out), and has been theoretically attributed to the decrease in surface lattice parameters with decreasing NP size [119, 120]. However, with surface oxide and a carbon layer surrounding the NPs, that explanation does not appear to apply here.

Recent papers on the use of Ru NPs in sensors [121], hydrogenation catalysts [122] and Li-O_2 batteries [123] indicate their sizes to be in the range of 1-6 nm, roughly the size of the NPs characterized here. Our results show that, whatever the substrate and extent of atmospheric exposure, the NP surface will be partially oxidized with a mixed valence oxide, and it will be metallic, with most of the valence electron density residing in the 4d orbitals. On carbon-based substrates, such as HOPG, carbon fibers or carbon nanotubes, NP bonding to the substrate is expected to be weak, with surface diffusion occurring. In the presence of residual hydrocarbon vapor, the NP surface will be covered with a hydrocarbon layer, limiting surface contact and resultant coalescence.

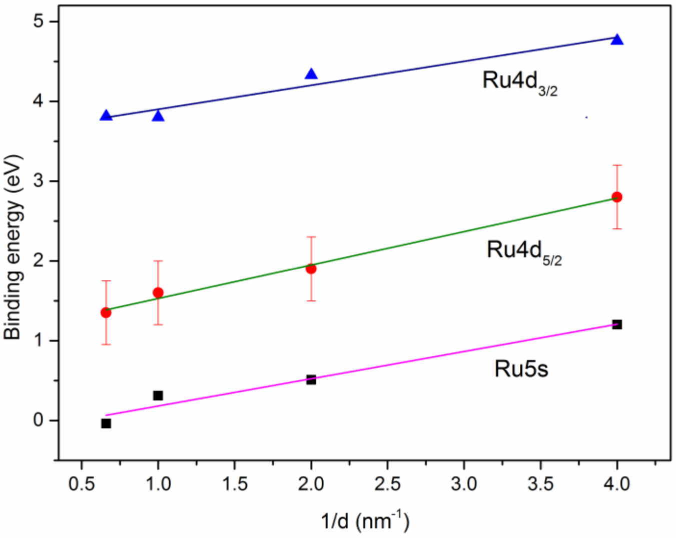

Figure 3.14: Evolution of the valence band binding energy as a function of inverse Ru thickness.

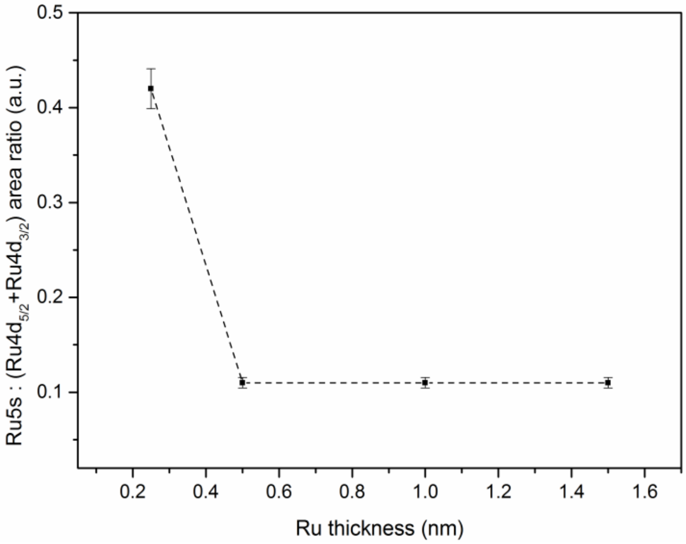

Figure 3.15: Evolution of the 5s/4d area ratio, as a function of Ru thickness.

3.5 Conclusions

XPS characterizations were carried out on Ru NPs, for two deposition rates and for various amounts deposited onto freshly cleaved HOPG surfaces. The NP surface was shown to possess a mixed valence Ru oxide, as well as a hydrocarbon layer from residual gas hydrocarbons present in the vacuum. TEM photomicrographs showed the aggregation and partial coalescence of Ru NPs deposited at the higher deposition rate, as the Ru NP condensation energy was released too rapidly to dissipate; such diffusion indicates weak bonding of the NPs to the HOPG surface, permitting lateral NP diffusion across the surface, as well as partial oxidation of the hydrocarbon layer forming around the NPs. The analysis of the valence band indicates an increase in the Kubo gap with decreasing NP size, accompanied by an abrupt electron spill-over from the 4d to the 5s orbitals at the point at which the electron density of states at the Fermi level becomes zero. This detailed information, obtained from our use of symmetrical peak component XPS analysis, is of potential importance in the use of Ru NPs as sensors and catalysts.

CHAPTER 4 STRUCTURE OF PLATINUM-RUTHENIUM ALLOY NANOPARTICLES DEPOSITED ONTO HIGHLY ORIENTED PYROLYTIC GRAPHITE, AND THEIR EVOLUTION WITH ANNEALING

4.1 Introduction

With regard to the best catalytic performance of PtRu NPs, in PEMFC and DMFC, as discussed in Chapter 1, a detailed study of their preparation and characterization methods is still lacking. There are several contradictory claims [3-7] on PtRu NP structure in the literature, as to which metal covers the NP surface and which oxides are formed, for example. These led us to prepare and characterize highly pure PtRu alloy NPs, using physical evaporation. This precludes surface contamination by chemical fragments of the reducing agent used in chemical reduction of metal salts, as has frequently been done.

Here, we describe the preparation methods used, followed by a presentation of the surface and bulk characterization techniques. In order to understand alloying behavior, and the structures of the alloys formed, we used three different orders of deposition: Pt evaporated onto Ru, Ru evaporated onto Pt and the simultaneous evaporation of both metals; none of the methods wets HOPG surface used, and all the deposits retract to form NPs. As we shall show, each deposit gives a different structure, each of which is affected differently by annealing.

XPS helped us to distinguish the differences in the chemical and physical environment of each element in the alloy. Here, again, our treatment of the spectra uses symmetric peak components. By using the quantitative capacity of XPS, relative concentrations of each component of an element are obtained. TOF-SIMS detects charged fragments sputtered from the near surface (1-2 nm) region, from which the surface composition and chemical species may be determined. In addition, in order to investigate the various phases, the internal crystal structures, and elemental distributions of the NPs, HAADF/ STEM and EELS were employed. A comprehensive discussion of these findings is presented in this chapter.

4.2 Experimental

4.2.1 Sample Preparation

Following our earlier studies [1, 124] of pure Ru and Pt NPs deposited onto HOPG (grade ZYA, SPI, Inc.), we prepared PtRu NPs on the same substrate, using three different orders of deposition: Pt was evaporated onto previously deposited Ru (deposit 1), the two metals were evaporated simultaneously (deposit 2), and Ru was evaporated onto previously deposited Pt (deposit 3). All the evaporations were carried out in the preparation chamber of a VG ESCALab 3 MARK II XPS spectrometer (Thermo VG Scientific), at a pressure of $< 3 \times 10^{-8}$ Torr, using a Quad-EVC evaporator (Mantis Deposition, Ltd.) containing high purity Ru and Pt rod targets (American Elements) and a tungsten filament e-beam source. For all these deposits, we attempted to keep a 1:1 mass ratio, depositing 0.9 nm of Pt and 1 nm of Ru, by keeping the deposition rate unchanged. The nominal thicknesses of both Ru and Pt were monitored using a quartz crystal microbalance placed near the sample.

High-resolution transmission electron microscopy (HR-TEM) was performed on each deposit after annealing (not shown); confirming the formation of NPs at the HOPG surface, even after annealing, as expected. This is because the low deposition rate (0.13 nm/min) of the e-beam evaporator gives sufficient time for the condensation energy to dissipate, avoiding any possible surface diffusion, such as was found for pure Ru [124].

4.2.2 XPS Measurements, Annealing, and XPS Data Analysis

After deposition at room temperature, the samples were transferred to the analysis chamber of the XPS, without exposure to atmosphere. *In-situ* XPS was performed in this chamber, at a base pressure of $< 2 \times 10^{-9}$ Torr, using non-monochromated Mg Kα radiation (1253.6 eV). High-resolution spectra were obtained at a perpendicular takeoff angle, using a pass energy of 20 eV (step size: 0.05 eV; step dwell time: 200 ms). The instrument resolution was 0.7 eV. Core level spectra were obtained for the Ru3d, Pt4f, C1s, and O1s electron emissions, and valence band spectra were obtained for the Ru4d,5s and Pt 5d,6s emissions.

Following XPS measurements, the samples were returned to the preparation chamber, and placed on an annealing stage (VG Scientific Model 240), where they were annealed in steps, 1 h for each step, at temperatures ranging from ~ 150° to ~ 715°C. After each step, they were cooled to room temperature and remeasured by XPS. The XPS spectra were analyzed using symmetric peak components, as discussed above.

In analyzing the data obtained from XPS, after Shirley background removal, the component peaks were separated with the VG Avantage software, using mixed Gaussian-Lorentzian functions. The binding energy was calibrated by placing the principal C1s peak at 284.6 eV; this commonly used procedure adjusts the energy scale, precisely locating the binding energy positions of both core and valence spectra, as well as the position of the Fermi level.

The peak widths employed in the component separations, given as fwhm, were those found in our earlier studies [124, 125]. Relative concentrations were obtained from high resolution spectra, using sensitivity factors regularly confirmed with standard samples.

4.2.3 TOF-SIMS Analysis

For TOF-SIMS, HAADF/STEM and EELS, it was necessary to transfer samples from the XPS chamber to these instruments. These techniques were applied to as-prepared samples and to samples which had been annealed at approximately 650°C. Since TOF-SIMS is more highly surface sensitive than XPS, samples for these measurements were transported in a VG vacuum transfer device that could be coupled to both systems, at a pressure of $<1 \times 10^{-6}$ Torr. These samples were measured in an ION-TOF TOF-SIMS IV mass spectrometer, with a mono-isotopic Bi^+ beam and mass resolution $(M/\Delta M) \geq 8000$. Spectral mapping of the samples was performed over an area 50 µm × 50 µm, with 256 × 256 pixel resolution, under a beam voltage of 25 kV, a beam current of 2.0 nA in bunch mode, and a beam diameter of 0.34 µm.

TOF-SIMS spectra were obtained from three different sites on each of the samples. Due to surface charging, signals, especially in negative mode, were somewhat unstable. The two most abundant isotopes of each metal were considered. Ru fragmental yields were greater in positive mode, and Pt fragmental yields, in negative mode. The relative yields of these metals, which define their ease of fragmentation, were found to be in the ratio of ~ 3:2.

4.2.4 HAADF/STEM and EELS Analysis

Since STEM and EELS are essentially bulk measurements, it was not necessary to transfer samples under vacuum. They were, nonetheless, observed as soon as possible after the preparation.

HAADF/STEM and EELS experiments were carried out on a FEI Titan 80-300 cubed microscope, equipped with a Gatan EELS spectrometer (Quantum model) and a high-brightness field emission source operated at 300KV. Samples were either collected by scraping flakes from the HOPG graphite, to observe the morphology of particles in plan view, or by sectioning, using a focused ion beam (Zeiss model NVision 40), after a protective carbon layer was electron-beam deposited onto the Pt/Ru layer surfaces prior to a W layer deposition. HAADF imaging was used to reveal the atomic-number contrast of the structures (Pt having a significantly higher atomic number than Ru), with additional spectroscopic imaging with EELS used to reveal the distribution of Pt and Ru complementing the HAADF images.

4.3 XPS Results and Discussion

4.3.1 Core Level Spectra

As in our previous studies, symmetric peak components were employed to analyze the most intense peaks of Ru and Pt, Ru3d and Pt4f, as well as the C1s and O1s spectra. To compare the deconvolutions of pure Pt and Ru with the PtRu NPs, Tables 4.1 and 4.2 present all the pure metal attributions that we obtained, repeating our previous studies on the pure metals [1, 124]. The number of symmetric components for each XP spectrum in PtRu NPs is identical to that of pure metals, except in the O1s spectra: depending on the order of metal deposition, the O1s spectrum could be deconvoluted into two or three components. The XP spectra of PtRu NPs appear at slightly higher energies than those of the pure metals, and the intensities, atomic ratios, and some attributions of PtRu NPs differ from those of the pure metals, as explained below.

For the three methods of deposition, the C1s, Ru3d, and Pt4f spectra were deconvoluted like those of the pure metals, yielding the same numbers of symmetric components. However, the O1s spectra were deconvoluted into two components in deposit 1, and three components in deposits 2 and 3. The intensities, atomic rations, and attributions of all the spectra differ from the one deposit to another, and they vary as a function of annealing temperature. The peak components of the C1s, Ru3d, Pt4f and O1s spectra, for deposit 1 at room temperature, are shown in Fig. 4.1.

As was found for pure Ru [124], the C1s and Ru3d spectra overlap and were deconvoluted simultaneously. The C1s spectra were found to be composed of six peaks. Except for the carbide peak, as observed in our previous Ru study [124], all the C1s peaks have the same positions as those for pristine HOPG. As we demonstrated in that study [124], the carbide peak intensity increased with increasing deposition. In the case of PtRu, as more Ru diffuses to the surface (see later), more carbide appears; however, due to the simultaneous presence of Pt, the amount of carbide is less than that of pure Ru at the same extent of deposition. The slight changes in the position of carbide in PtRu NPs, compared to pure Ru, are less than the resolution of our instrument, 0.7 eV. A list of peak components and attributions of all elements, for all three deposits, are presented and discussed in Section 7.

Because of the overlap of the O1s and the Pt4p$_{3/2}$ spectra, they, too, were deconvoluted simultaneously. The O1s spectrum (Fig. 4.1b) was fit with two components (see Table 4.4), the one at the lower binding energy indicating a metal oxide, and the other indicating an oxidized carbon species. Figure 4.1c also shows the deconvolution of the Pt4p$_{3/2}$ spectrum into three symmetric components.

As found in our previous Ru and Pt studies [1, 124], any Ru and Pt oxides, formed due to the presence of residual oxygen, decompose at temperatures above 350ºC. The disappearance of the O1s metal oxide peak, as a function of annealing temperature, is presented in Fig. 4.2a. Figure 4.2b shows the evolution of the atomic percentages of the two components, as a function of annealing temperature; O1 tends toward zero with increasing temperature, while O2, an organic oxide, suffers an even greater decrease, although not to zero. Similar changes were observed in deposits 2 and 3.

Each of the Ru3d and Pt4f spectral doublets was deconvoluted into three symmetric components, as indicated in Fig. 4.1a and c. There are some differences between their attributions here and those for pure Pt [1] and Ru [124]. Their binding energies are somewhat higher than those of the pure metals, indicating an interaction between Pt and Ru during annealing. For example, in the case of pure Ru [124], the Ru2 and Ru3 components were found to be due to two different metal oxides on the NP surface, having corresponding components in the O1s spectrum. However, here we have only one metallic oxide component, O1, which, as we discuss below, is attributed to a mixed PtRu oxide, necessitating different attributions for Ru2 and Ru3. We also found that the attributions of some Ru and Pt components changed, as a function of annealing temperature; these are discussed below.

Table 4.1: Peak components and attributions for a nominal deposition of 15 nm Ru evaporated onto HOPG, identical to those previously found for Ru [124].

Element	Label	Binding energy (eV)	Identification
C1s	C1	284.6	Undamaged alternant hydrocarbon structure
	C2	285.6	Damaged alternant hydrocarbon structure
	C3	286.5	Free radical defects
	C4	288.2	Shake-up of C2
	C5	291.3	Shake-up of C1
	C6	283.6	Carbide
O1s	O1	530.0	Ru oxide
	O2	531.8	Ru oxide
	O3	533.2	C–OH
$Ru3d_{5/2}$	Ru1	280.1	Ru^0
	Ru2	280.8	Ru oxide
	Ru3	281.7	Ru oxide
$Ru3d_{3/2}$	Ru1'	284.3	Ru^0
	Ru2'	285.0	Ru oxide
	Ru3'	286.0	Ru oxide

Table 4.2: Peak components and attributions for a nominal deposition of 15 nm Pt evaporated onto HOPG, identical to those previously found for Pt [1]; the peak components of C1s spectrum are identical to those for pure Ru, in Table 4.1.

Element	Label	Binding energy (eV)	Identification
O1s	O1	530.8	Pt oxide
	O2	532.7	C–OH

Table 4.2: (Continued) Peak components and attributions for a nominal deposition of 15 nm Pt evaporated onto HOPG, identical to those previously found for Pt [1]; the peak components of C1s spectrum are identical to those for pure Ru, in Table 4.1.

	Pt1	71.3	Pt at surface

$Pt4f_{7/2}$	**Pt2**	**72.2**	**Pt in volume**
	Pt3	**73.2**	**Pt oxide**
$Pt4f_{5/2}$	**Pt1'**	**74.7**	**Pt at surface**
	Pt2'	**75.5**	**Pt in volume**
	Pt3'	**76.6**	**Pt oxide**

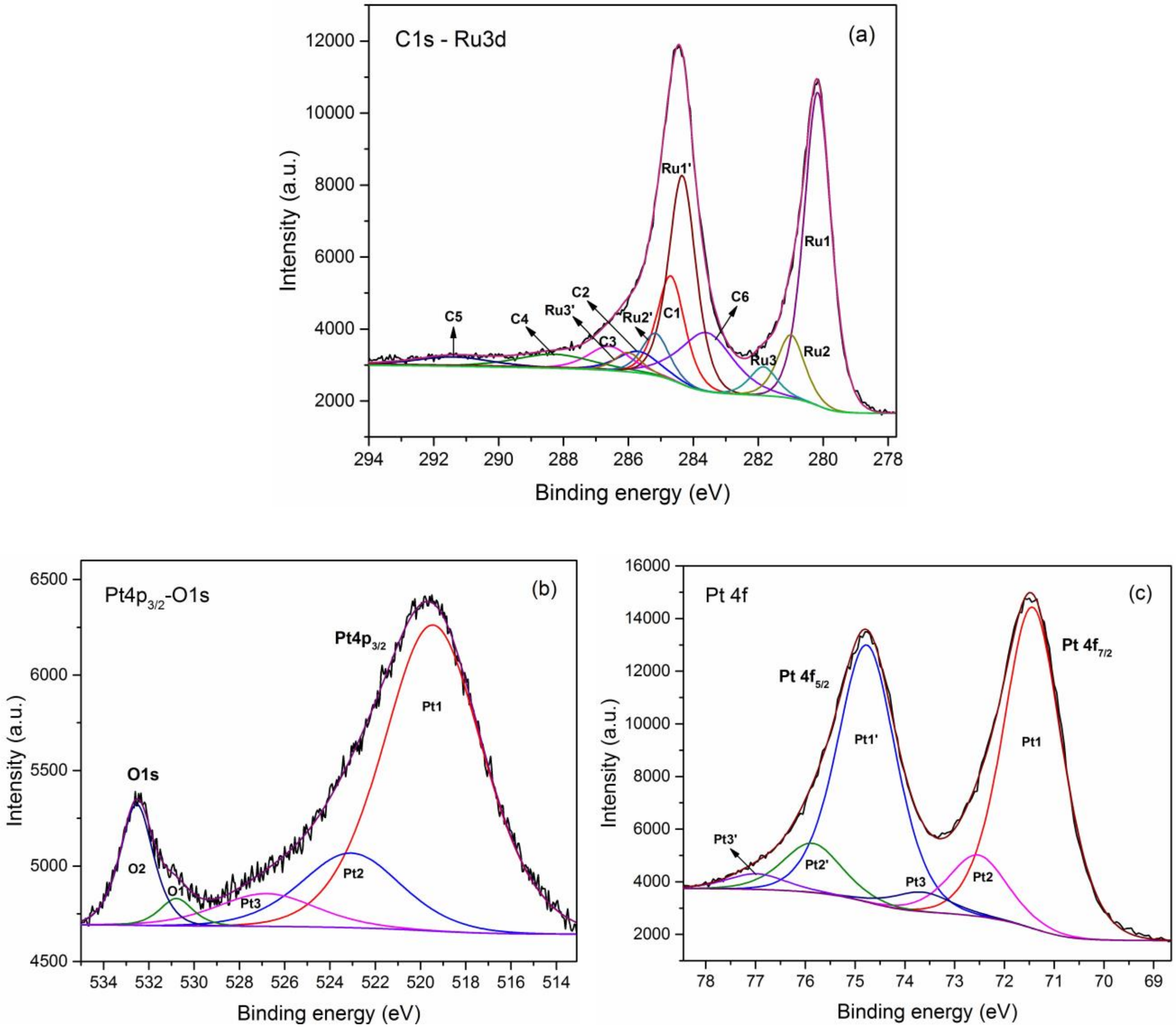

Figure 4.1: XPS spectra for Pt deposited on Ru (1:1 mass ratio) onto HOPG (deposit 1) at room temperature. Schematic deconvolutions of the (a) C1s-Ru3d, (b) Pt4p3/2-O1s, (c) Pt4f.

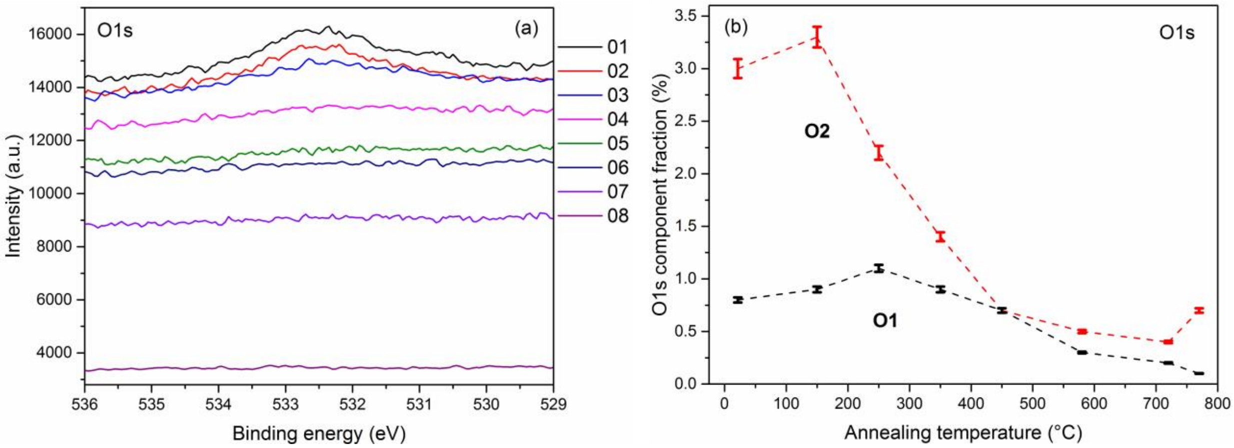

Figure 4.2: (a) Evolution of the O1s spectrum (01 represents the sample at room temperature and 08 is at the highest temperature), (b) Evolution of the O1s component fractions, both for deposit 1, after annealing at each indicated temperature for 1 h.

4.3.1.1 Deposit 1

The evolution of the binding energy, full widths at half maxima, and atomic ratios of the XPS peak components were evaluated, in order to determine how they are affected by annealing, and what they reveal about electronic properties and structure. Figure 4.3 shows the evolution of the binding energies of the Ru $3d_{5/2}$ and Pt $4f_{7/2}$ components. Particularly for the Pt $4f_{7/2}$ spectrum, there are changes observed at both 350º and 715°C.

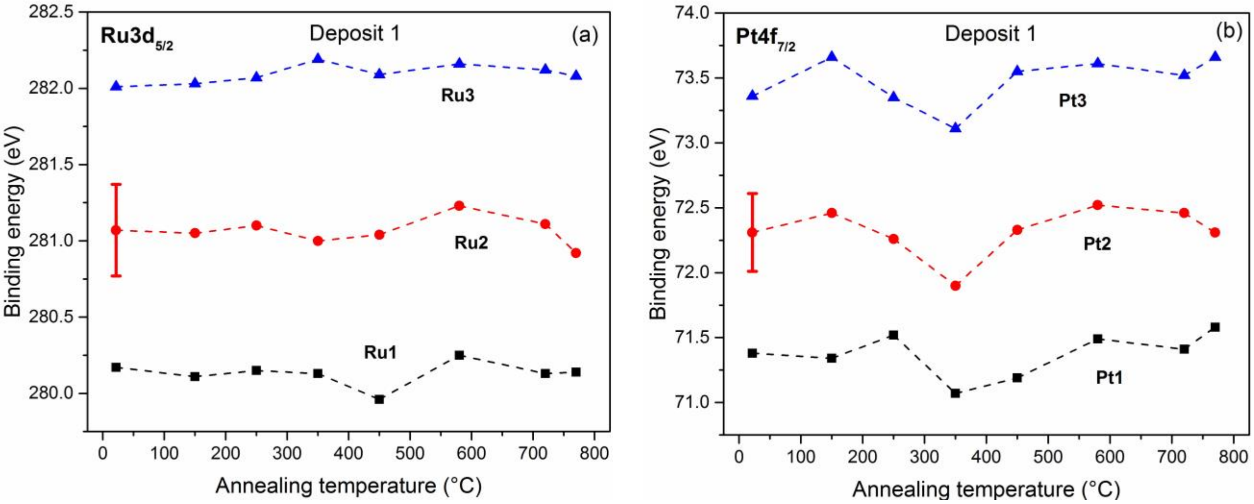

Figure 4.3: Evolution of the binding energies of (a) $Ru3d_{5/2}$ and (b) $Pt4f_{7/2}$ component peaks for deposit 1, as a function of annealing temperature.

Figure 4.4 shows the evolution of the Ru3d and Pt4f component fwhm values as a function of annealing temperature. The fwhm value of a peak is known to change when there is a change in order, and Fig. 4.4 shows abrupt changes over the range 250-350°C and also at 715°C. The changes in both binding energies (Fig. 4.3) and fwhm values (Fig. 4.4) suggest evolving interactions between Ru and Pt during annealing. This may also be seen in Fig. 4.5, which presents the temperature evolution of the Ru3d$_{5/2}$ and Pt4f$_{7/2}$ component fractions in deposit 1. The first components of both Ru and Pt (Ru1 and Pt1) decrease over the range 250-350°C and at 715°C, while Ru2 and Pt2 increase at the same temperatures. This suggests an intermixing due to interdiffusion. The evolution of component fractions on annealing is seen in inflections at those temperatures, and also in changes in the binding energies and fwhm values. These changes reflect compositional or structural changes.

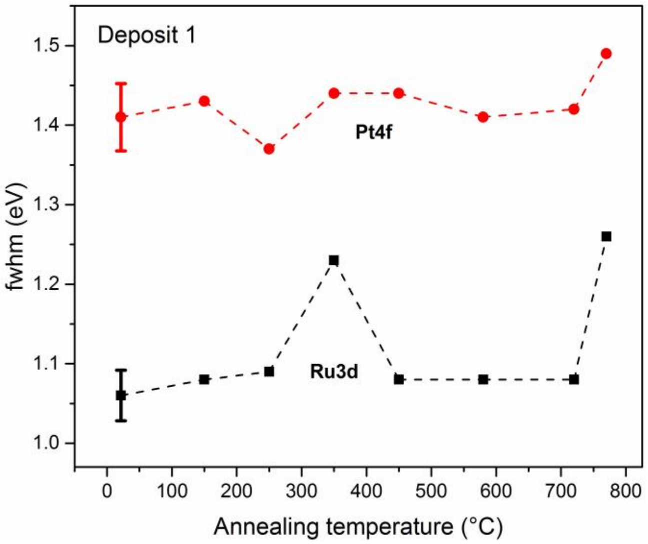

Figure 4.4: Evolution of Ru3d and Pt4f fwhm values for deposit 1, as a function of annealing temperature.

Comparing the binding energies of Ru1 and Pt1 with those of the pure metals [1, 124], we attribute Ru1 to Ru° in a Ru-rich environment, and Pt1 to surface Pt° in a Pt-rich environment. The changes in relative concentration undergone on annealing, seen in Fig. 4.5, suggest that metallic Ru and Pt tend to interact through diffusion. Because of this, Ru2 and Pt2, which increase as Ru1 and Pt1 decrease in the range 250-350°C, are attributed, respectively, to Ru in a Pt-rich environment, and Pt in a Ru-rich environment. Both Ru3 and Pt3 are minimally affected in this range.

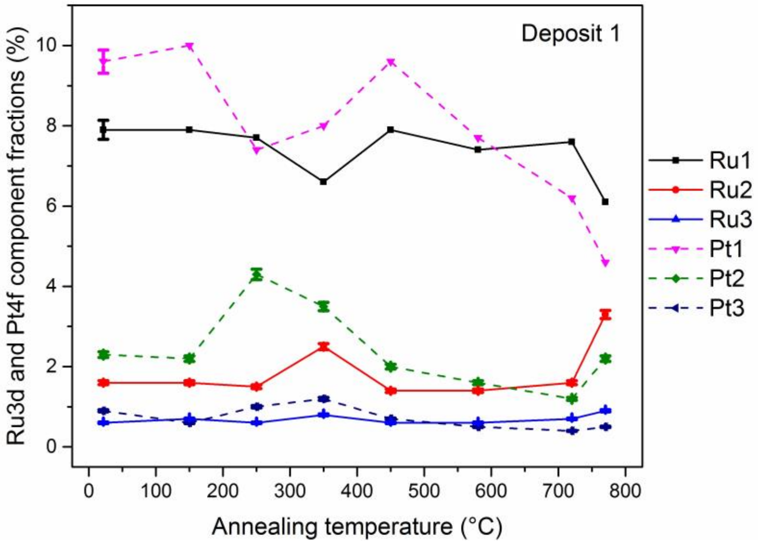

Figure 4.5: Evolution of the component fractions for Ru3d$_{5/2}$ and Pt4f$_{7/2}$ for deposit 1, as a function of annealing temperature. Ru1 is due to Ru° in a Ru-rich environment, and Pt1 is surface Pt° in a Pt-rich environment. Ru2 and Pt2 represent Ru in a Pt-rich environment and Pt in a Ru-rich environment, respectively. The attributions of Ru3 and Pt3 are discussed below.

The temperature evolution of various atomic concentrations, and the Pt:Ru atomic ratio of deposit 1, are presented in Fig. 4.6. The atomic percentage of C1s increases as a function of annealing temperature, indicating the deposition of residual hydrocarbons onto the NPs, as previously found [124]. The C1s spectrum indicates both hydrocarbons and carbide. Figure 4.7 shows the component fractions C1, which is the most intense carbon peak, and C6, the carbide. There are clear inflections at 350°C; the hydrocarbon increases, while the carbide decreases. They seem to be inversely related. As we know from previous studies [1, 124] on pure Pt and Ru, only Ru forms carbide. Therefore, the variations of carbide confirm the diffusion of Ru to the surface. As expected, the atomic percentages of the O1s components, in all the deposits, decrease on annealing, indicating the decomposition of the oxides at elevated temperatures. Further, on annealing, the atomic fraction of Ru increases, while the atomic fraction of Pt decreases. There is a temperature, in Fig. 4.6a, at which the atomic percentages of Ru3d and Pt4f intersect (~ 620°C), which is in agreement with the temperature, in Fig. 4.6b, where the ratio of Pt:Ru attains a value of 1. It appears that an interdiffusion occurs between these two metals, with Ru appearing at the surface; this supports the attributions of Ru2 and Pt2 as being due to interdiffusion.

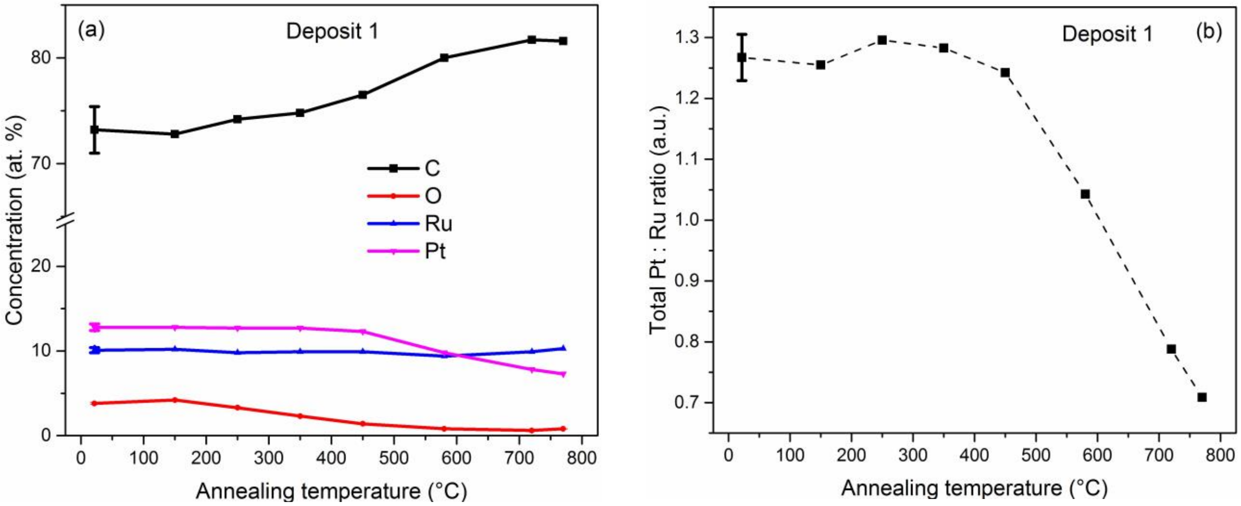

Figure 4.6: (a) Evolution of the atomic concentrations, where C refers to both hydrocarbons and carbide, and O, both metallic and organic carbon oxides, and (b) evolution of the total Pt:Ru atomic ratios.

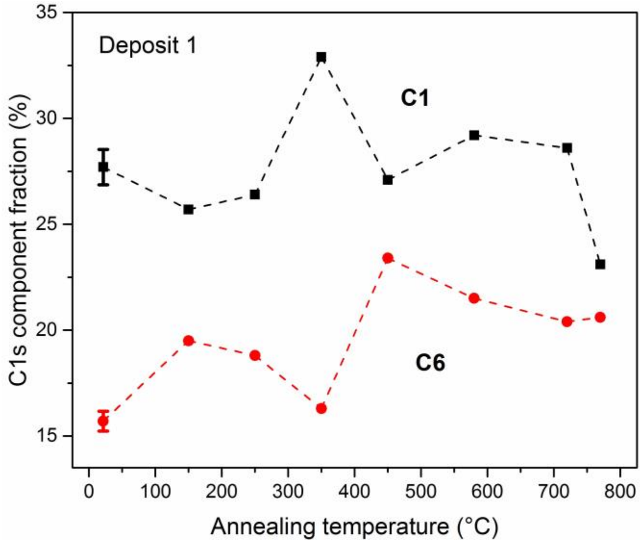

Figure 4.7: Evolution of the component fractions for C1 and C6 (carbide) for deposit 1, as a function of annealing temperature.

In summary, an XPS analysis of deposit 1 indicates that, at about 350°C, the metallic oxide begins to decompose, and intermixing between Ru and Pt occurs. In this deposit, at 350º and 715°C, changes in Pt and Ru environments are evident, as seen in Figs. 4.3-4.5, showing the interdiffusion of both metals. Increases of the atomic concentration of Ru (Fig. 4.6) and of carbide (Fig. 4.7), along with the decrease of the concentration of Pt (Fig. 4.6), indicate that Ru is the metal that diffuses and reaches the surface.

4.3.1.2 Deposits 2 and 3

For deposits 2 (the two metals were evaporated simultaneously), and 3 (Ru was evaporated on previously deposited Pt), the deconvolutions of C1s, Ru3d, and Pt4f were identical to those of deposit 1, although with different intensities; the C1s spectra, which overlap the Ru3d spectra, were separated into six peaks, and each component of the Ru3d and Pt4f spectral doublets was deconvoluted into three peaks. However, the O1s spectra, for deposits 2 and 3 were found to be composed of three components, as shown in Fig. 4.8 for deposit 2; the first two components, below a binding energy of 532.5 eV, are attributed to metal oxides, and the third, to oxidized carbon. However, the positions and the intensities of the O1s metal oxide components are different in deposits 2 and 3. Hence, their attributions are also different, as will be discussed below. As expected, these components disappear at elevated temperatures, as the oxides decompose.

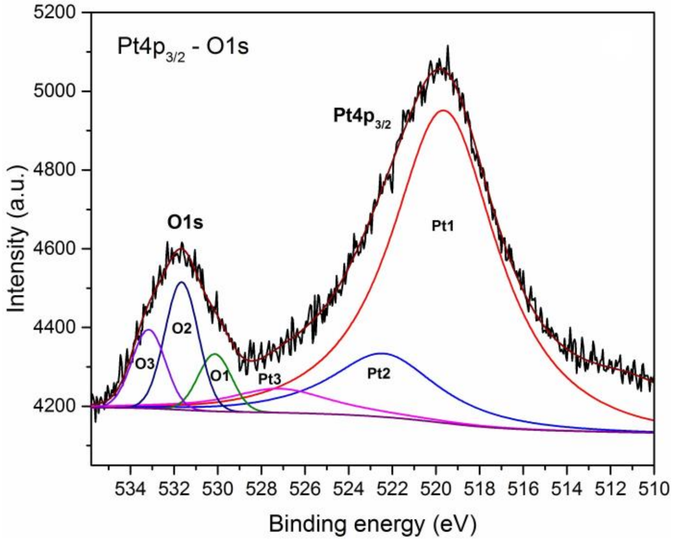

Figure 4.8 : Schematic deconvolutions of Pt4$p_{3/2}$-O1s for deposit 2.

Changes in the binding energies and fwhm values of the Ru and Pt components of deposits 2 and 3, as a function of annealing temperature, are not as evident as for deposit 1. The Ru3$d_{5/2}$ and Pt4$f_{7/2}$ binding energies and their fwhm values appear to be essentially independent of annealing temperature, for both deposits. Figure 4.9a presents the temperature evolution of the Ru3$d_{5/2}$ and

$Pt4f_{7/2}$ component fractions in deposit 2. The atomic ratios of the Ru components show variations at the previously noted 350°C, indicating the interaction of Ru with its environment as it rises to the NP surface. In comparison, the Ru and Pt components of deposit 3 are minimally affected. The attributions of all the components of deposits 2 and 3 are discussed below.

The temperature evolution of various atomic concentrations and the Pt:Ru atomic ratio of deposit 2, are presented in Figs. 4.9b and c. As for deposit 1, the atomic percentage of C1s (which represents both hydrocarbons and carbide) increases, and the atomic percentage of O1s decreases, as a function of annealing temperature; the trend of carbide in deposits 2 and 3, for which Ru is already at the surface, is different from that of deposit 1, as shown in Fig. 4.10: the carbide in deposit 2 remains almost constant, as a function of annealing temperature, while a decrease is observed for deposit 3, due to the increase of the hydrocarbon layer at the surface. In addition, the variations in atomic percentages of Ru and Pt, as well as the Pt:Ru atomic ratio, both shown for deposit 1 (Fig. 4.6) did not occur for deposit 2 (or deposit 3, whose trends of atomic concentrations and the Pt:Ru atomic ratio are identical to those of deposit 2). This suggests that both deposits 2 and 3 are more stable against diffusion.

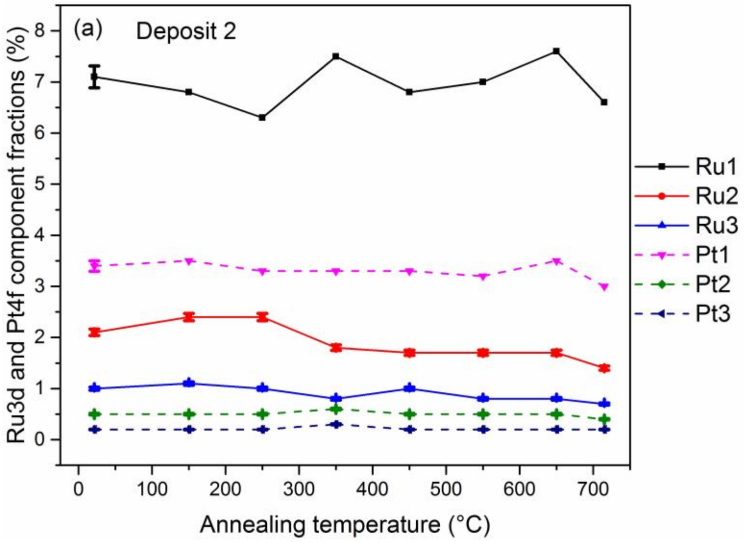

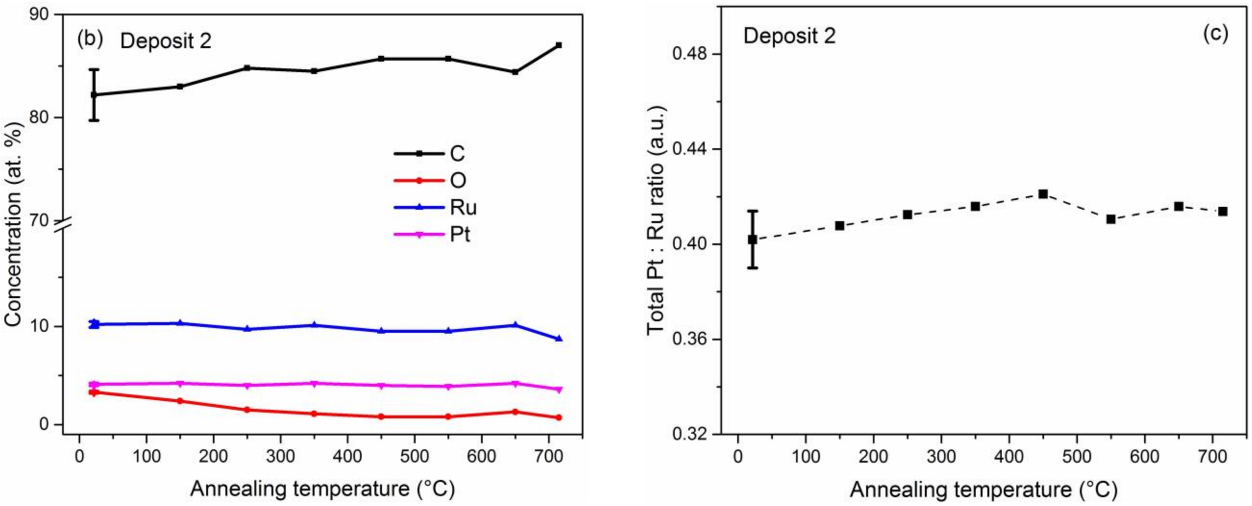

Figure 4.9: (a) Evolution of the component fractions for Ru3d$_{5/2}$ and Pt4f$_{7/2}$; Ru1 is due to Ru° in a Ru-rich environment, and Pt1 is surface Pt° in a Pt-rich environment, identical to deposit 1 and 3. Certain fractions of Ru2 and Pt2 represent Ru in a Pt-rich environment, and Pt in a Ru-rich environment, respectively. Attributions of the other fractions, along with the attributions of Ru3 and Pt3 are discussed later. (b) Evolution of the atomic concentrations for all elements, C refers to both hydrocarbons and carbide, and O represents both metallic and organic carbon oxides, and (c) evolution of the total Pt:Ru atomic ratios for deposit 2, as a function of annealing temperature.

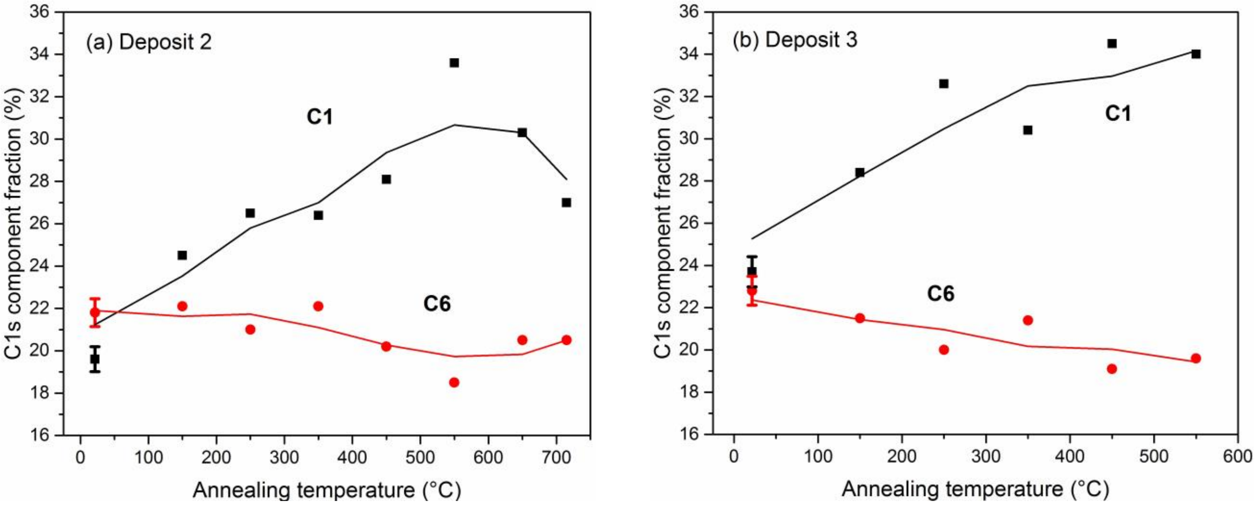

Figure 4.10: Evolution of the component fractions for C1 and C6 (carbide) for (a) deposit 2, (b) deposit 3, as a function of annealing temperature.

In summary, despite the fact that no significant diffusion of Ru and Pt is seen, either in deposit 2 or 3, the amounts of Ru and Pt at the surface are different for each deposit. We return to this subject in section 4.7.

For all three deposits, at about 350°C, interdiffusion occurs between Ru and Pt when oxide decomposes. In deposit 1, this interdiffusion is clearly seen because Ru, deposited below the Pt, comes to the surface. In deposit 2, some Ru exists at the surface, and in deposit 3, all the Ru is deposited on top of Pt. Thus, interdiffusion is significantly less in the latter two cases.

The component fraction trends for carbide on annealing, as well as the amount of carbide, are different for each deposit (Figs. 4.7 and 4.10). As discussed earlier, only Ru forms carbide. In deposits 2 and 3, there is, as expected, more carbide than in deposit 1, particularly at lower temperatures. Thus, carbide increases only in deposit 1 (Fig. 4.7), again confirming that Ru diffuses in preference to Pt, since this does not happen for Pt when it is deposited first, in deposit 3 (Fig. 4.10b) or when deposited simultaneously, in deposit 2 (Fig. 4.8a). It appears that the surface composition is different in each of the three deposits.

4.3.2 Valence Band Spectra

Based on previous studies [124, 125] of the valence bands of pure Ru and Pt deposited onto HOPG, in which both contain three peaks, we were able to separate the valence band spectra of all the deposits into six peaks; $Ru4d_{3/2}$, $Ru4d_{5/2}$, Ru5s, $Pt5d_{3/2}$, $Pt5d_{5/2}$, and Pt6s, at essentially the same binding energies found for the pure metals. All the binding energies, for the pure metals and the three deposits, are listed in Table 4.3. The spectral component intensities differed from those of the pure metals, and varied with the method of deposition and with annealing. Figure 4.11a shows the VB components of deposit 1, at room temperature, as an example.

The evolution of the PtRu NP VB spectrum on annealing had not previously been studied. Figure 4.11b presents this evolution for deposit 1. There is no obvious shift of component peak positions, as a function of annealing. This was also found for deposits 2 and 3. It appears that annealing has no discernable effect on the VB peak positions of all the deposits. It also may suggest that alloying has already started before annealing, so that no further variation occurs during annealing.

Table 4.3: Valence band peak components and their binding energies and fwhm values for pure Ru and Pt evaporated onto HOPG and deposits 1-3.

Element	**Label**	**Binding energy (eV)**	**FWHM (eV)**
VB of pure Ru	**Ru5s**	**0.8**	**1.3**
	$Ru4d_{5/2}$	**2.3**	**2.7**
	$Ru4d_{3/2}$	**5.0**	**2.7**
VB of pure Pt	**Pt6s**	**1.8**	**2.0**
	$Pt5d_{5/2}$	**4.4**	**3.7**
	$Pt5d_{3/2}$	**6.0**	**3.7**
VB of deposit 1	**Ru5s**	**0.5**	**0.9**
	$Ru4d_{5/2}$	**2.2**	**2.1**
	$Ru4d_{3/2}$	**4.8**	**2.1**
	Pt6s	**1.3**	**1.3**
	$Pt5d_{5/2}$	**3.4**	**3.1**
	$Pt5d_{3/2}$	**6.4**	**3.1**
VB of deposit 2	**Ru5s**	**0.5**	**1.0**
	$Ru4d_{5/2}$	**2.7**	**2.7**
	$Ru4d_{3/2}$	**5.4**	**2.7**
	Pt6s	**1.4**	**1.7**
	$Pt5d_{5/2}$	**4.0**	**2.6**
	$Pt5d_{3/2}$	**6.3**	**2.6**
VB of deposit 3	**Ru5s**	**0.5**	**1.3**
	$Ru4d_{5/2}$	**2.1**	**2.5**
	$Ru4d_{3/2}$	**4.8**	**2.5**
	Pt6s	**1.5**	**1.2**
	$Pt5d_{5/2}$	**3.2**	**2.5**
	$Pt5d_{3/2}$	**6.6**	**2.5**

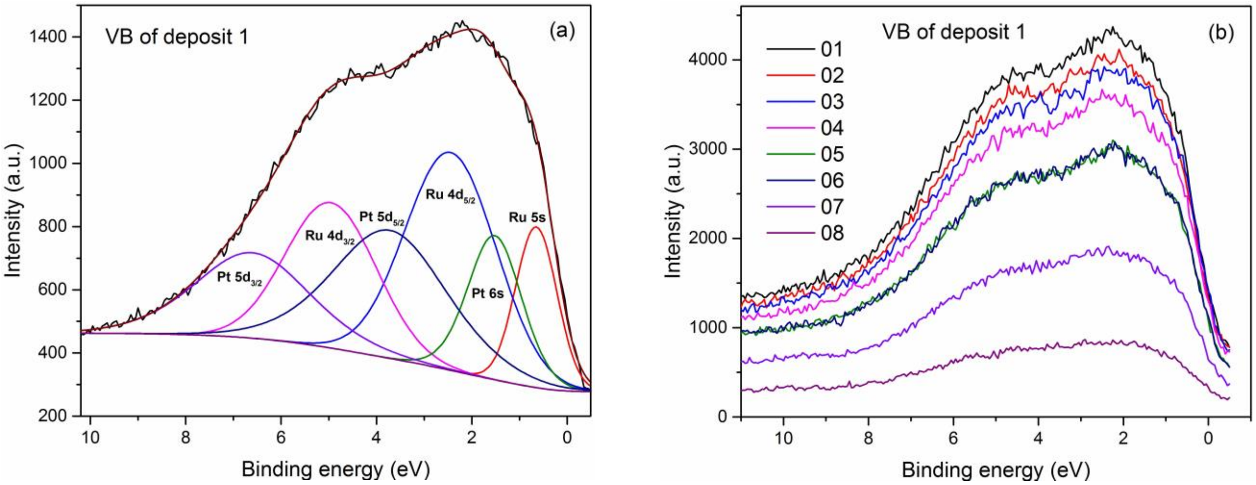

Figure 4.11: (a) Schematic separation of the valence band spectrum for deposit 1, at room temperature, (b) Evolution of the valence band spectra for deposit 1, as a function of annealing temperature; 1 to 8 represent the samples at room temperature, 150, 250, 350, 450, 580, 720, 770°C, respectively.

Figure 4.12 shows the evolutions of the Ru and Pt VB component fwhm values, for the three deposits, as a function of annealing temperature. The variation of the fwhm value of a peak indicates changes in crystalline order. In all the deposits, it is only the Pt5d fwhm that shows abrupt changes with temperature; this tells us that the Pt5d orbitals are greatly influenced in the alloying process, while the other orbitals appear to play some minor role. Despite the fact that the variation of Pt5d is clearly seen in all deposits, the reason for this variation is unknown.

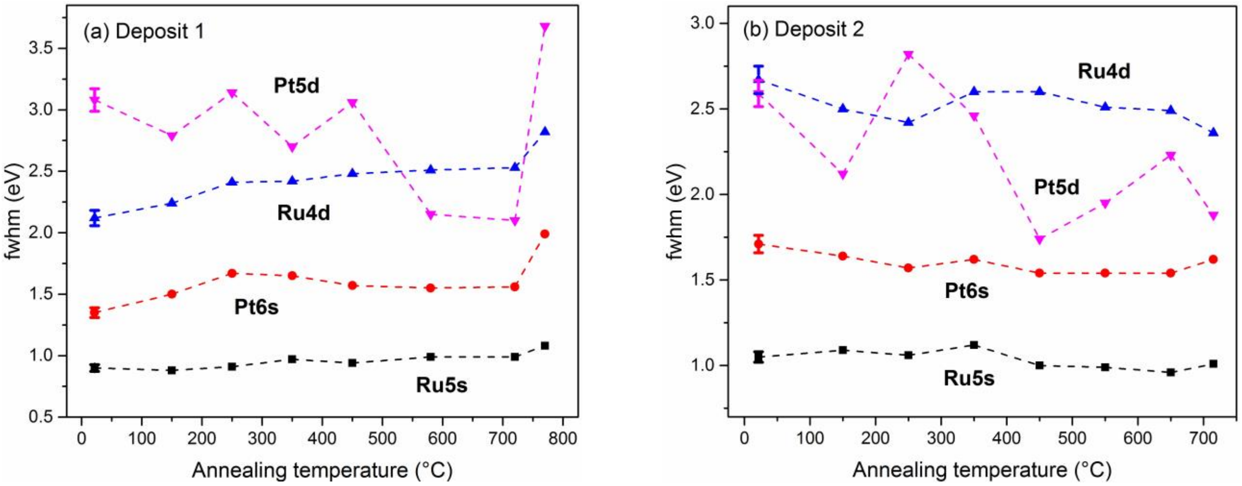

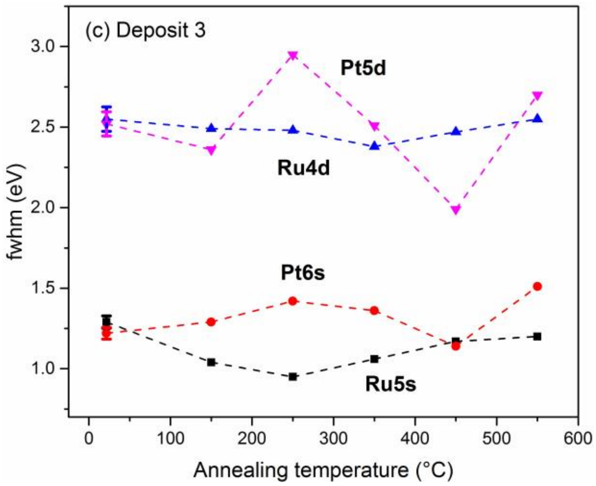

Figure 4.12: Evolution of fwhm of valence band components, (a) deposit 1, (b) deposit 2, and (c) deposit 3, as a function of annealing temperature.

Figure 4.13 compares the VB spectra of all the deposits, as well as those for pure Ru and Pt, both before and after annealing at about 715°C. The spectral shapes are all different, and their widths broaden with increasing annealing temperature. The changes in the spectra at elevated temperatures may be due to chemical reactions that take place at the surface. Such broadening results in the displacements of the d-band centers of all the three deposits to higher binding energies.

As seen in Fig. 4.13a, the shape of the spectrum of deposit 1, at room temperature, is similar to that of pure Pt because of the initial Pt coverage at the surface, although narrower than for pure Pt; at 715°C, the shape is similar to a combination of those of both pure Ru and Pt. It seems that when Pt predominantly covers the NP surface, the spectrum resembles that of Pt; when Ru covers the surface, as we will see for deposit 3, the spectrum resembles that of Ru; when both Ru and Pt are present at the surface, as we will see for deposit 2, the spectrum resembles a combination of both. That is, the VB spectrum may, indeed, reflect the outer surface. Hence, for deposit 1, it appears that, on annealing, Ru diffuses through Pt and moves to the surface; this is also seen in Fig. 4.6.

For deposit 2, the shapes of the spectra, before and after annealing, resemble a mixture of Ru and Pt, becoming broader for elevated temperatures. This surely indicates that both Ru and Pt exist at the surface.

For deposit 3, the shape of the spectrum changes from one that, at room temperature, is identical to pure Ru to one having a slightly different shape at elevated temperature, although still with a major Ru-like component, reflecting the interaction between Ru and diffusing Pt at the elevated temperatures; this will be confirmed in the discussion of our TOF-SIMS results. We conclude that the changes observed in Fig. 4.13 are consistent with the results of the core level XPS data.

The differences in shapes are accompanied by changes in the d-band centers of all the deposits. The d-band center is the energy that divides each VB band spectrum into two equal halves. Clearly, at both room temperature and at 715ºC, the d-band center of deposit 1 lies at the highest binding energy (the farthest from the Fermi level, and the most stable) and deposit 3 lies at the lowest binding energy. Given the similarities in VB spectral shapes discussed above, what we see may extend to the surface, despite the fact that the whole NP is being probed. If this is so, the shift of the d-band center to higher binding energies would be beneficial for use in catalysis. However, it is important to note that this shift is only one of several contributions to catalytic activity; another would be the chemical species present at the NP surface.

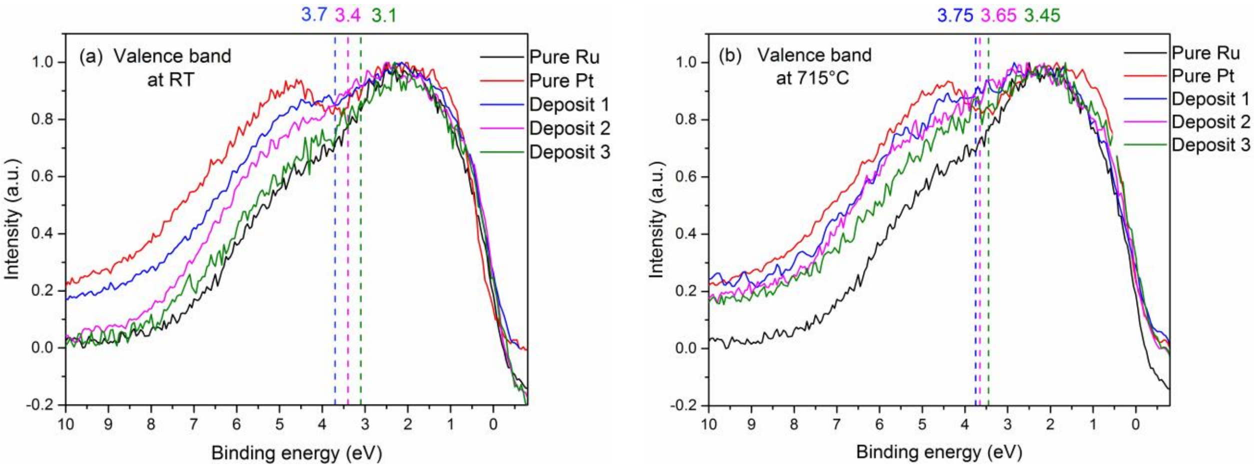

Figure 4.13: Comparison of the valence band spectra among pure Ru, pure Pt, each of them deposited separately onto HOPG, at room temperature and deposit 1, 2, and 3, at (a) room temperature and (b) after annealing at 715ºC.

4.4 TOF-SIMS Results and Discussion

In this analysis, we measure fragments sputtered from the NPs surface. This aids in our investigation of the surface chemical composition.

4.4.1 Deposit 1

4.4.1.1 Monometallic Fragments

Figure 4.14 depicts the presence of Ru^+ and Pt^- fragments as a function of annealing temperature. The y axis describes the *normalized* intensity (i.e., divided by the total ion intensity). The Ru^+ fragmental yield increased significantly at 600°C, indicating Ru diffusion through the Pt, coming to the surface. The Pt^- fragment intensity decreased as a function of annealing temperature, as was also found in our XPS data (Fig. 4.6). The low intensity Ru fragment peaks in the negative mode (i.e., the measurement of negative fragments), and of Pt fragments in the positive mode, follow the same trends.

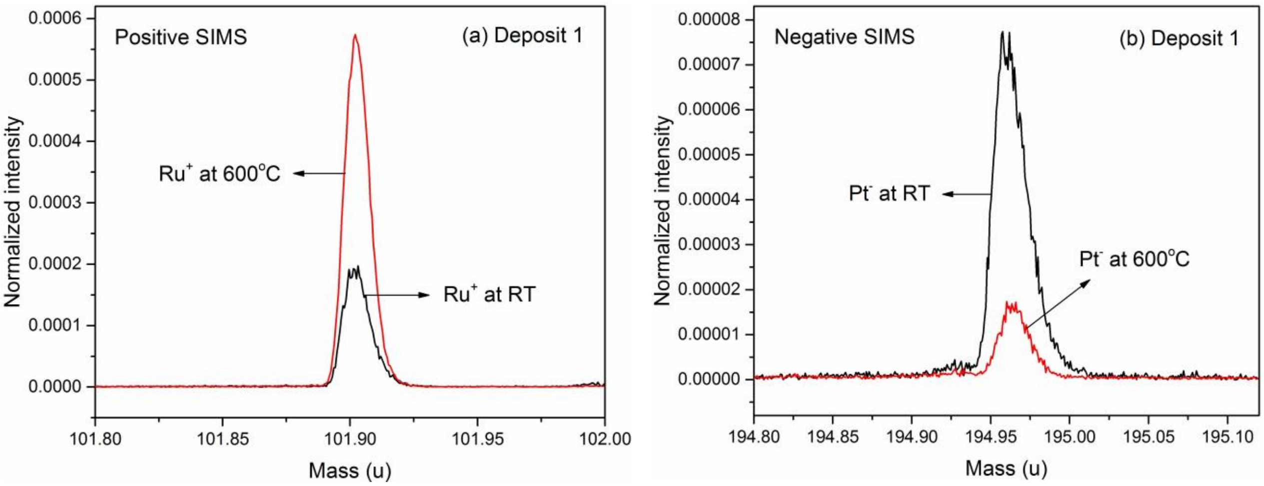

Figure 4.14: High resolution TOF-SIMS comparisons of (a) Ru^+ fragment, and (b) Pt^- fragment, for deposit 1, as a function of annealing, of PtRu NPs onto HOPG.

At 600°C, we found an increase in Ru_2^+ fragments and a decrease in Pt_2^- fragments, as seen in Fig. 4.15a and b, respectively. While we did not find any trace of Pt_3^- fragments, Ru_3^+ fragments (Fig. 4.15c) appeared at 600°C. Such increases in Ru_2^+ and Ru_3^+ at elevated temperatures tell us that Ru-Ru contact has increased, as more Ru diffuses to the surface. That is, annealing causes an increase in the surface concentration of Ru, to the extent that Ru atoms contact each other. Similarly, the decrease in Pt_2^- indicates that Pt is being diluted in the Ru surface environment. This confirms our XPS results, showing that Ru and Pt components at the surface vary as a function of annealing temperature. Thus, on annealing, the diffusion of Ru to the surface, and its enrichment (Ru_2^+ and Ru_3^+), indicate that the Ru1 XPS component contains contributions not only from the base Ru layer, but also from the Ru that has diffused to the surface.

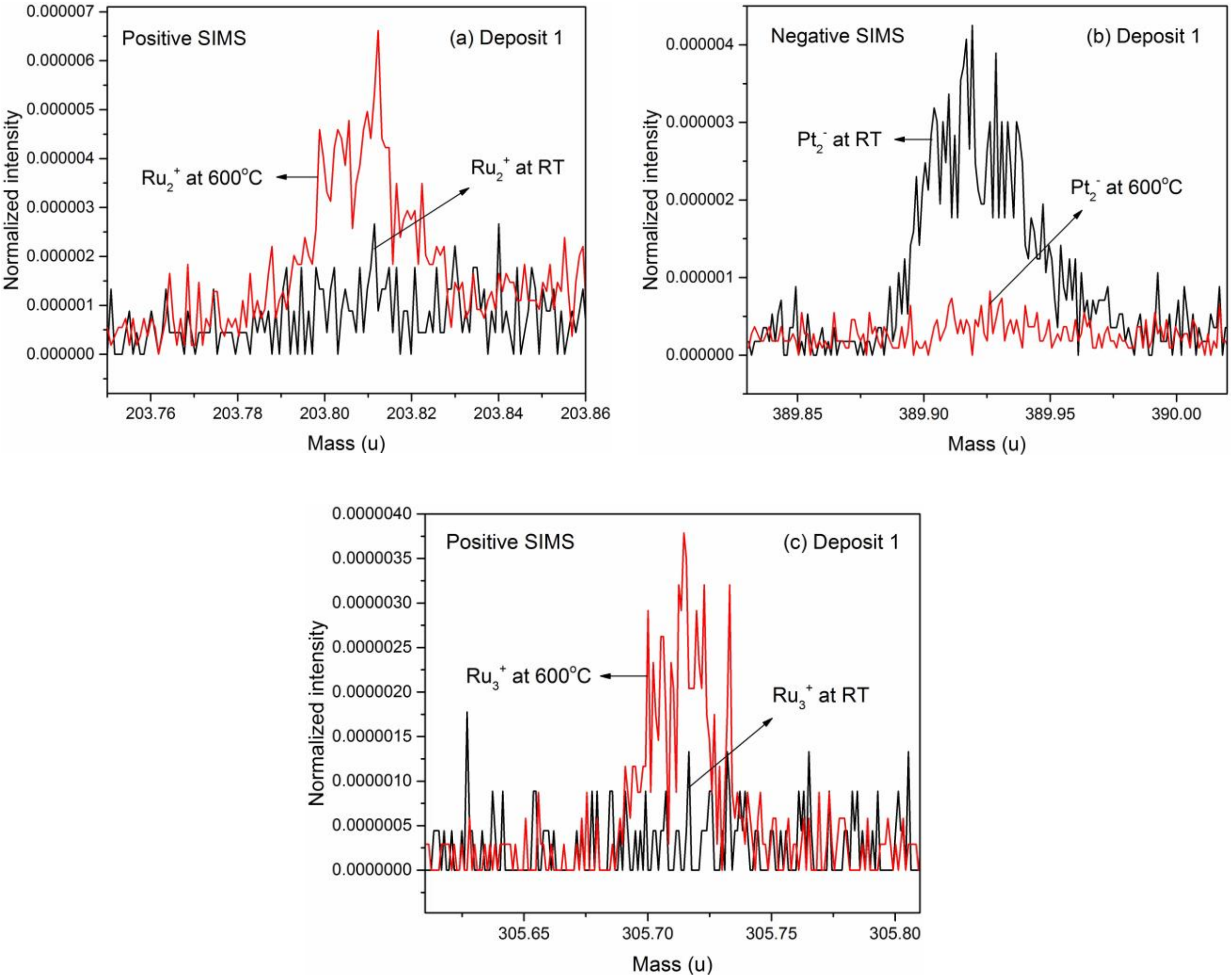

Figure 4.15: High resolution TOF-SIMS comparisons of (a) Ru_2^+ fragment, (b) Pt_2^- fragment, and (c) Ru_3^+ fragment, for deposit 1, as a function of annealing, of PtRu NPs onto HOPG.

4.4.1.2 Metal interaction with surface species

$Ru_xC_yH_z$, $Ru_xC_yO_z$, $Ru_xO_yH_z$, and $Ru_xC_yO_zH_w$ fragments, and similar Pt fragments, were found, indicating that the Ru has reached the surface and has reacted with the hydrocarbon layer deposited there. Hydroxyl and carboxyl group fragments were also identified, as correspondingly found in the C1s and O1s XPS spectra.

Figure 4.16 shows oxygen, carbon, and hydrocarbons fragments for Ru (positive mode), and Figure 4.17, those for Pt (negative mode). The two most abundant isotopes of Ru and Pt were used in attributing each of the fragments in these figures, in order to confirm their presence. Again, similar fragments were found for opposite modes, but at much lower intensities.

Both Ru carbon and hydrocarbon fragments increased as a function of annealing temperature, similar to the Ru fragment trends in Fig. 4.14a. Corresponding Pt carbon and hydrocarbon fragments decreased at elevated temperature, following the same trend as Fig. 4.14b.

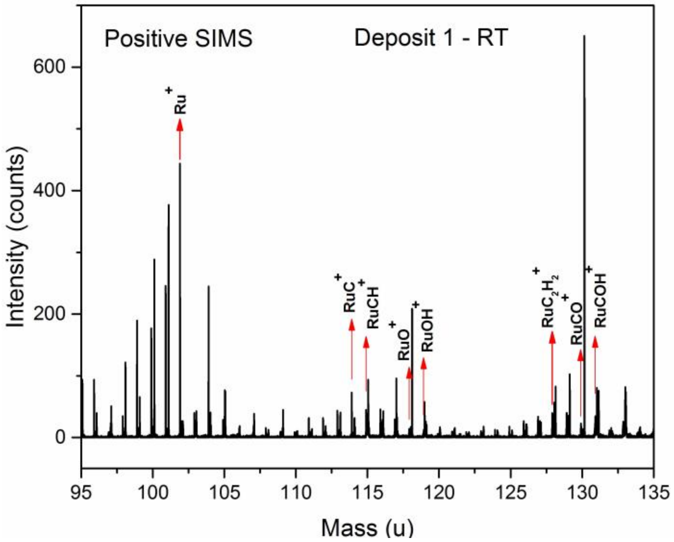

Figure 4.16: Positive SIMS spectra of Ru related fragments at room temperature of deposit 1.

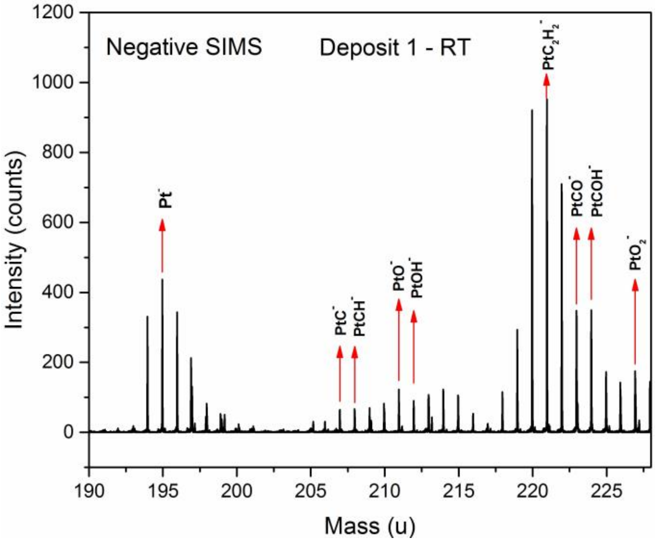

Figure 4.17: Negative SIMS spectra of Pt related fragments at room temperature of deposit 1.

Figure 4.18 shows RuO^+ and PtO^-. RuO^+ remains constant on annealing. XPS O1s spectra of these two samples (Fig. 4.2) show that metallic oxide has decomposed at or below 600°C. Recalling that Ru comes to the surface at elevated temperatures (Fig. 4.14a), and that some of it reacts with residual oxygen, this may simply reflect a steady state between Ru diffusion to the surface and RuO^+ decomposition.

Possible PtO^- fragments were found only in the negative mode, and decreased as a function of annealing temperature. However, because two other fragments, $^{194}PtOH^-$ and $^{196}PtCH_3^-$, have the same mass, we are not able to analyze this fragment in detail. In addition, we found PtO_2^- fragments, as seen in Fig. 4.18b, which decrease substantially as a function of annealing temperature. This decrease indicates that the Pt surface concentration is decreasing. Moreover, metallic oxides decompose at elevated temperatures, with some of the released oxygen then possibly oxidizing the hydrocarbon layer. One recalls that the XPS spectra show that the carbonyl groups increase as a function of annealing temperature (an increase in the amount of organic oxidation product), as seen in Fig. 4.2b. This occurs with the other two deposits, as well.

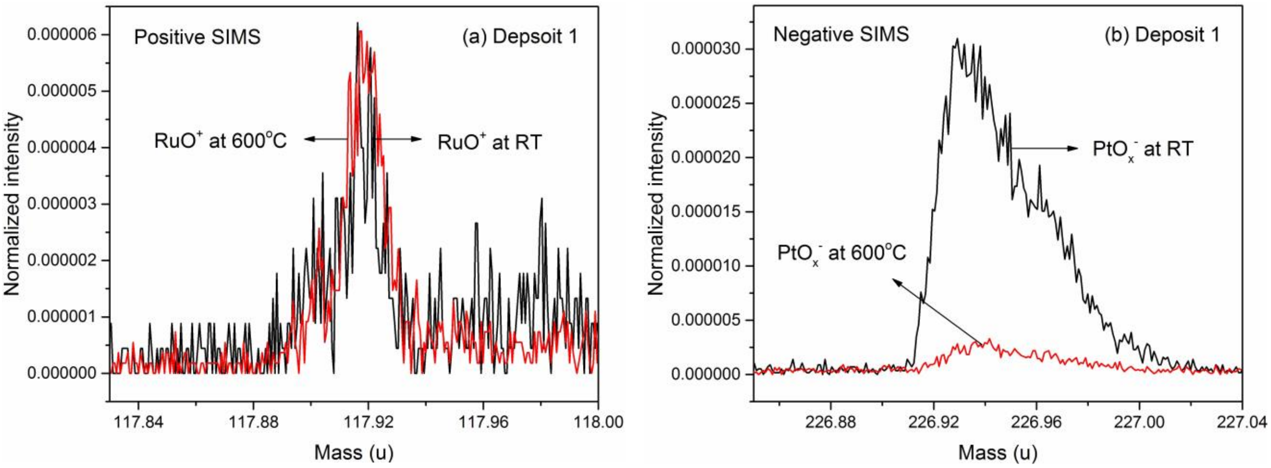

Figure 4.18: High resolution SIMS comparisons of (a) RuO^+ fragment, and (b) $PtOx^-$ fragment, for deposit 1, as a function of annealing, of PtRu NPs onto HOPG.

4.4.1.3 PtRu fragments

PtRu alloy fragments appear only in the positive mode, and at very low intensity. This is taken to be related to the preferential stabilities of Ru^+ and Pt^- fragments, suggesting that PtRu fragments exist largely as dipoles ($Ru^{\delta+}$-$Pt^{\delta-}$), not observable in either mode. Figure 4.19 shows such fragments. They remain constant as a function of annealing temperature. This constancy is due to the very small signal of PtRu fragments, which makes it impossible to track any changes for PtRu fragment formation, on annealing. The other peak in Fig. 4.19 is attributed to an unidentified contaminant.

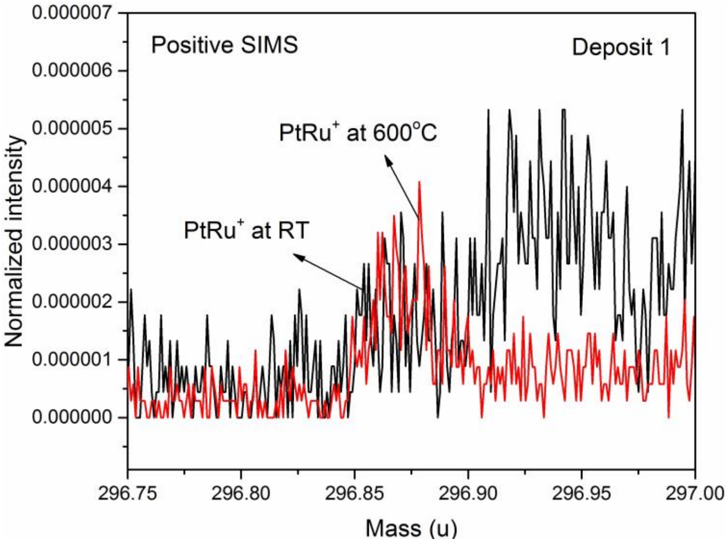

Figure 4.19: High resolution positive SIMS comparisons of PtRu$^+$ fragment for deposit 1, as a function of annealing, of PtRu NPs onto HOPG.

The TOF-SIMS results confirm our XPS data, as related to the increase of Ru fragments (Ru$^+$, Ru$_2^+$, and Ru$_3^+$) and the related decrease of Pt fragments (Pt$^-$ and Pt$_2^-$), at the surface on annealing, indicating the diffusion of Ru through Pt, reaching the surface. Our analysis also shows the decomposition of oxide on annealing, as found in XPS data.

4.4.2 Deposit 2

4.4.2.1 Pt and Ru fragments

Figure 4.20 shows Ru$^+$ and Pt$^-$ fragments as a function of annealing temperature. The TOF-SIMS results for deposit 2 are different from those of deposit 1; Ru$^+$ fragments for deposit 2 show a slight decrease, while Pt$^-$ fragments show a slight increase, as a function of annealing temperature. It appears that the increase of hydrocarbons, and carbide formation at elevated temperatures, are more significant than the diffusion of Ru to the surface, where it already exists for this deposit. The increase of one the most intense hydrocarbons, C$_2$H$^-$, is presented in Fig.

4.21. This hydrocarbon was also the most significant in the other two deposits, where it also underwent the same increase, as a function of annealing temperature. The slight increase of Pt on annealing indicates the minor diffusion of Pt to the surface.

Given that TOF-SIMS is more surface sensitive than XPS, these slight changes are not evident in XPS, as can be found in Fig. 4.9b and c. Clearly, different preparation methods give PtRu NPs having different structures and compositions, especially at the surface, and differences are maintained on annealing.

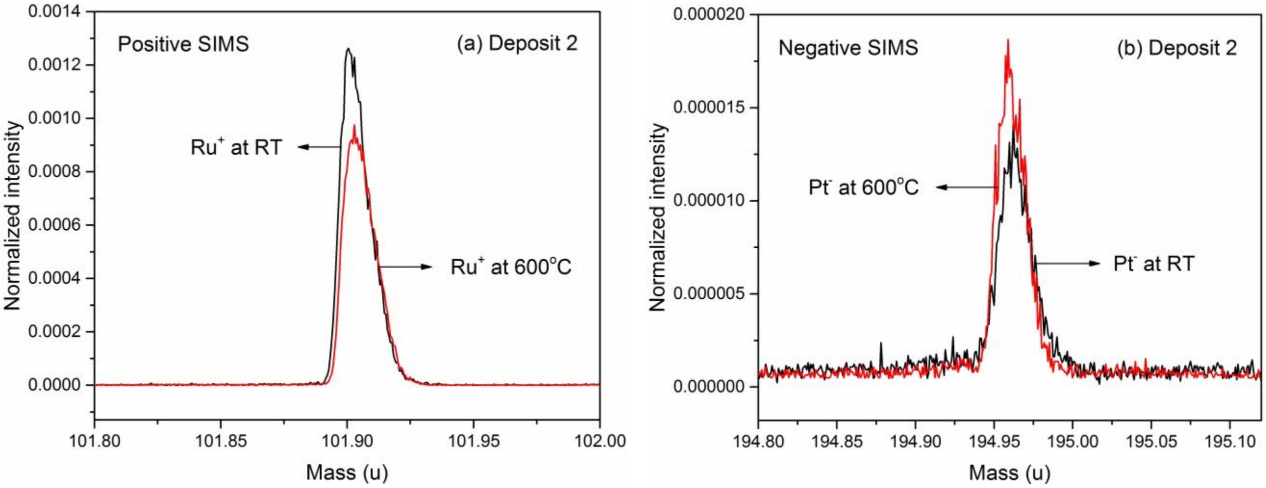

Figure 4.20: High resolution SIMS comparisons of (a) Ru^+ fragment, and (b) Pt^- fragment, for deposit 2, as a function of annealing, of PtRu NPs onto HOPG.

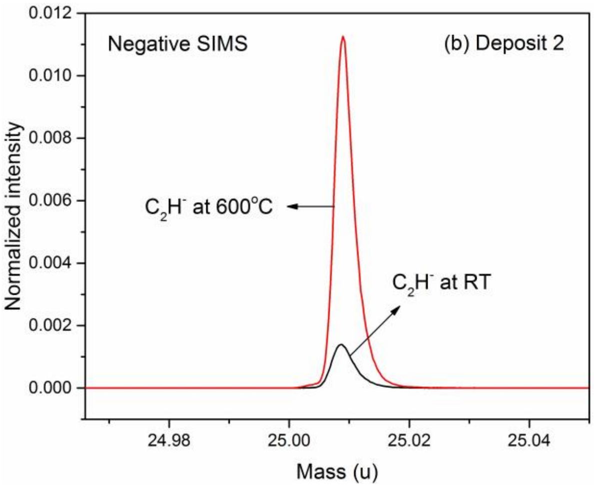

Figure 4.21: High resolution SIMS comparisons of C2H$^-$ fragment, for deposit 2, as a function of annealing, of PtRu NPs onto HOPG.

As for deposit 1, Ru_2^+, Ru_3^+ and Pt_2^- fragments are found for deposit 2. Ru_2^+ exhibits the same trend as does Ru^+ in this deposit, as shown in Fig. 4.22, for the same reason. Pt_2^- shows a very slight decrease as a function of annealing temperature. The minute amount of Ru_3^+ fragments increases on annealing. The signals and also the changes in Pt_2^- and Ru_3^+ intensities are so miniscule that we feel it is better not to offer any interpretation.

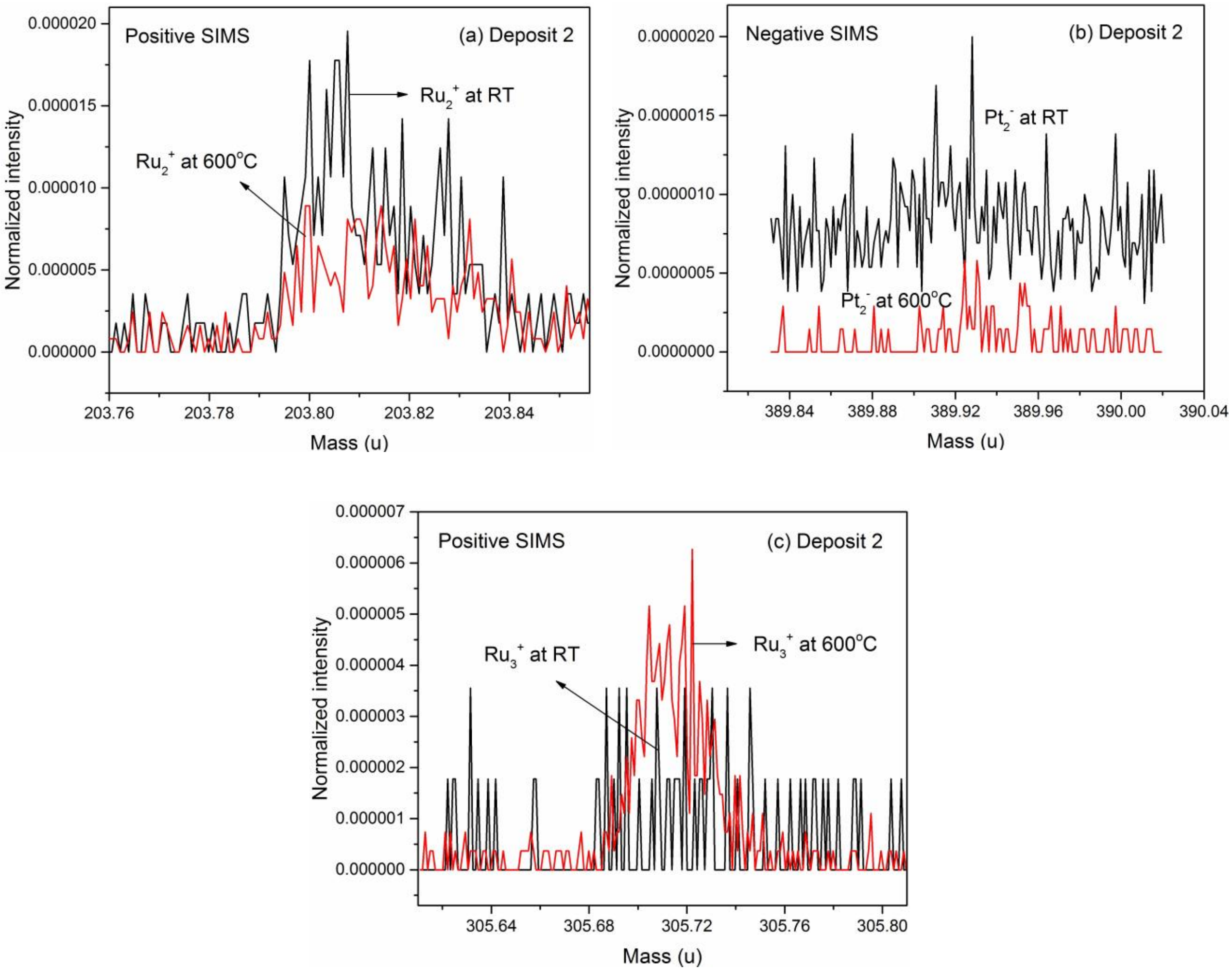

Figure 4.22: High resolution SIMS comparisons of (a) Ru_2^+ fragment, (b) Pt_2^- fragment, and (c) Ru_3^+ fragment, for deposit 2, as a function of annealing, of PtRu NPs onto HOPG.

4.4.2.2 Pt and Ru interaction with surface species

As with deposit 1, $Ru_xC_yH_z$, $Ru_xC_yO_z$, $Ru_xO_yH_z$, and $Ru_xC_yO_zH_w$ fragments, as well as similar Pt fragments, were found, although at different intensities. These fragments again indicate the presence of both metals at the nanoparticle surface.

Figure 4.23 shows RuO^+ and a very minuscule amount of PtO^-. Unlike deposit 1, the decrease of RuO^+ is clearly seen, due to the decomposition of metallic oxide, as well as a much reduced diffusion of Ru to the surface. PtO^- decreased at elevated temperatures, although much less significantly than for deposit 1. However, it should be noted that the presence of some RuO^+ and PtO^- at 600°C, in the TOF-SIMS analysis of all the three deposits, may be related to residual oxygen in the chamber.

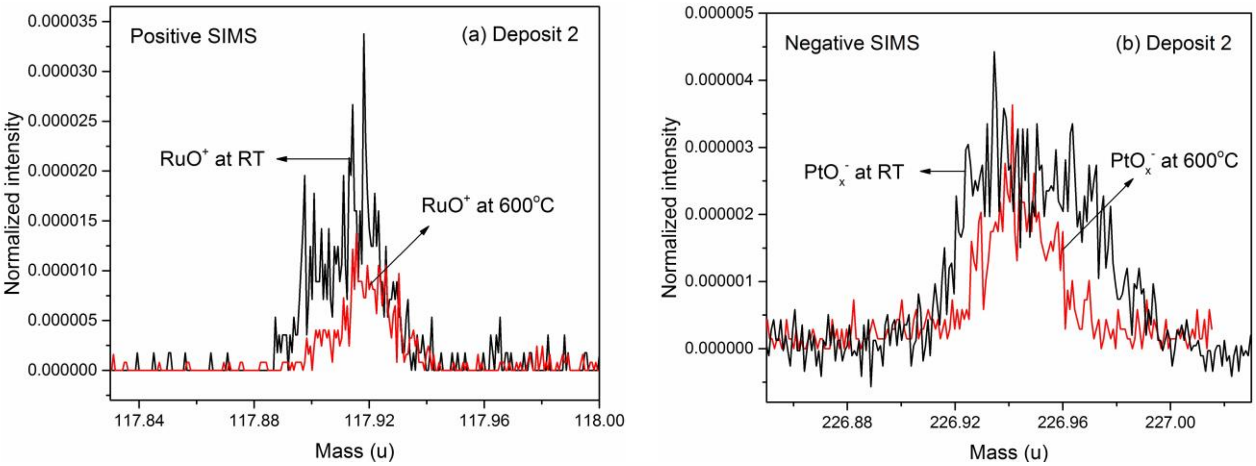

Figure 4.23: High resolution SIMS comparisons of (a) RuO^+ fragment, and (b) PtO_x^- fragment, for deposit 2, as a function of annealing, of PtRu NPs onto HOPG.

4.4.2.3 PtRu fragments

As with deposit 1, PtRu alloy fragments exist only in the positive mode. These fragments are marginally more evident at 600°C, as seen in Fig. 4.24.

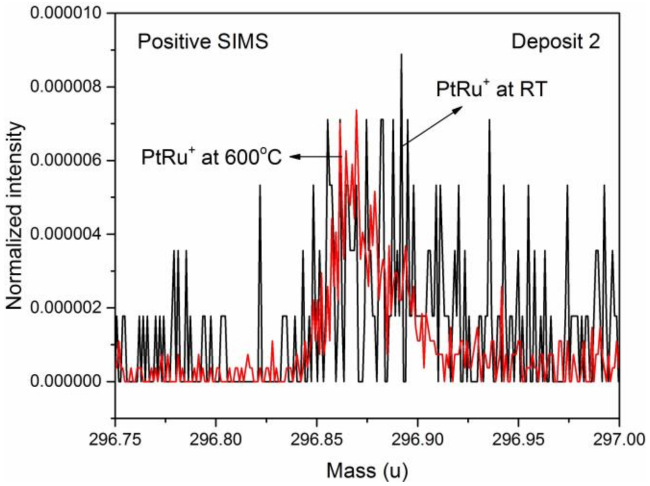

Figure 4.24: High resolution positive SIMS comparisons of $PtRu^+$ fragment for deposit 2, as a function of annealing, of PtRu NPs onto HOPG.

In this deposit, TOF-SIMS revealed an important point: the minor diffusion of Pt to the surface, which was not evident in our XPS data. We also found that, as with deposit 1, oxide decomposed upon annealing, both Ru- and Pt-hydrocarbon fragments were present, as were PtRu fragments.

4.4.3 Deposit 3

4.4.3.1 Pt and Ru fragments

Figure 4.25 shows Ru^+ and Pt^- fragments as a function of annealing temperature. For this deposit, Pt fragments have quite low intensities, when compared to deposits 1 and 2, since the rate of Pt diffusion to the surface is much less than that of Ru.

Ru^+ fragments undergo a more considerable decrease, as a function of annealing temperature, than in deposit 2. Because the entire Ru deposit, already at the surface, remains there, no more diffusion of Ru to the surface occurs. Thus, this *relative* decrease of Ru^+ fragments appears to be due to the increase of surface hydrocarbon and carbide. Both Ru_2^+ and Ru_3^+ fragments decrease on annealing, for the same reason (Fig. 4.26a and c).

Pt^- fragments show a slight *relative* decrease, as a function of annealing temperature, also due to the increase of surface hydrocarbons. Ultimately, the relative concentration of Pt_2^- fragments becomes almost undetectable.

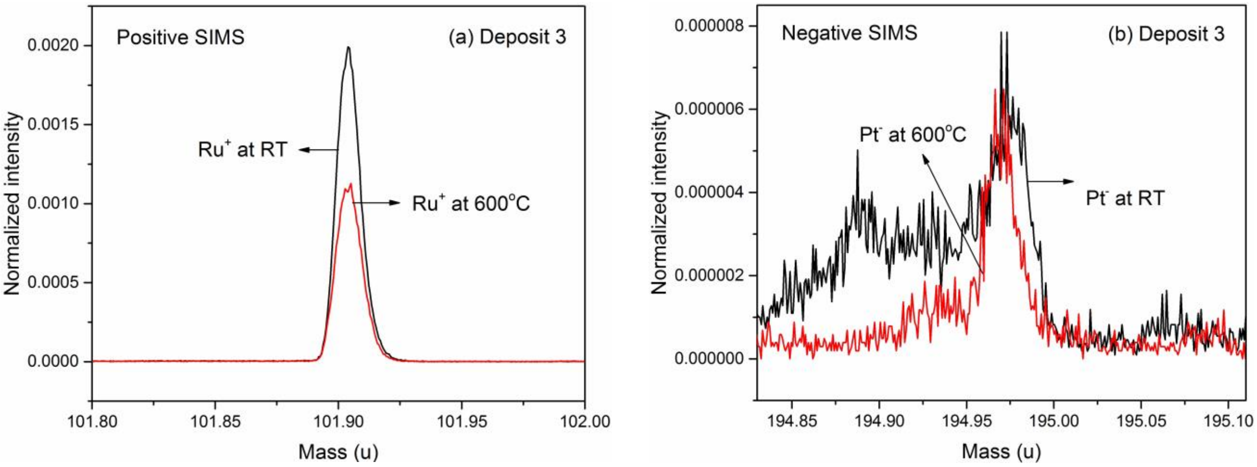

Figure 4.25: High resolution SIMS comparisons of (a) Ru$^+$ fragment, and (b) Pt$^-$ fragment, for deposit 3, as a function of annealing, of PtRu NPs onto HOPG.

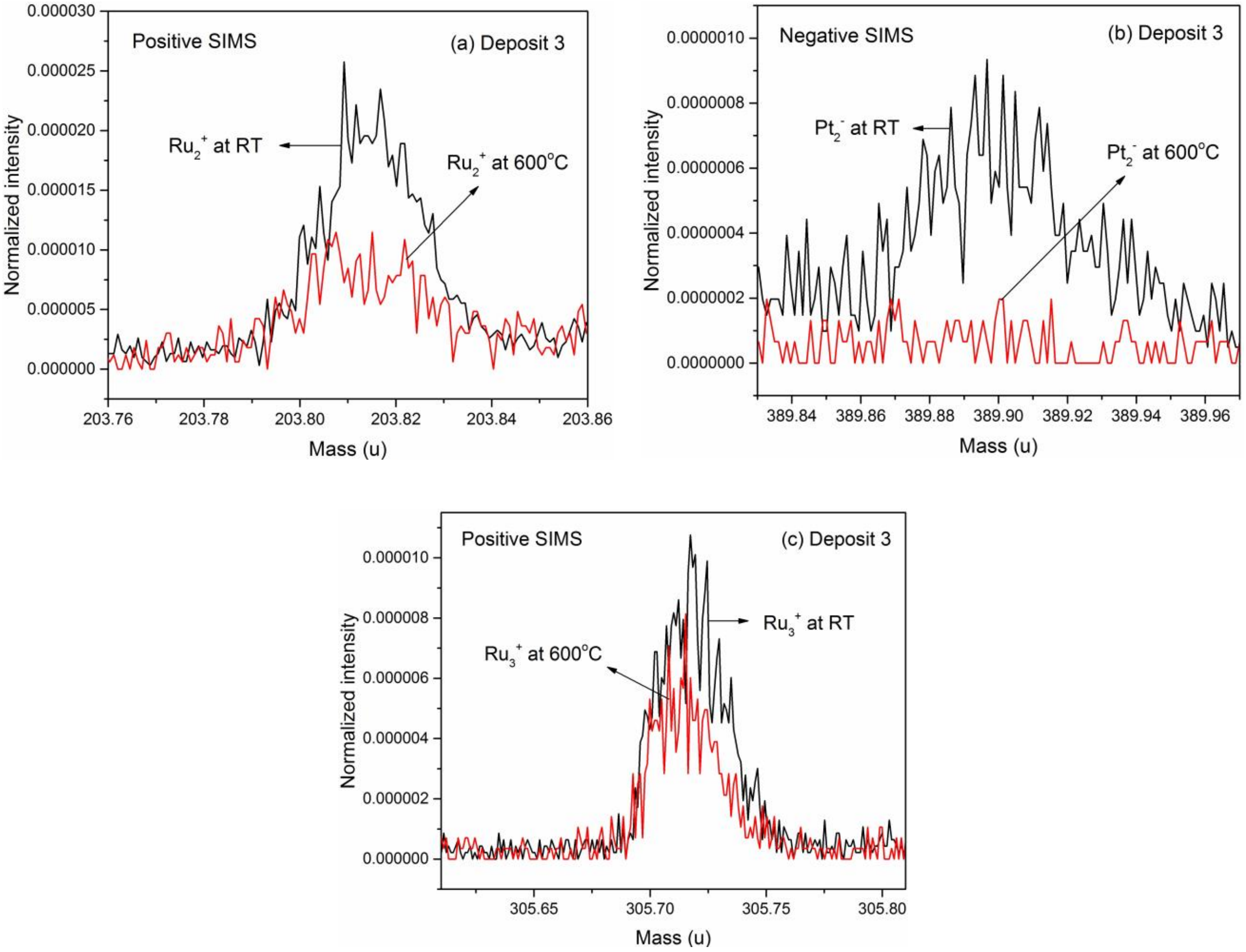

Figure 4.26: High resolution SIMS comparisons of (a) Ru_2^+ fragment, (b) Pt_2^- fragment, and (c) Ru_3^+ fragment, for deposit 3, as a function of annealing, of PtRu NPs onto HOPG.

4.4.3.2 Pt and Ru interaction with surface species

As with deposits 1 and 2, both Pt- and Ru-hydrocarbon fragments were found, the former at much lower intensities. These fragments again indicate the presence of both metals at the nanoparticle surface, once more confirming the minor diffusion of Pt to the surface.

For RuO^+ (Fig. 4.27a), changes on annealing are more discernible than for deposit 2. Because the decrease of RuO^+ is due to its decomposition at elevated temperatures, the Ru concentration at the surface does not change (no Ru diffusion). Similar to deposit 2, PtO^- decreases slightly at elevated temperatures.

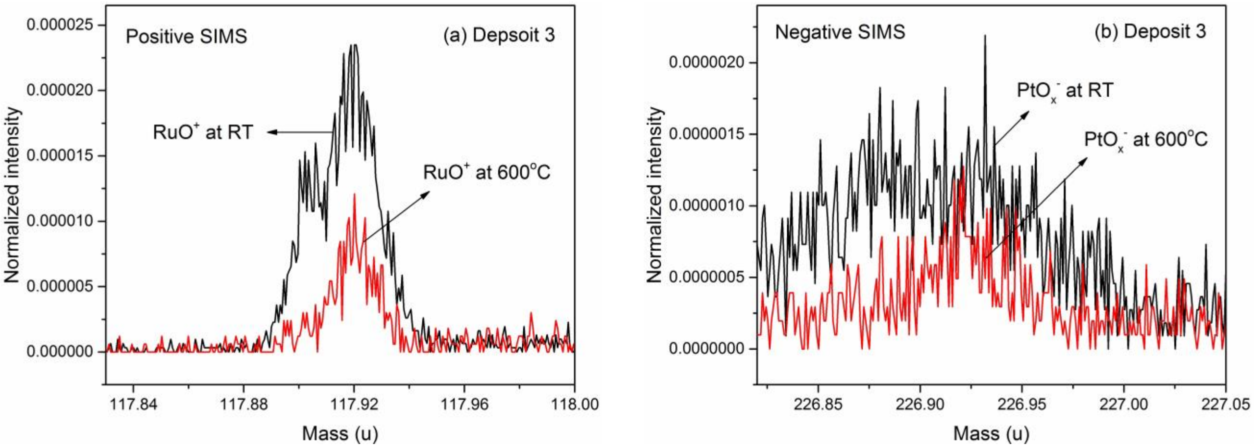

Figure 4.27: High resolution SIMS comparisons of (a) RuO^+ fragment, and (b) PtO_x^- fragment, for deposit 3, as a function of annealing, of PtRu NPs onto HOPG.

4.4.3.3 PtRu fragments

As with deposits 1 and 2, the low intensity PtRu alloy fragments exist only in the positive mode. These fragments possibly remain constant as a function of annealing temperature, as seen in Fig. 4.28, which is for the same reason given for deposit 1: the very small signal of PtRu fragments, for which changes could not be followed. Hence, PtRu alloy formation cannot be analyzed in detail.

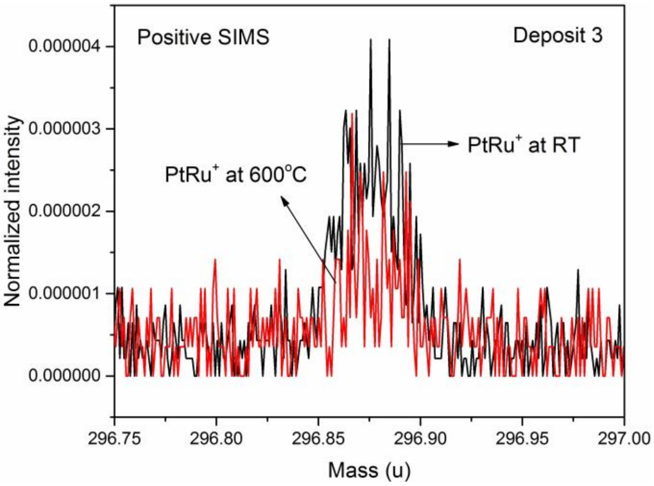

Figure 4.28: High resolution positive SIMS comparisons of $PtRu^+$ fragment for deposit 3, as a function of annealing, of PtRu NPs onto HOPG.

In this deposit, the surface is mostly covered by Ru; only a small amount of Pt is detected at the surface. As with deposits 1 and 2, Ru- and Pt-hydrocarbons and PtRu fragments were detected in this deposit. We also found oxide decomposition on annealing. RuO^+ has the most obvious decrease in this deposit, rather than the other two, because the total amount Ru is already present at the surface. On the other hand, PtO^- has the most obvious decrease in deposit 1, because, in addition to oxide decomposition, Pt is diluted at the surface by the arrival of additional Ru.

In summary, TOF-SIMS confirms and augments what we found from our XPS data; this includes the major diffusion of Ru through Pt and the minor diffusion of Pt through Ru; the presence of metal oxide and hydrocarbon fragments, indicating that, even under ultra-high vacuum, the nanoparticles reacted with residual C- and O-containing gases to form surface contaminants; oxide decomposition and to increase hydrocarbon deposition on annealing. Further, TOF-SIMS delineated changes that occur in each deposit. These include the formation of Ru_n^+ and Pt_n^-; the existence of both $Pt_xC_yH_z$ and $Ru_xC_yH_z$ fragments, demonstrating the presence of both metals at the nanoparticle surface, no matter which metal was deposited first; the presence of PtRu fragments, indicating alloy formation, even at room temperature. Moreover, it was only by using TOF-SIMS that we could study RuO^+ and PtO^- separately because, in the case of XPS, the positions of Ru and Pt oxides are so close in binding energy that they cannot be readily distinguished.

The presence of both Ru and Pt at the outer surfaces of all the depositions was confirmed by our XPS and TOF-SIMS results. A comparison of the relative concentrations of the Ru and Pt fragments at the surface, among the three deposits, obtained from XPS analyses (impossible with TOF-SIMS), is presented in section 4.8.

4.5 HAADF/STEM and EELS Results and Discussion

To study the morphology of the NPs, as well as to determine the crystal structures of the NPs, we turn to HAADF-STEM photomicrographs and EELS maps.

4.5.1 Deposit 1

Figure 4.29 shows STEM photomicrographs of the as-deposited NPs, and those annealed at 650°C for 1 h. There are distinct patches containing predominantly Ru or Pt (as visible from the brighter intensity patches in the HAADF images and from EELS images, confirmed later in Fig. 4.30), forming a clearly resolved lattice of Pt adjacent to a more defective Ru-rich lattice. This is in agreement with Kawasaki et al. [126], who reported disorder in the Ru lattice. We also observe many single atoms and small clusters with defective lattices (some not fully crystalline), which appear to be Ru-rich (identified with dashed arrows in Fig. 4.29a), based on the intensity of the features, as compared to Pt-rich areas of the same size (identified with full arrows in Fig. 4.29a).

After annealing (Fig. 4.29b), we see a more perfect lattice with several interconnected particles (sintering of the particles has occurred). From these images, there are regions that are Pt-rich (identified with full arrows), and others that are Ru-rich (identified again with dashed arrows), but no clear uniform Pt shell covering the Ru-rich areas. This is different from what was reported in our PtFe NP study [125], and also by some theoreticians [4, 46, 50] in their PtRu NP studies. These theoreticians claimed that Pt forms a shell at the surface, covering the Ru core. From Fourier filtering of our images, and from simple inspection, one can directly visualize that, in some regions, the lattice orientation extends to adjacent particles with little change of the spacing of the crystallographic planes detected (the atomic radii of Ru and Pt differ by only 3 %) from regions where there are clearly distinct Pt- and Ru-rich areas. There are also regions, however, where the lattice orientation changes and there appears to be a more defective lattice in the Ru-rich, than in the Pt-rich, areas. These results suggest that there may already be a single strained lattice, with a composition varying between Ru and Pt, having some areas of the same lattice rich in Ru, and others rich in Pt.

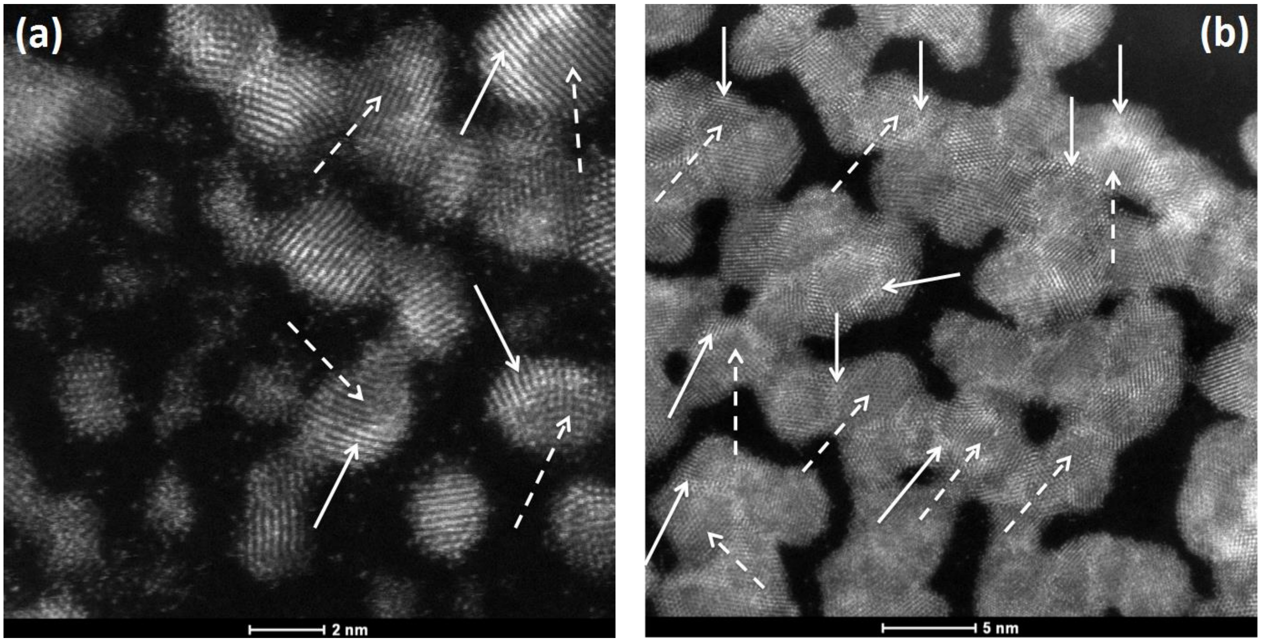

Figure 4.29: STEM images of PtRu NPs onto HOPG at (a) room temperature, (b) 650°C, in deposit 1. Dashed arrows point to Ru-rich areas, full arrows point to Pt-rich areas.

The EELS maps (Fig. 4.30a) show that, upon deposition, the Pt is segregated at the surface. This is shown from the Pt distribution (shown in green on the color-coded map) which essentially appears on the edges of the clusters. This clearly shows that the Pt is at the surface of the particles, due to its deposition after Ru. Pt practically forms a layer around Ru particles. After annealing, Fig. 4.30b shows phase separation. This map again shows two phases, with some Pt in Ru-rich areas, and some Ru in Pt-rich areas. In this case, the Pt distribution does not entirely surround the Ru-rich areas. Therefore, Ru extends to the surface of the NPs. This is consistent with the XPS measurements.

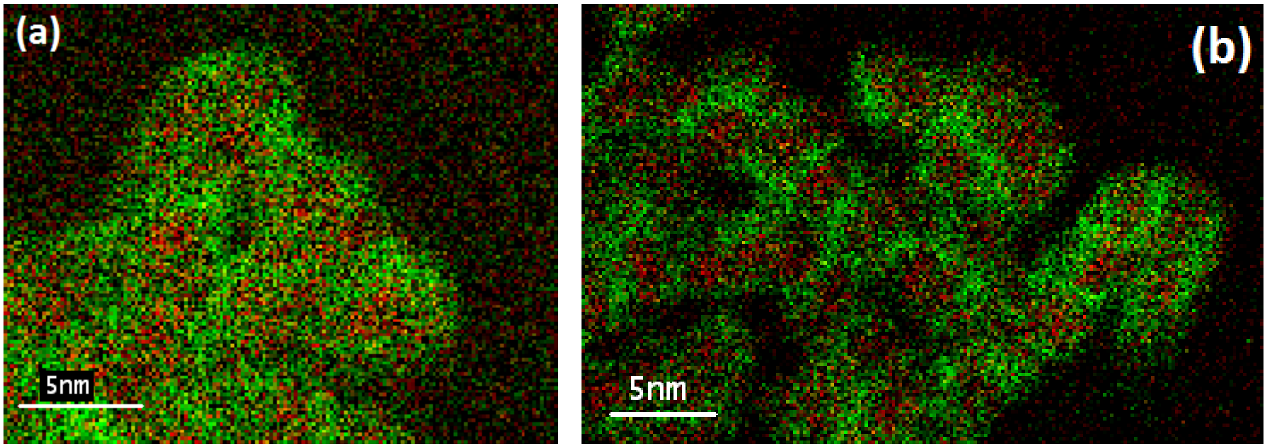

Figure 4.30: EELS elemental mapping of Ru and Pt in PtRu NPs on HOPG at (a) room temperature, (b) 650°C, in deposit 1.

4.5.2 Deposit 2

Figures 4.31 and 4.32 present STEM photomicrographs and EELS maps of the as-deposited NPs, and those annealed at 650°C for 1 h, respectively. The FIB technique was used in both deposits 2 and 3 because of the advantage it provides in determining the relative positions of elements with respect to the substrate, when used to prepare cross-sections. The HAADF image (Fig. 4.31a) shows a continuous bright band due to the overlap of several particles within the thickness of the cross-section. The elemental distributions of Pt (green) and Ru (red) (Fig. 4.31b) are identical, as shown by uniform distribution of colors (in contrast to deposit 1, where the distribution is clearly different for the two maps). Due to the fact that the measurements on the FIB cross-section are done in projection, we also carried out EELS measurements with a tilted sample (approximately 12 degrees) so as to ensure that the identical distribution of Pt and Ru is not only due to the averaging of composition over several particles in projection. The HAADF image (Fig. 4.31c) now shows the individual particles over the substrate (dark area identified in the figure) and under the protective capping layer of carbon and tungsten (bright band at the top of the image). As shown in Fig. 4.31 d, the individual particles are now visible and the distribution of Ru (red) and Pt (green) is again uniform, confirming that individual particles are indeed also composed of Pt and Ru, uniformly distributed. After annealing at 650°C the NPs also exhibit uniform Pt and Ru distributions at the individual level, as shown in the maps obtained from the tilted cross-section (Fig. 4.32). Therefore, in deposit 2, both at room temperature and at 650°C, it appears that Ru and Pt mixed throughout the layer with no distinctive spatial separation.

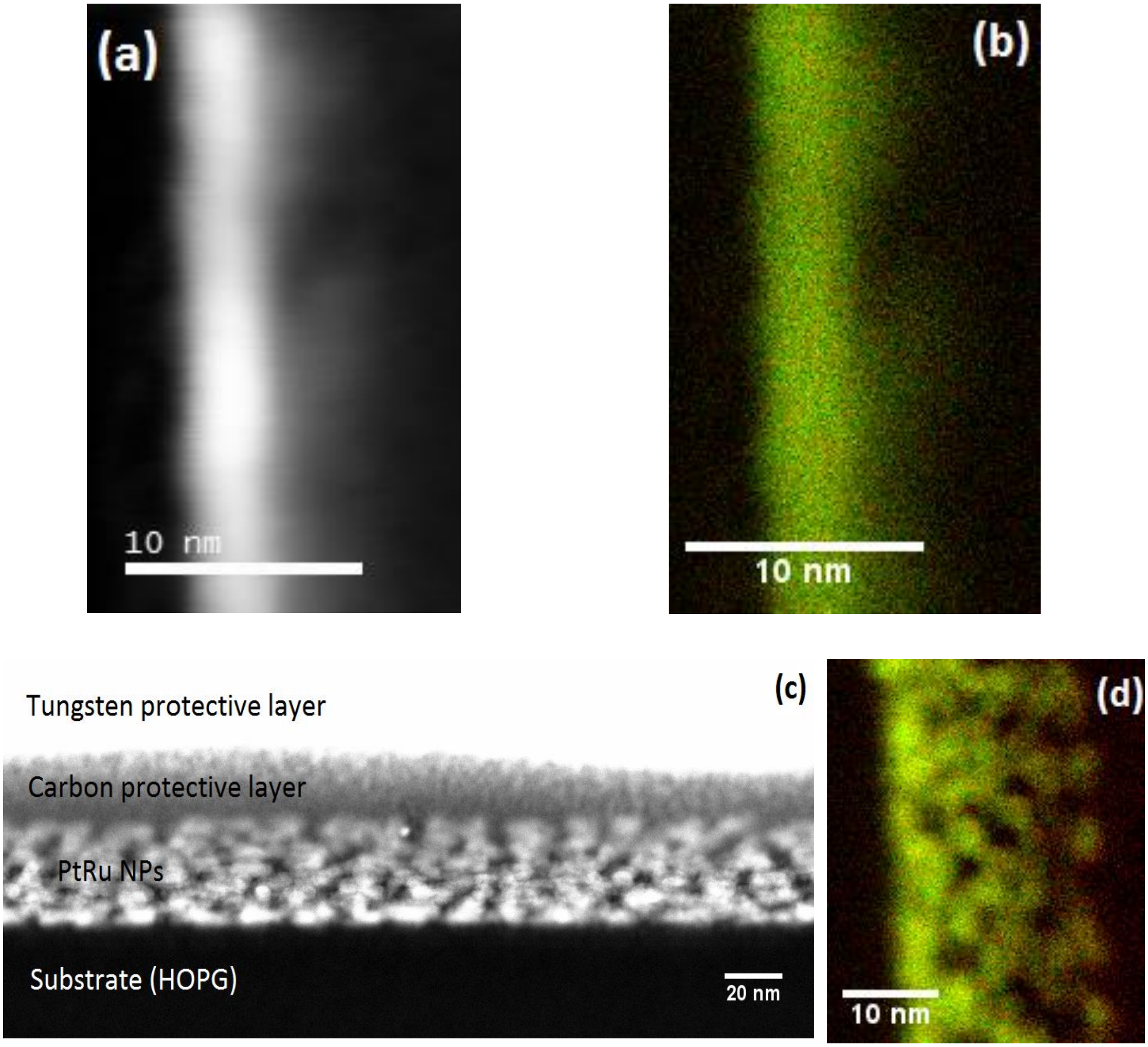

Figure 4.31: (a) STEM-HAADF image of the cross-section of deposit 2; (b) EELS elemental map of Pt (green) and Ru (red). The uniform blend of colors indicates that the Pt and Ru distribution is uniform. (c) cross-sectional STEM image of PtRu NPs on HOPG at room temperature, obtained when the sample is tilted; The substrate, the PtRu nanoparticles and the protective layers are indicated; (d) EELS elemental mapping of Pt (green) and Ru (red) obtained when deposit 2 the sample is tilted by about 12 degrees and as shown in the HAADF image (c).

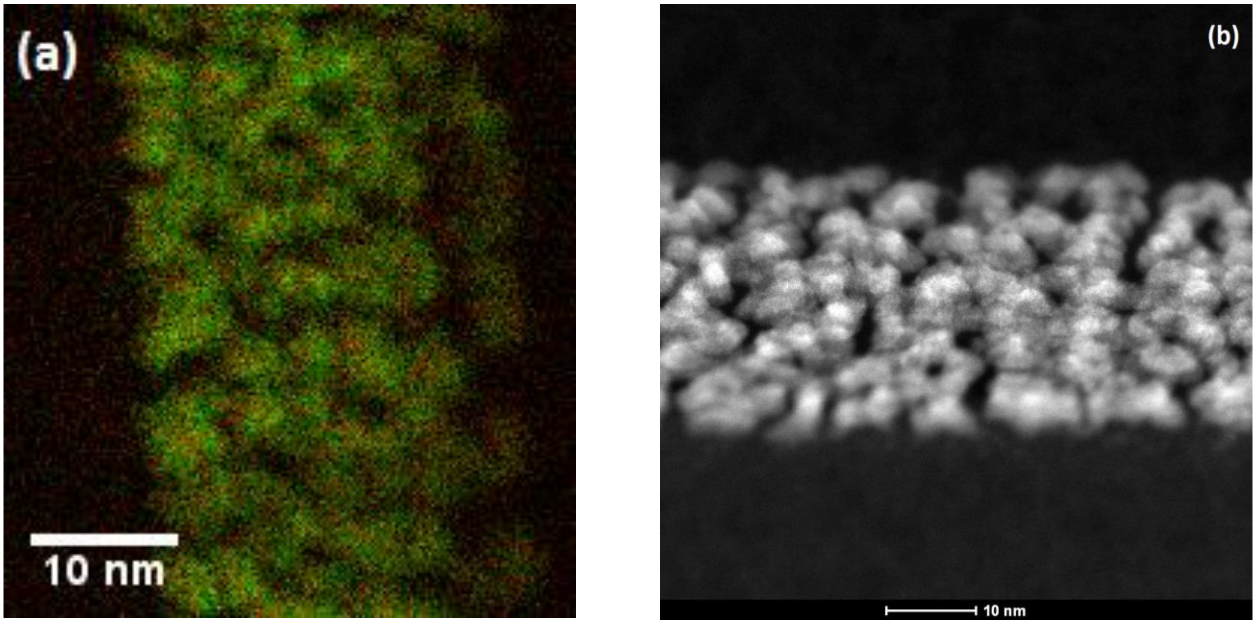

Figure 4.32: (a) EELS elemental map (b) STEM image, of PtRu NPs on HOPG annealed at 650°C, in deposit 2. The sample is slightly tilted, as discussed in Fig. 4.31, to show the individual particles, so that the apparent thickness is not representative of the actual deposit thickness.

4.5.3 Deposit 3

Figures 4.33 and 4.34 show EELS maps of the as-deposited NPs, and those annealed at 650°C for 1 h. At room temperature, Pt (shown in green in the elemental map) is located below Ru, as seen in Fig. 4.33. In this deposit, both Ru and Pt appear as layers to the projection, in which, at some locations, interdiffusion appears to occur. However, due to the non-continuous layer deposition (particles form, instead of a continuous film), some Ru also appears, in a few instances, in direct contact with the substrate.

In the sample annealed at 650°C, Fig. 4.34, there is a clear separation between Pt and Ru. It appears that only Pt forms particles, and Ru surrounds them as layers, always on the top portion of the particles.

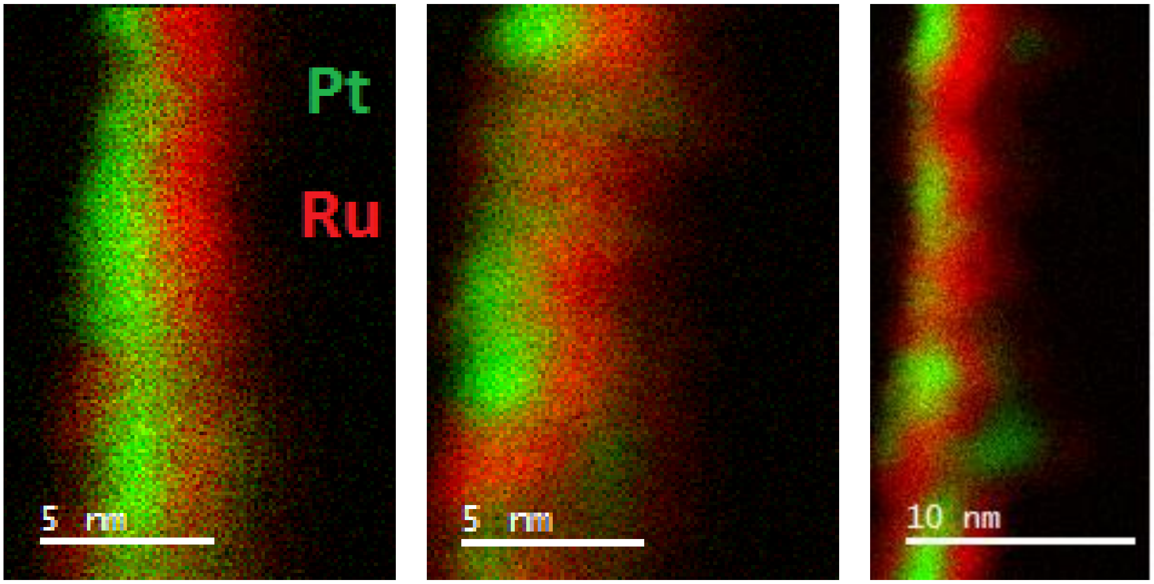

Figure 4.33: EELS elemental mapping of PtRu NPs on HOPG at room temperature, in deposit 3. The HOPG substrate is on the left side of the image.

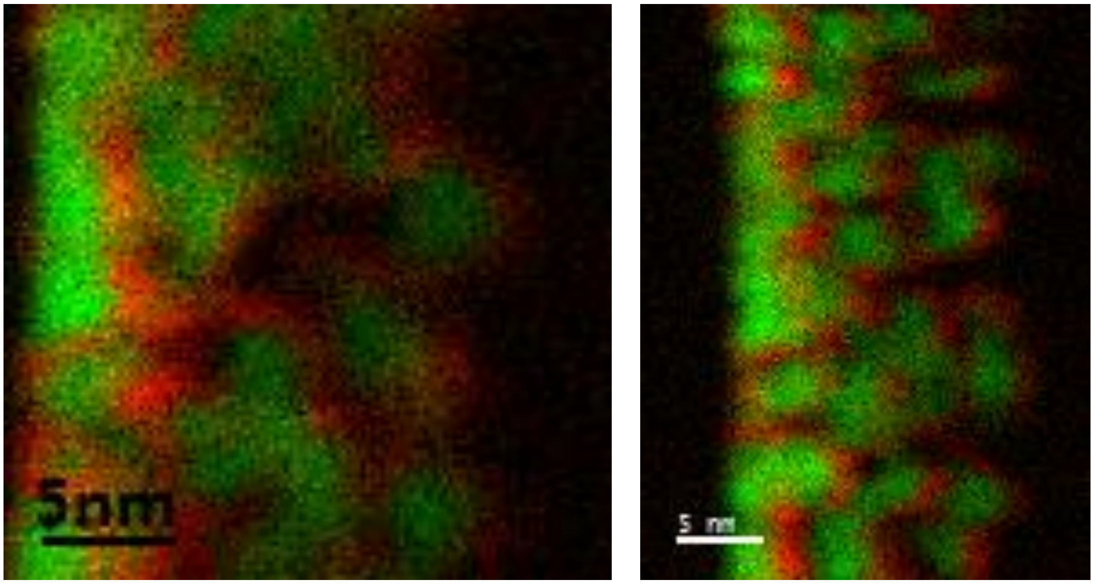

Figure 4.34: EELS elemental mapping of PtRu NPs on HOPG annealed at 650°C, in deposit 3. The HOPG substrate is on the left side of the image.

4.6 PtRu Alloy NP Formation during the Annealing Process

It is clear that the PtRu alloy structure evolves during the various deposition and annealing processes. In all three deposits, the *initial* interdiffusion of Ru and Pt occurs because of the release of the heat of condensation of the depositing metals. That is, the heats of condensation of both Pt and Ru (~5 and ~6 eV, respectively) are great enough to cause interdiffusion and alloying on initial deposition, even before the formal annealing process had begun.

For deposit 1, the temperature evolution of the Ru and Pt fwhm values (Fig. 4.4) and the relative ratios of the components (Fig. 4.5) indicate two points of inflection, one over the range 250°-350°C and the other at 715°C. Below 250°C, annealing causes only very small changes in the NPs, as seen in Figs. 4.4-4.6a and 7b. Over the range of 250°-350°C, Ru and Pt interdiffuse rapidly. Babu *et al.* [7] and Huang *et al.* [49] found that Ru is the metal that diffuses into Pt, eventually reaching the surface; this is confirmed in our XPS experiments, as shown in Figs. 4.6a and b, and in our TOF-SIMS results (Fig. 4.14). The Ru-rich surface layer thickens over this temperature range, forming larger Ru clusters, Ru_2^+ and Ru_3^+ (Fig. 4.15). In addition, the EELS map (Fig. 4.30a) confirms the Pt segregation at the surface, upon deposition. This is followed by Ru diffusion to the NP surface on increasing the annealing temperature, as seen in Fig. 4.30b.

Antolini *et al.* [48] and Lust *et al.* [127] have reported, using X-ray diffraction, that crystalline PtRu alloy, produced by chemical reduction, forms from an atomically uniform crystalline mixture of the two elements only at ~ 350°C and, as found by Antolini *et al.* [48], the crystal then undergoes perfection as the annealing temperature is raised. Our HAADF/STEM results also show a more perfect lattice, with sintering, of the Pt-rich regions of PtRu NPs (that causes the Ru-rich regions of the PtRu NPs to be exposed to the surface), at elevated temperatures, rather than distinct patches containing predominantly Ru or Pt atoms, at room temperature. Figure 4.35 shows the Ru3:O1, Pt3:O1, and Pt3:Ru3 atomic ratios of deposit 1, as a function of annealing temperature. At higher temperatures, both the Ru3:O1 and Pt3:O1 ratios undergo significant increases as the oxides decompose, while the Pt3:Ru3 ratio becomes constant at 1:1, as expected for PtRu. That is, the decomposition of the surface oxides signals the formation of the PtRu alloy at the surface, unlike other cases, in which the alloy forms in the core [3, 6, 125, 128]. Thus, the 1:1 PtRu crystal alloy forms above 350°C, where oxygen is lost, and undergoes perfection as the temperature is raised. This is surely due, as mentioned earlier, to the fact that Ru and Pt differ in size by less than 3 %. While the process occurring above 700°C also appears to be an interdiffusion (see Figs. 4.4 and 4.5), we cannot presently associate it with any known process occurring in that temperature range. At the moment, it remains unattributed.

Below the decomposition temperatures of the oxides, the Pt3:Ru3:O1 ratio is 1:1:1, suggesting the existence of a Pt-O-Ru complex oxide. Pt-O-Ru fragments, which probably exist as Ru^+-O-Pt^- dipolar fragment, could not be identified using TOF-SIMS, although all of the possible decomposition fragments of this complex, such as Ru^+, Pt^-, RuO^+, and PtO^-, have been found separately.

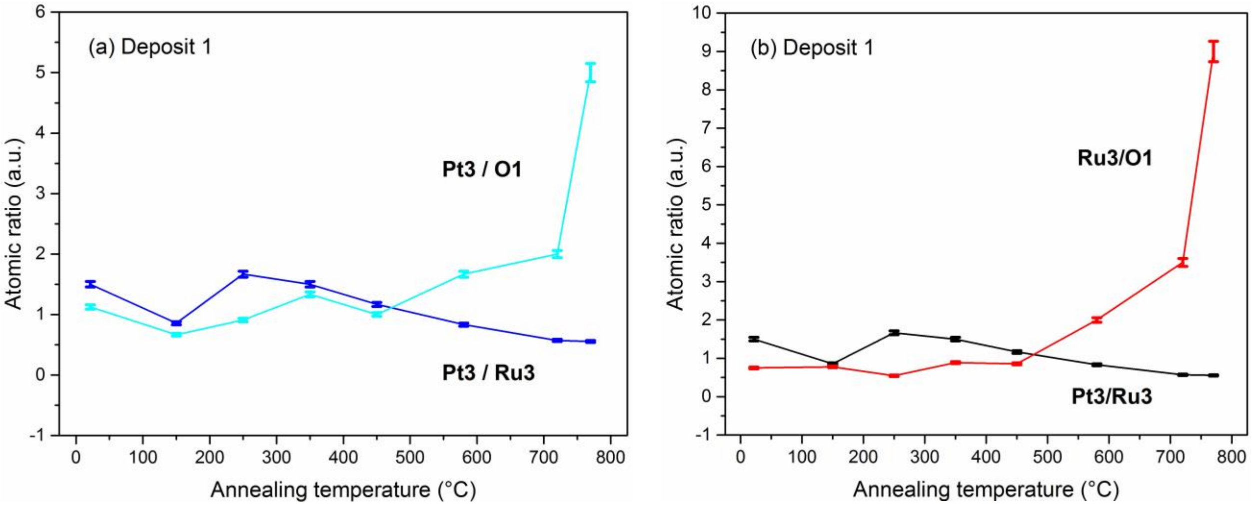

Figure 4.35: Atomic ratios of Pt3/Ru3 and (a) Pt3:O1, (b) Ru3:O1, as a function of annealing, for deposit 1.

In contrast to deposit 1, the temperature evolution of the Ru and Pt fwhm values and component fractions (Fig. 4.19a), and the Pt:Ru atomic ratio (Fig. 4.19c) of deposit 2 (in which Ru and Pt are deposited simultaneously) do not indicate any significant points of inflection. TOF-SIMS analysis demonstrates the minor diffusion of Pt (Fig. 4.20b), but no major diffusion of Ru (Fig. 4.20a). It should be noted that, because of the similarity of Pt and Ru sizes, they can form PtRu alloy crystals with compositions other than [129] that found for deposit 1. Both HAADF/STEM and EELS (Figs. 4.31 and 4.32) confirm that, in contrast to deposit 1, individual NPs consist of Pt and Ru, uniformly distributed, upon deposition and after annealing. These results also indicate that there are PtRu alloys formed in the as-deposited as well as in the annealed samples, similar to what was found in deposit 1.

In the case of deposit 3, where Ru is deposited onto Pt, no abrupt changes were found in any of the correlation plots, nor was any major diffusion of Ru seen by TOF-SIMS analysis (Fig. 4.25a). As Ru is the major diffuser, and is already at the surface, little further interdiffusion is observed for deposit 3, in EELS mapping (Figs. 4.33 and 4.34). The interdiffusion and alloying seen in this deposit is due to the minor diffusion of Pt (recall the presence of $Pt_xC_yH_z$ at the surface) away from the surface, and also the separation between Pt and Ru, on annealing. Identical to what was found for deposit 2, the similar sizes of Pt and Ru permit the formation of PtRu in ratios other than 1:1.

In summary, in all deposits, a PtRu alloy forms upon deposition, although with various structural and elemental distributions of Pt and Ru. In addition, above 350°C, where oxides decompose, a PtRu crystal alloy forms, and undergoes perfection on annealing. However, the Ru:Pt ratio is not identical in all deposits. It ranges from an average of 15 % Pt, for deposit 3, to 50 % for deposit 1, all near the surface.

4.7 Attributions of Ru and Pt XPS Components

In all the deposits, the Ru and Pt XPS spectra were separated into 3 symmetric components. Except for the first components, Ru1 and Pt1, which are due to Ru and to surface Pt in their own environments, the attributions of the second (Ru2 and Pt2) and third (Ru3 and Pt3) components differ for each of the deposits despite their being at essentially the same binding energies; this is because the binding energy values are indicative of the electron densities at the emitting atoms, influenced by their physical and/or their chemical structures.

4.7.1 Deposit 1

Comparing the binding energies of Ru and Pt with those of the pure metals [1, 124] (see Tables 4.1 and 4.2), it is clear that the first component of Ru (Ru1) is due to Ru° in a Ru environment. Similarly, the first component of Pt (Pt1) is due to surface Pt° in a Pt environment. As shown in Fig. 4.5, the second components of both Ru and Pt are attributed to the interactions between these two metals: Ru diluted in a Pt environment (Ru2), and both Pt diluted in a Ru environment and the volume component of pure Pt (Pt2), (see Table 4.2 for pure Pt). These two phases, with a composition varying between Ru and Pt, including some Pt in Ru-rich areas, and some Ru in Pt-rich areas, could be easily seen in Figs. 4.29 and 4.30. Both XPS (Fig. 4.35) and TOF-SIMS (Fig.

4.18) suggest that the third components of Ru and Pt (Ru3 and Pt3, respectively) are due, below 350°C, to a mixed oxide at the surface because, as noted above, (1) the Ru3:Pt3:O1 ratio is essentially constant below 450°C (Fig. 4.35), and (2) we found Ru and Pt oxide fragments by TOF-SIMS (Fig. 4.18).

At higher temperatures, above 350°C, as mentioned earlier, the Pt3:Ru3 ratio becomes constant at 1:1, so that we attribute Ru3 and Pt3 to the formation of a PtRu alloy crystal. A complete XPS identification of all the elements in deposit 1, at room temperature, is shown in Table 4.4.

Table 4.4 : Peak components and attributions for deposit 1, at room temperature, except where noted above 350°C.

Element	Label	Binding energy (eV)	FWHM (eV)	Identification	Relative atomic %
C1s	C1	284.6	1.2	Undamaged alternant hydrocarbon structure	30.0
	C2	285.6	1.6	Damaged alternant hydrocarbon structure	4.8
	C3	286.5	1.6	Free radical defects	6.4
	C4	288.2	3.9	Shake-up of C2	12.1
	C5	291.3	3.9	Shake-up of C1	6.5
	C6	283.3	1.6	Carbide	13.4
O1s	O1	530.9	1.8	Pt-O-Ru mixed oxide	0.8
	O2	532.6	1.8	C─OH	3.0
$Ru3d_{5/2}$	Ru1	280.2	1.1	Ru^0	7.9
	Ru2	281.1	1.1	Ru diluted in a Pt environment	1.6
	Ru3	282.0	1.1	Pt-O-Ru mixed oxide *Above 350°C:* 1:1 PtRu alloy crystal	0.6
$Ru3d_{3/2}$	Ru1'	284.3	1.1	Ru^0	
	Ru2'	285.2	1.1	Ru diluted in a Pt environment	
	Ru3'	286.2	1.1	Pt-O-Ru mixed oxide	

Table 4.4: (Continued) Peak components and attributions for deposit 1, at room temperature, except where noted above 350°C.

				Above 350°C: **1:1 PtRu alloy crystal**	
Pt4f$_{7/2}$	**Pt1**	**71.4**	**1.4**	**Pt (probably in surface)**	**9.6**
	Pt2	**72.3**	**1.4**	**Pt diluted in a Ru environment**	**2.3**
	Pt3	**73.4**	**1.4**	**Pt-O-Ru mixed oxide** ***Above 350°C:*** **1:1 PtRu alloy crystal**	**0.9**
Pt4f$_{5/2}$	**Pt1'**	**74.7**	**1.4**	**Pt (probably in surface)**	
	Pt2'	**75.6**	**1.4**	**Pt diluted in a Ru environment**	
	Pt3'	**76.7**	**1.4**	**Pt-O-Ru mixed oxide** ***Above 350°C:*** **1:1 PtRu alloy crystal**	

4.7.2 Deposit 2

Both Ru and Pt appear at the surface, with the atomic fraction of Ru greater than that of Pt. As already noted, the heat generated from metal vapor condensation is enough to permit more Ru to diffuse to the surface. The attributions of Ru1 and Pt1 are identical to those of deposit 1: Ru° in a Ru environment and surface Pt° in a Pt environment.

For deposit 1, only one inorganic oxygen component (O1) was found, and was attributed to a mixed Pt-O-Ru oxide, as discussed in the previous section. However, deposit 2 contains two inorganic oxygen components, O1 and O2, shown in Fig. 4.8. Based on our previous studies [1, 124] of pure Ru and Pt, Ru forms two type of oxides; one of them is related to O2 (Table 4.1), and Pt2 is due to Pt in the NP volume (Table 4.2). This indicate us that Ru2 and Pt2 in deposit 2 have similar attributions to those of pure Ru and Pt. Particularly at lower temperatures. Ru2 and Pt2 are also expected to contain contributions of Ru diluted in a Pt environment and Pt diluted in a Ru environment, as with deposit 1. The complete XPS attributions of all the components in deposit 2, at room temperature, are found in Table 4.5.

Concerning the O1 component, Fig. 4.36 shows that the Pt3:Ru3:O1 ratio is not 1:1:1, as was found for deposit 1 (Fig. 4.35). Again based on our previous studies [1, 124] on Pt and Ru, both Pt3 and Ru3 oxides have components in the O1 spectrum (see binding energies in Table 4.1, 4.2, and 4.5), suggesting the formation of oxides at lower temperatures, (recall that both Pt and Ru exist at the surface), although not the Ru-O-Pt mixed oxide (shown in Figure 4.36), that was found for deposit 1. Both Ru and Pt oxides are detected in the TOF-SIMS results (Fig. 4.23). Both Figures 4.36 and 4.37 show a decrease of O1 as a function of annealing temperature, as the oxides decompose. In our previous study [124] on Ru NPs, we found that the ratio between the Ru3 and O1 was 1:1. Using this ratio, and subtracting the Ru oxide ratio from Ru3, we obtain the true value of Ru in a PtRu alloy environment, after oxide decomposition, as seen in Fig. 4.37. The Pt3:Ru3 atomic ratio is found to be quite low and constant, at ~ 0.2, which does not indicate the formation of a 1:1 Pt:Ru crystal. The inflection at 350ºC is clearly seen in Fig. 4.36a, suggesting crystal formation, and Pt-Ru phase diagrams [129] indicate the presence of a stable structure having this atomic ratio.

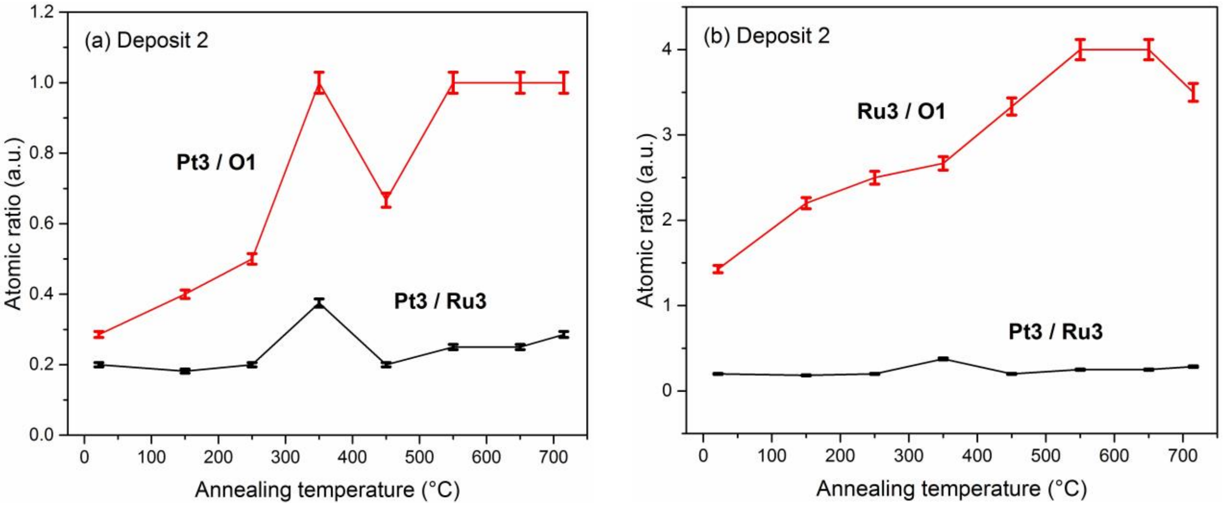

Figure 4.36: Atomic ration of (a) Pt3:O1, (b) Ru3:O1, and Pt3:Ru3, as a function of annealing, for deposit 2.

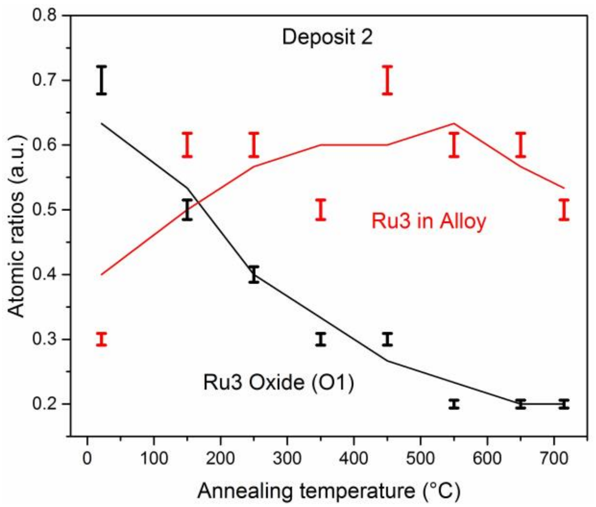

Figure 4.37: Atomic ratio of O1, which is subtracted from Ru3; the remainder is Ru3 in PtRu alloy (deposit 2).

Table 4.5 : Peak components and attributions for deposit 2, at room temperature, except where noted above 350°C.

Element	**Label**	**Binding energy (eV)**	**FWHM (eV)**	**Identification**	**Relative atomic %**
C1s	**C1**	**284.6**	**1.0**	**Undamaged alternant hydrocarbon structure**	**19.6**
	C2	**285.6**	**1.6**	**Damaged alternant hydrocarbon structure**	**7.0**
	C3	**286.5**	**1.6**	**Free radical defects**	**7.8**
	C4	**288.2**	**3.9**	**Shake-up of C2**	**15.5**
	C5	**291.3**	**3.9**	**Shake-up of C1**	**10.5**
	C6	**283.1**	**2.0**	**Carbide**	**21.8**
O1s	**O1**	**530.1**	**1.8**	**Ru and Pt oxides**	**0.7**
	O2	**531.8**	**1.8**	**Ru Oxide**	**1.8**
	O3	**532.7**	**1.8**	**C─OH**	**0.8**
$Ru3d_{5/2}$	**Ru1**	**280.1**	**1.0**	**Ru^0**	**7.1**
	Ru2	**281.1**	**1.0**	**Ru2 (component) Oxide**	**2.1**

Table 4.5: (Continued) Peak components and attributions for deposit 2, at room temperature, except where noted above 350°C.

				Above 350°C: **Ru diluted in a Pt environment**	
	Ru3	**281.9**	**1.0**	**Ru3 (component) Oxide** ***Above 350°C:*** **PtRu alloy crystal, although not with a ratio of 1:1**	**1**
Ru3d$_{3/2}$	**Ru1'**	**284.3**	**1.0**	**Ru^0**	
	Ru2'	**285.3**	**1.0**	**Ru2' (component) Oxide** ***Above 350°C:*** **Ru diluted in a Pt environment**	
	Ru3'	**286.1**	**1.0**	**Ru3' (component) Oxide** ***Above 350°C:*** **PtRu alloy crystal, although not with a ratio of 1:1**	
Pt4f7/2	**Pt1**	**71.6**	**1.4**	**Pt (probably in surface)**	**3.4**
	Pt2	**72.6**	**1.4**	**Pt in volume** ***Above 350°C:*** **Pt diluted in a Ru environment**	**0.5**
	Pt3	**73.7**	**1.4**	**Pt3 (component) Oxide** ***Above 350°C:*** **PtRu alloy crystal, although not with a ratio of 1:1**	**0.2**
Pt4f5/2	**Pt1'**	**75.0**	**1.4**	**Pt (probably in surface)**	
	Pt2'	**75.9**	**1.4**	**Pt in volume** ***Above 350°C:*** **Pt diluted in a Ru environment**	
	Pt3'	**77.0**	**1.4**	**Pt3' (component) Oxide** ***Above 350°C:*** **PtRu alloy crystal, although not with a ratio of 1:1**	

4.7.3 Deposit 3

Since Ru is deposited on Pt in deposit 3, and remains at the surface, while Pt does not have much of a tendency to diffuse into Ru, there is little tendency to change. Ru1 and Pt1 are, as previously, due to Ru° in a Ru environment and surface Pt° in a Pt environment. As for deposit 2, we found two inorganic oxygen components in deposit 3. The atomic percentage of Ru2 is in the range of 1.8 to 1.4 on annealing, while that of Pt2 is constant, at 0.3. As with deposits 1 and 2, both Ru2 and Pt2 must be due, at least in part, to the interactions between them. Ru2 also appears to have an oxide contribution, correlating with O2, as shown in Fig. 4.38. The atomic ratio between Ru2:O2 is essentially 1:1 below its decomposition, below 350°C, as seen in Fig. 4.38a, suggesting a contaminant surface oxide. In our previous study on Ru NPs [124], we found that the ratio between the Ru2 and O2 was 1.3:1. Using this ratio, and subtracting the Ru oxide ratio from Ru2, we obtain an estimate of the value of Ru diluted in a Pt environment, as shown in Fig. 4.38b (the negative value for Ru in a Pt environment, below ~ 300ºC, is attributed to both deconvolution and measurements errors). This figure, along with Figure 4.38a, indicates oxide decomposition at higher temperatures, at which point Ru2 interacts with Pt2.

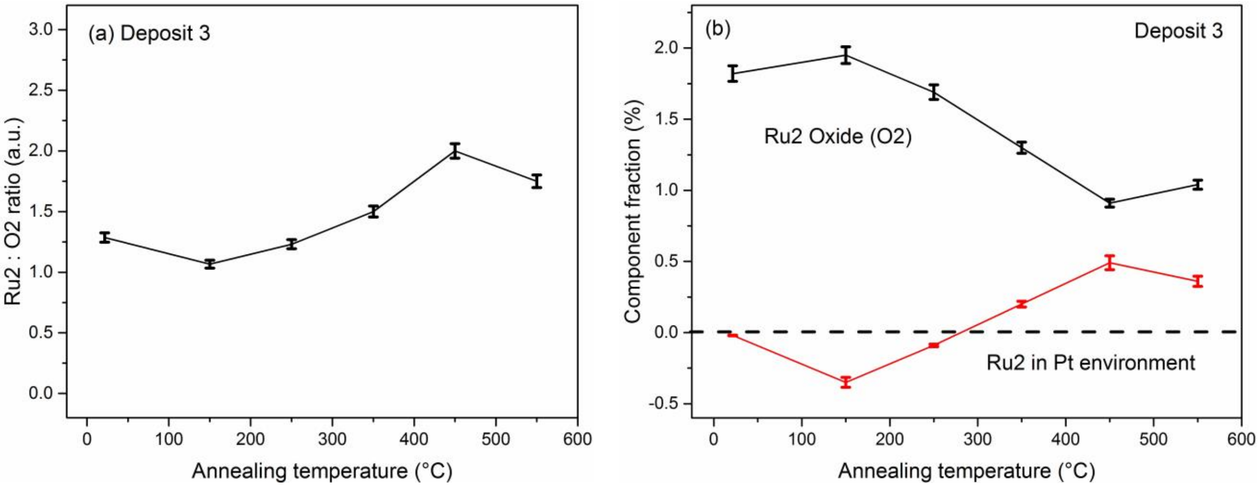

Figure 4.38: (a) Evolution of the Ru2: O2 atomic ratio for PtRu NPs (b) Atomic ratio of O2, which is subtracted from Ru2; the leftover is Ru2 in Pt environment (deposit 3); the negative values are uncertainties due to measurements.

The attributions of Ru3 and Pt3 are similar to those of deposit 2. The atomic percentage of Pt3 is constant at 0.1, while that of Ru3 is also constant, at ~ 0.6-0.7. As with deposit 2, Pt-Ru phase diagrams [129] indicate the presence of a stable PtRu structure having this atomic ratio. As seen in Fig. 4.39, the Pt3:Ru3:O1 is not 1:1:1. A complete XPS identification of all the elements in deposit 1, at room temperature, is shown in Table 4.6.

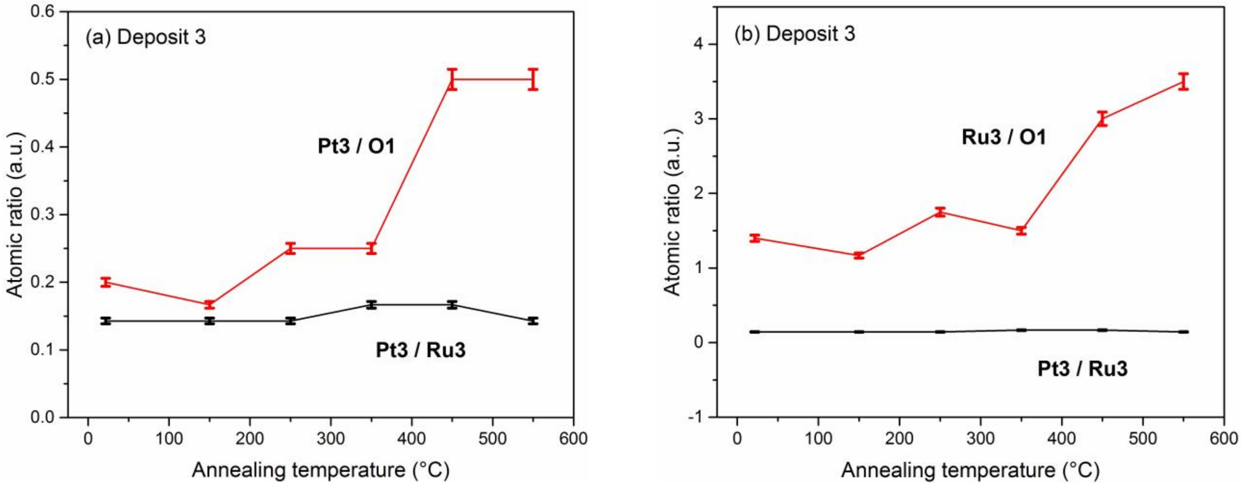

Figure 4.39: Atomic ration of (a) Pt3:O1, (b) Ru3:O1, and Pt3:Ru3, as a function of annealing, in deposit 3.

Table 4.6: Peak components and attributions for deposit 3, at room temperature, except where noted above 350°C.

Element	Label	Binding energy (eV)	FWHM (eV)	Identification	Relative atomic %
C1s	**C1**	**284.6**	**1.0**	**Undamaged alternant hydrocarbon structure**	**23.7**
	C2	**285.6**	**1.6**	**Damaged alternant hydrocarbon structure**	**6.5**
	C3	**286.5**	**1.6**	**Free radical defects**	**7.2**
	C4	**288.2**	**4.0**	**Shake-up of C2**	**15.1**
	C5	**291.3**	**4.0**	**Shake-up of C1**	**9.6**
	C6	**283.3**	**2.0**	**Carbide**	**22.8**
O1s	**O1**	**530.2**	**1.8**	**Ru and Pt Oxides**	**0.5**
	O2	**531.8**	**1.8**	**Ru Oxide**	**1.4**
	O3	**533.3**	**1.8**	**C─OH**	**0.5**

Table 4.6: (Continued) Peak components and attributions for deposit 3, at room temperature, except where noted above 350°C.

Ru3d$_{5/2}$	**Ru1**	**280.0**	**1.0**	**Ru^0**	**8.6**
	Ru2	**280.8**	**1.0**	**Ru2 (component) Oxide** ***Above 350°C:*** **Ru diluted in a Pt environment**	**1.8**
	Ru3	**281.7**	**1.0**	**Ru3 (component) Oxide** ***Above 350°C:*** **PtRu alloy crystal, although not with a ratio of 1:1**	**0.7**
Ru3d$_{3/2}$	**Ru1'**	**284.2**	**1.0**	**Ru^0**	
	Ru2'	**285.0**	**1.0**	**Ru2' (component) Oxide** ***Above 350°C:*** **Ru diluted in a Pt environment**	
	Ru3'	**285.9**	**1.0**	**Ru3' (component) Oxide** ***Above 350°C:*** **PtRu alloy crystal, although not with a ratio of 1:1**	
Pt4f7/2	**Pt1**	**71.4**	**1.5**	**Pt (probably in surface)**	**1.3**
	Pt2	**72.5**	**1.5**	**Pt in volume (very low)** ***Above 350°C:*** **Pt diluted in a Ru environment. Although the relative contribution of Pt2 in this deposit is less than deposit 2.**	**0.3**
	Pt3	**73.8**	**1.5**	**Pt3 (component) Oxide** ***Above 350°C:*** **PtRu alloy crystal, although not with a ratio of 1:1**	**0.1**
Pt4f5/2	**Pt1'**	**74.7**	**1.5**	**Pt (probably in surface)**	
	Pt2'	**75.9**	**1.5**	**Pt in volume (very low)**	

Table 4.6: (Continued) Peak components and attributions for deposit 3, at room temperature, except where noted above 350°C.

				Above 350°C: **Pt diluted in a Ru environment. Although the relative contribution of Pt2 in this deposit is less than deposit 2.**	
	Pt3'	**77.1**	**1.5**	**Pt3' (component) Oxide** ***Above 350°C:*** **PtRu alloy crystal, although not with a ratio of 1:1**	

4.7.4 Relative concentrations of Ru and Pt in the three deposits

Despite the fact that XPS is quantitative and TOF-SIMS is not, TOF-SIMS can give an indication of the Ru and Pt concentrations near the surface, where catalytic reactions take place. The relative concentrations of Ru and Pt in each deposit are calculated based on the XPS deconvolutions, some of them obtained from Tables 4.4-4.6. These results confirm what was concluded from TOF-SIMS analysis, as previously discussed, although here it is much more precise. Among the three deposits, at room temperature, deposit 1 has the greatest amount of surface Pt and the least amount of surface Ru, and deposit 3 has the greatest amount of surface Ru and the least amount of surface Pt.

As a function of annealing, among these three deposits, deposit 3 again has the greatest amount of Ru and the least amount of Pt. It is interesting to note that, after annealing, the relative concentrations of surface Ru and Pt are close to each other in deposits 1 and 2. We confirmed this by repeating these experiments several times. Both deposits 1 and 2 have less Ru and more Pt at the surface than deposit 3. These results can be employed to understand the catalytic activities of the three alloys.

4.8 The Ultimate Surface Compositions of PtRu Alloy NPs

We find that the method of synthesis employed determines the ultimate structure of the NPs. Although some researchers [3, 4], reported that the surface of PtRu NPs are Pt-rich, our data indicate that Ru diffuses through Pt, coming to the NP surface. This diffusion is significant when Pt is deposited onto Ru, as shown by XPS, TOF-SIMS, HAADF/STEM, and EELS data, which also showed substantially different surface structures for each of the three types of depositions, even when annealed to ~ 700°C. As Calvo [130] pointed out in his review of the thermodynamics of nanoalloys, one of the important issues in this field is that the extensive variety of synthesis methods can lead to very different structures.

We suggest two reasons for the contradictions found in the literature for the ultimate surface structure of PtRu alloy NPs: first, because of its low surface tension, Pt is expected to exist at the surface. Pt has a lower surface tension than Ru at 1000°K (Pt; 1976 mN m^{-1}, Ru; 2271 mN m^{-1}, obtained from an electrostatic levitation facility [131]), well above the temperature at which Ru comes to the surface in deposit 1. Hence, in theory, Pt should predominate at the surface. However, we are not dealing with pure Pt and Ru. Both react with each other and, at the NP surface, with residual gases, to form contaminant layers (oxide, carbide, and hydrocarbon). Ru diffuses to the surface, because it is more reactive to these residual gases than Pt. Given the contaminants at the surface, a Ru-rich surface appears to be more thermodynamically stable.

Second, the ultimate structure of the PtRu alloy NP depends upon the preparation method used. Each of the preparation methods produces a surface structure which differs from those of the others, even after prolonged annealing at temperatures over 700ºC. In addition to surface structure, the surface chemistries and elemental distributions of Pt and Ru of these three deposits are also different. Our XPS, TOF-SIMS, HAADF/STEM, and EELS results show different Pt:Ru ratios for each of the three types of deposition, even after annealing. Moreover, the amounts of carbide and metal oxide at the surface clearly depend upon the amount of each metal at the surface. As a result, no unique equilibrium structure is reached for these preparation methods under the conditions available to us. This makes the aforementioned inconsistencies in the literature understandable. Table 4.7 compares the characteristics of the three deposits.

Because of the difference in surface structure and chemistry in these three types of deposition, each will potentially demonstrate a different catalytic activity. For this reason, we are currently studying the methanol oxidation reactivity of each of these deposits in a working PEM fuel cell.

Table 4.7: The characteristics and differences in deposits 1, 2, and 3.

	Ru & Pt diffusions to the surface	**Changes on annealing**	**Pt:Ru ratio in alloy***	**Concentration of Ru & Pt**	**Type of metal oxides**
Deposit 1	Major diffusion of Ru	The most	**1.2:1**	The most Pt & the least Ru	Mixed oxide Pt-O-Ru
			0.85:1		
Deposit 2	Minor diffusion of both Ru & Pt	Moderate	**0.7:1**	Close to deposit 1 values after annealing	Two types of Ru oxide & Pt oxide (tiny)
			0.8:1		
Deposit 3	Minor diffusion of Pt (less than deposit 2)	The least	**0.15:1**	The most Ru & the least Pt, even after annealing	Two types of Ru oxide & Pt oxide (negligible)
			0.2:1		

*For each deposit, the first row is the ratio obtained at room temperature, and the second row represent the ratio after annealing steps.

4.9 Conclusion

Our use of symmetric peak component XPS analysis, along with TOF-SIMS, HAADF/STEM and EELS, has provided detailed information on a previously unidentified phenomenon, preparation-dependent NP structure. Three different PtRu NP preparations were used, varying the order of metal deposition; deposition of Pt onto Ru, Ru onto Pt and the simultaneous deposition of both metals. Based on the preparation technique used, the PtRu alloy NP structure evolves differently during the various deposition and annealing processes. We found that each of the three types of deposits has unique characteristics. For example, the Pt:Ru ratio in each deposits is different. Overall, the composition of a PtRu alloy NP, its surface structure, and its surface chemistry depend upon its method of preparation. A comparison of the relative surface characteristics of the three deposits would be necessary to understand their different catalytic capacities. Knowing what we already know of each deposit, we expect to have three different catalysts with potentially different performances. Since the details of surface structure and chemistry are now being revealed, an understanding the catalysis mechanism, and how to optimize it, may now be feasible.

CHAPTER 5 PRESENTLY ONGOING RESEARCH – CATALYST EVALUATION

5.1 Introduction

We have begun investigating the methanol oxidation catalytic activities of PtRu NPs deposited onto carbon paper substrates. Except for replacing the original HOPG substrate with carbon paper, which is the substrate used in fuel cells, these are the same NPs whose characterization is described in Chapter 4. Because catalysis occurs at the outer surface, XPS data was characterized to study the surface composition and chemistry at the surface of the NP electrocatalysts. TEM was employed to study their formation, morphology and distribution, which are crucial catalysis parameters.

As described in Chapter 4, we prepared PtRu NPs using three different orders of evaporative deposition: Pt deposited onto Ru, Ru deposited onto Pt and both metals deposited simultaneously, and followed their evolutions as a function of annealing temperature. It was our purpose to investigate which method of deposition, and which state of annealing, produced the best catalyst.

5.2 Experimental

5.2.1 Sample Preparation

Our substrate, HOPG, has not been considered for use in fuel cells. Due to its low price and large sizes available, similarly structured carbon paper is the substrate of choice in fuel cells [132, 133]. Thus, in order to evaluate the catalytic activities of our PtRu alloy NPs under real fuel cell conditions, we deposited the PtRu alloy NPs onto carbon paper. Following our earlier studies [1, 124] of pure Ru and Pt NPs deposited onto HOPG, we prepared PtRu bimetallic materials on the carbon paper substrate, by loading 9.3 nm of Pt (20 µg/cm^2) and 10.3 nm of Ru (13 µg/cm^2), in the three orders of deposition previously used with HOPG (Chapter 4). For all these deposits, we attempted to keep a 1:1 mass ratio, by keeping the deposition rate unchanged. All the electrocatalysts were also annealed at 650°C for 1.5 hours, to study the effect of annealing on their activities. All details concerning the equipment used and experimental conditions are identical to those in Chapter 4.

5.2.2 Electrochemical Measurements

The electrochemical measurements of the variously prepared electrocatalysts were performed using an electrochemical workstation (Autolab-PGSTAT302N) in a conventional three-electrode system, at ambient temperature, under a N_2 atmosphere; these included a Ag/AgCl reference electrode, a platinum wire as counter electrode, and a 1.0 cm × 0.5 cm rectangle of the sample as the working electrode. In each case, the electrode surface was cleaned and activated: cyclic voltammetry (CV) was carried out, between -0.2 and 1.0 V vs. Ag/AgCl in N_2-purged 0.5 M H_2SO_4 solution, at a scan rate of 100 mV s^{-1} for 30 cycles to obtain a stable CV curve. To investigate the activities of various electrocatalysts toward the methanol oxidation reaction (MOR), CV tests were carried out in 0.5 M H_2SO_4 with or without 1.0 M CH_3OH (scan rate: 50 mV s^{-1}, potential range: -0.2 to 1.0 V vs. Ag/AgCl). The catalyst activity was normalized by plotting the unit geometrical area of the catalysts, as well as the Pt content (calculated from our XPS results).

5.3 Electrochemical Performance

The electrocatalytic methanol oxidation activities of the samples were characterized by CV and the resulting MOR voltammograms were treated by removing the background found for the samples in 0.5 M H_2SO_4 under the same conditions; the results are seen in Fig. 5.1. Two obvious anodic peaks (one in the forward scan, one in the backward scan), typical for methanol electro-oxidation, are observed on all the samples during the forward and reverse scans. During the forward scan, there is an obvious shoulder to the left of the principal peak, indicating the presence of two processes. In fact, the methanol oxidation reaction is complicated and may well involve several processes; a detailed explanation for those peaks has not yet been found.

It is believed that the anodic peak during the reverse scan is related to the removal of incompletely oxidized carbonaceous species, collected on the catalyst surface during the forward scan. The area ratio of the forward anodic peak to the backward anodic peak (I_f / I_b) can identify the CO tolerance of the catalyst. Incomplete methanol oxidation to CO_2 during the forward anodic scan, and excessive accumulation of CO on the catalyst surface result in low (I_f / I_b) value. On the other hand, a high (I_f / I_b) value indicates both increased CO tolerance and methanol oxidation [134]. Deposit 2 (simultaneous deposition) and its annealed counterpart exhibit the highest ratios, indicating a great tolerance for CO poisoning, apparently through improved synergistic effects between Pt and Ru under simultaneous deposition. While the initial value for deposit 2 is somewhat higher than that for the annealed sample, XPS reveals that annealing has caused a greater deposition of surface hydrocarbon on annealing; such a deposit may block active catalysis sites on the NP surface. Further studies of MOR efficiency ranking continue.

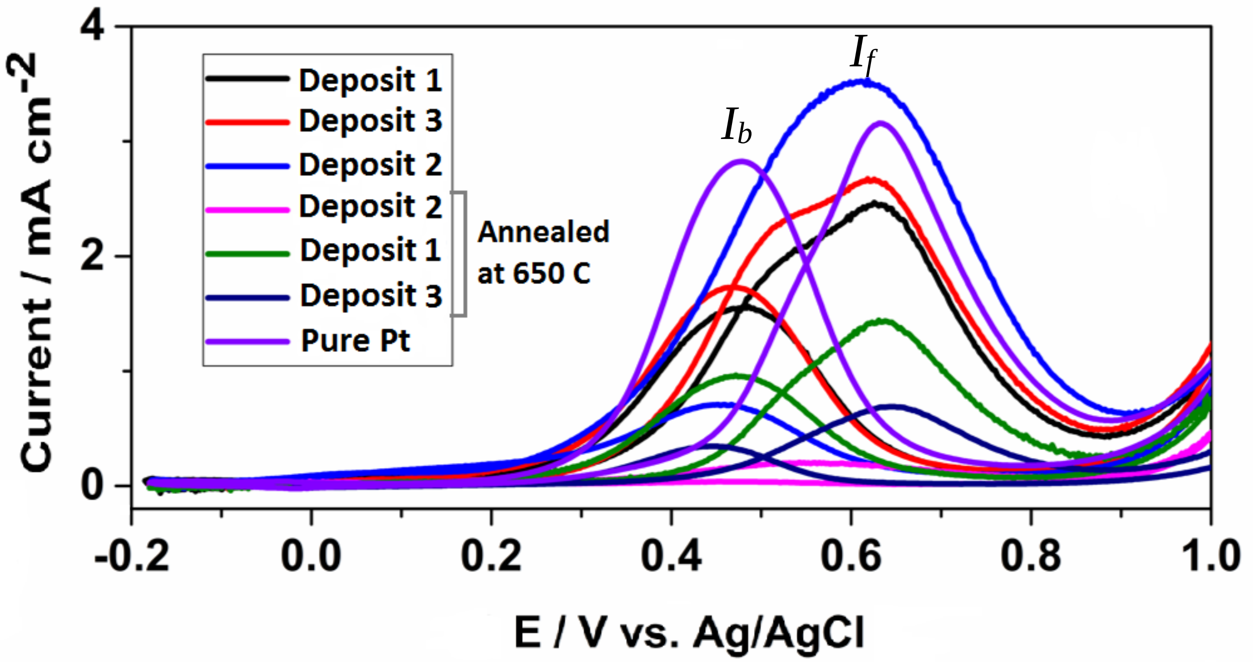

Figure 5.1: CV plots of methanol oxidation for all deposits 1-3 and for pure Pt.

5.4 TEM Analysis

Fig. 5.2 shows TEM photomicrographs of PtRu deposited onto carbon paper at both room temperature and after annealed at 650°C. The EDS spectra of Fig. 5.3 confirm that the NPs contain Pt and Ru. Similar our study [124] of Ru on HOPG, the metals do not wet the carbon paper, causing the metals to retract and form NPs. In addition, based on the results obtained from TOF-SIMS and HAADF/STEM, and EELS in Chapter 4, due to the high heats of condensation of both Pt and Ru (~5 and ~6 eV, respectively), all the prepared NP samples form alloys on initial deposition. In both photomicrographs, many NPs are in contact because of the high number density of NPs formed. However, there is no further aggregation on annealing. This is because both Pt and Ru are present at the surface, and Pt NPs do not diffuse across the surface [1], while

Ru does [124]. That is, NPs containing Pt at their surfaces will not diffuse and coalesce. This indicates that the effective surface areas of these electrocatalyts do not change on annealing. Hence, these electrocatalysts could be used even in the high temperature fuel cells.

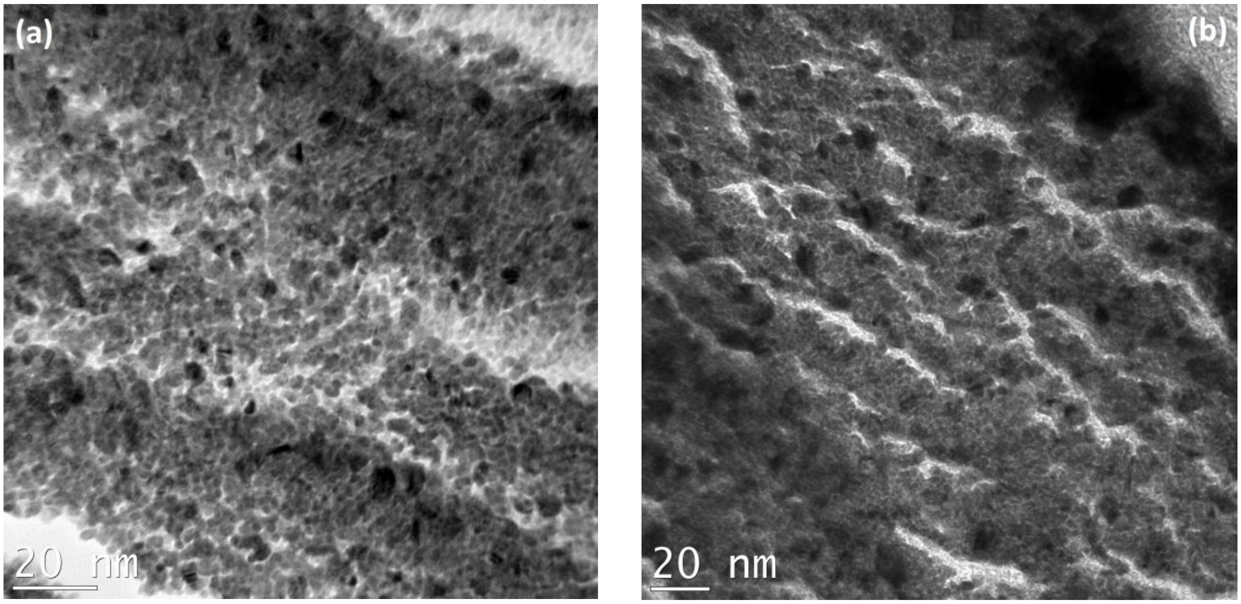

Figure 5.2: TEM photomicrographs of PtRu NPs deposited onto carbon paper at (a) room temperature, (b) after annealed at 650°C.

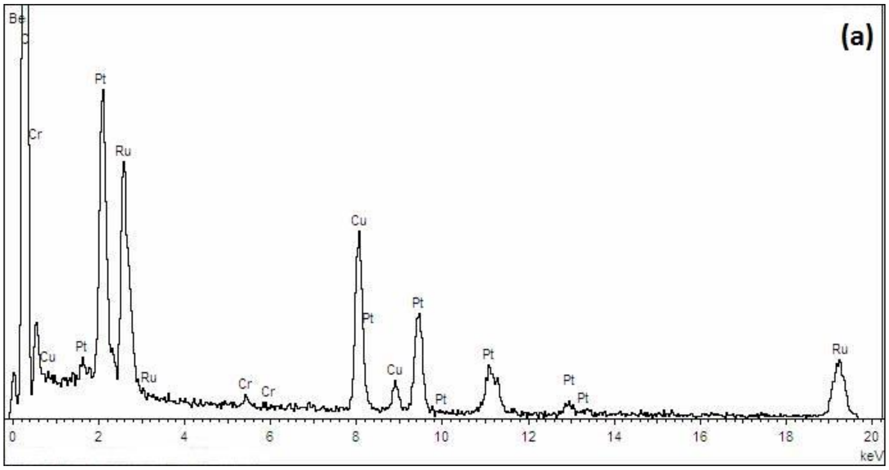

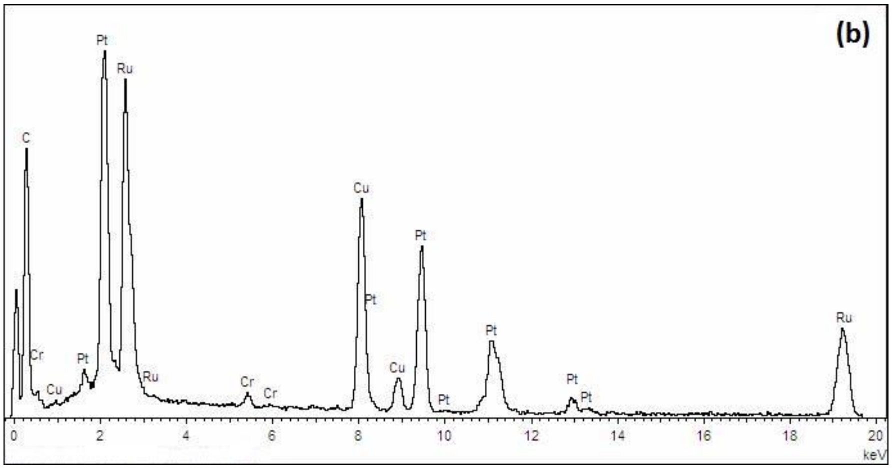

Figure 5.3: EDS spectra of the PtRu NPs shown in Figure 5.2. The Cu peaks come from the support grid.

5.5 Comparison of Electrochemical and XPS Results

The CO tolerance ranking of the various samples, as discussed above, indicate that deposit 2, the simultaneous deposition of Pt and Ru, shows the best catalytic activity among all of the other samples. In order to determine the reasons for this superior performance, the atomic fractions of all the atoms present at the surface are required. Table 5.1 lists the component fraction of Ru, Pt, C, and O in deposits 1-3, both initially and after anneal. These relative concentrations are obtained by XPS, performed on PtRu alloy NPs deposited onto HOPG, as presented in Chapter 4.

For both room temperature and 650°C, deposit 1 has the most surface Pt and the least surface Ru, while deposit 3 has the most surface Ru and the least surface Pt (as shaded in Table 5.1). Thus, the amount of surface Pt and Ru in deposit 2 always lies between those of deposits 1 and 3. This suggests that deposit 2 has a more favorable Pt/Ru surface ratio, leading to superior performance. In addition, as seen in Table 5.1, deposit 2 contains the most metallic and organic oxides.

In all the samples, oxide decomposition occurs above 350°C and the hydrocarbon layer thickness increases on annealing, as discussed in Chapter 4. In all the samples, on annealing, the amounts of surface Pt and Ru decrease, as seen in Table 5.1. This is due to the increased surface hydrocarbon layer. The hydrocarbon layer, especially in deposit 2, may produce or increase some functional group, such as Ru carbide, which may have an effect on MOR efficiency.

Table 5.1: Component fractions of Ru, Pt, C, and O, in deposits 1-3, obtained from XPS data.

		Deposit 1		Deposit 2		Deposit 3	
		RT	**650°C**	**RT**	**650°C**	**RT**	**650°C**
Atomic fraction of Ru	Ru1	8.0	6.5	8.4	5.7	11.5	8.7
	Ru2	1.5	1.3	1.7	1.0	2.1	1.3
	Ru3	0.6	0.5	0.7	0.5	0.9	0.5
	Total Ru	10.1	8.3	10.8	7.2	14.5	10.5
Atomic fraction of Pt	Pt1	8.8	5.6	6.4	4.7	1.4	1.4
	Pt2	1.9	1.2	1.0	0.5	0.4	0.3
	Pt3	0.7	0.5	0.5	0.3	0.2	0.1
	Total Pt	11.4	7.3	7.9	5.5	2.0	1.8
Atomic fraction of oxide	O1	0.7	0.2	0.5	0.5	0.8	0.1
	O2	-	-	2.6	1.0	1.7	0.8
	O1+O2 (Metallic)	-	-	3.15	1.5	2.5	1.0
	O3	2.8	0.5	0.6	0.6	0.4	0.6
	Total O	3.5	0.8	3.8	2.1	3.0	1.6
Atomic fraction of carbon	C1	27.7	28.6	19.6	27	23.7	34.0
	C6 (Carbide)	15.7	20.4	21.8	20.5	22.8	19.6
	Total C	73.2	81.7	76.9	84	80.1	85.8

5.6 Conclusion

Because of the differences in the surface structure and chemistry of these three types of deposition, and before and after annealing, each demonstrated a different catalytic activity. The simultaneous deposition of Pt and Ru, prepared at room temperature, showed the best MOR performance among the other depositions. We suggest that the MOR performance of an electrocatalyst may not depend only upon surface Ru or Pt; it may also depends upon the amount and type of surface oxide, and perhaps the amount of hydrocarbons and carbide, depending on which metal (Ru or Pt) is predominant at the surface.

It appears necessary to prepare PtRu alloy NPs that are annealed to 350°C, and examine their catalytic activities. Since we discovered that simultaneous deposition produces the best electrocatalyst, investigations of this type of deposition, preparing other Pt:Ru ratios, is needed. This study continues, and we present other recommendations for future work in Chapter 6.

CHAPTER 6 CONCLUSION, FURTHER WORK, AND RECOMMENDATIONS

6.1 Conclusions

This thesis deals with the synthesis, and surface and bulk characterizations, of Ru and PtRu alloy NPs, deposited onto HOPG by e-beam evaporation in ultra-high vacuum. The advantage of this method is to prepare highly pure metal and metal alloy NPs, without the surface contamination of metal salt reduction methods, enabling us to study metal interactions with substrate and residual gases at their surfaces.

First, Ru NPs were synthesized at two deposition rates, one at 1.3 nm/min and the other at the much lower deposition rate of 0.13 nm/min; various amounts of Ru were deposited onto freshly cleaved HOPG surfaces: 0.25, 0.5, 1, and 1.5 nm nominal depositions. These were used to investigate the effect of deposition rate on the morphological features of Ru NPs, and the effect of various nominal deposition thicknesses on the electronic structures on the core- and valence levels of the NPs. It was our purpose to chemically and morphologically characterize the Ru NPs by *in-situ* surface-sensitive XPS, using symmetric peak component analysis, a technique developed in our laboratory, as well as by TEM. Core level XPS analysis showed that the Ru NP 3d, 3p, and 3s spectra were all found to be composed of three symmetric components. The first component, at the lowest binding energy, is due to zerovalent Ru, while the two other components are attributed to mixed surface oxides. In addition, the NP surface was shown to possess a hydrocarbon layer, deposited from residual gas hydrocarbons present in the vacuum. This partially reacts to form Ru carbide at the NP surface. Carbide was not found on Pt NPs in our group’s previous study [1]. The analysis of the valence band indicated an increase of the Kubo gap with decreasing NP size, accompanied by an abrupt electron spill-over from the 4d to the 5s orbital at the point at which the electron density of states at the Fermi level becomes zero.

The tendency of Ru NPs to agglomerate was observed, by TEM, at the higher deposition rate, while well-separated Ru NPs were obtained at the lower deposition rate. Aggregation and partial coalescence were found to be due to the weak bonding of the NPs to the substrate. Surface diffusion occurred because, at the higher deposition rate, the Ru NP condensation energy was released too rapidly to dissipate, permitting lateral NP diffusion across the surface, as well as partial oxidation of the hydrocarbon layer forming around the NPs. This detailed information on Ru NPs, obtained by XPS using symmetrical peak components and TEM, indicates the presence of surface oxides and carbide, size distributions and morphological features, and interfacial interaction with the substrate, and is of potential importance for the use of Ru NPs as sensors and catalysts. Knowing the chemical and structural features of pure Ru NPs, especially at the surface, was important for the understanding of the PtRu alloy NPs prepared next.

The structure of PtRu NPs, especially at the surface, as well as their morphology and elemental distributions of Ru and Pt, are determining factors in the catalytic activity of the electrocatalyst. Unfortunately, there are disagreements concerning the surface structure of PtRu NPs, as discussed in Chapters 1 and 4, which create a challenge in interpreting their catalytic behavior and optimizing their performance. In order to understand alloying behavior, and the structures of the alloys formed, in the second phase of the thesis, we used three different orders of deposition: deposition of Pt onto Ru, Ru onto Pt and the simultaneous deposition of both metals, all onto HOPG, as was done for the studies of pure Ru and Pt. The alloy NPs underwent annealing and their structural evolutions were characterized *in-situ*, using XPS and TOF-SIMS. Using symmetric peak component XPS analysis, three components were found for both Pt and Ru, similar to what was found in the studies of pure Pt and Ru, although with different attributions. Ru carbide was formed in all PtRu NPs, although the amount of carbide depended on the order of deposition. The relative concentrations of Ru, Pt, O and C in each deposit are calculated, based on the XPS deconvolutions. It appears that the surface composition is different for each of the three deposits.

Valence level studies were also employed to describe the alloying interactions between the metals. For all three deposits, no obvious shift of component peak positions of the valence level spectra, as a function of annealing, was seen, suggesting that alloying had already started before annealing. The changes seen in the spectral shapes in all the deposits appear to be due to chemical reactions that take place at the surface. A comparison of the shapes of the spectra of pure Ru and Pt with those of each deposit, at room and elevated temperatures, indicated which metal, Ru, Pt, or both, predominantly covers the NP surface. The changes observed in the valence band spectra are consistent with the results of the core level data.

TOF-SIMS detected Pt_xRu_y fragments, indicating alloy formation, and also detected both $Pt_xC_yH_z$ and $Ru_xC_yH_z$ fragments, as well as formation of Ru_2^+, Ru_3^+, and Pt_2^- fragments, showing the presence of both metals at the NP surface, no matter which metal was deposited first, again confirming our XPS results. Both XPS and TOF-SIMS revealed detailed information on a previously unidentified phenomenon, the major diffusion of Ru and minor diffusion of Pt to the surface. We also found different Pt:Ru crystallite ratios for each of the three types of deposition, even when annealed to 600°C and above. This indicates that each of the three types of deposits has unique characteristics, and no universal equilibrium NP is formed on annealing.

In addition, HAADF/STEM and EELS analyses confirmed the diffusion of Ru to the surface, PtRu alloy formation upon deposition, and differences in structural and elemental distributions among the three deposits, as had been indicated by XPS and TOF-SIMS. Deposit 1 showed two phases in distinct patches containing predominantly Ru or Pt, at room temperature, using these techniques. After annealing, these two phases formed a more perfect lattice, with sintering of the Pt-rich regions of particles. In deposit 2, individual particles are composed of Pt and Ru, uniformly distributed, in both as-deposited and annealed samples, with no distinctive spatial separation. In deposit 3, interdiffusion between Pt and Ru, at some locations, and the presence of Ru on the outer levels of the NPs, are exhibited, both at room temperature and on annealing. In all three deposits, HAADF/STEM and EELS did not show any clear uniform Pt shell covering the Ru-rich areas.

In all deposits, PtRu alloys formed upon deposition, although with various structures and elemental distributions. For all three orders of deposition, at about 350°C, interdiffusion occurred between Ru and Pt, when the metallic oxides decompose. In addition, above 350°C, due to the similarities of Pt and Ru dimensions, all three deposits form PtRu alloy crystals with various compositions, which undergo perfection on annealing.

There are several experimental and theoretical studies [3-5, 50], which found that Pt diffused to the surface. This claim may be based on the fact that pure Pt has a lower surface tension than pure Ru. However, we are not dealing with pure Pt and Ru. Both react with each other and, at the NP surface, with residual gases, to form contaminant layers (oxide, carbide, and hydrocarbon). All the characterization techniques used in this study demonstrated that Ru diffuses to the surface, not the reverse. We could not find any specific and detailed reason for the major diffusion of Ru, except, given the contaminants at the surface, a Ru-rich surface appears to be more thermodynamically stable.

In summary, the composition of a PtRu alloy NP, its surface structure, and its surface chemistry depend upon its method of preparation. That is, no identical equilibrium is reached for these preparation methods. This makes the inconsistencies previously found in the literature understandable. We found that surface contamination and the underlying NP structure depend upon the order of metal deposition. Since catalysis occurs at the NP surface, this constitutes a key factor in the fabrication of a desirable PtRu NP catalyst for PEM fuel cells. Knowing what we already know of each deposit, we expect to have three different catalysts, with potentially different performances. These results can be employed to understand the catalytic activities of the three alloys and optimize the desired catalyst.

6.2 Future Work and Recommendations

The research and development of new catalysts for PEMFC and DMFC are still generally based on trial-and-error methods, and require more effort to be understood and optimized. In this thesis, it was shown that a fundamental understanding of the chemical species present at the NP surface, which is preparation-dependent, is one of the major directions leading to improved catalytic activities. This may well be achieved by using a combination of state-of-the-art experimental techniques. In addition, there are several directions in which to extend the research, and further enhance the catalytic activity of an electrocatalyst:

1) Finding an alternative electrocatalyst to Pt, one that offers better CO tolerance, which could be applied in the PEMFC and DMFC operating at low temperature with an acidic electrolyte. Pt-Mo (molybdenum, a non-precious metal) and PtRuMo alloy NPs have been introduced as other substitutes to pure Pt, showing very promising CO-tolerance and higher activity toward CO and methanol electro-oxidation [135-137]. These depend on both composition and Ru–Mo and Pt–Mo interactions, as well as a possible change in the reaction path, promoting the direct oxidation of CHO species to CO_2 without the production of the CO poisoning species [138-140]. Considering the results of our in-depth study on evaporated Pt and Ru, and PtRu alloys, the evaporation of Mo and the

preparation of binary PtMo and ternary PtRuMo alloys would be reasonable paths to follow.

2) If the adhesion of PtRu NPs to their substrate is not strong enough, they will diffuse across the substrate, eventually coalescing, forming larger agglomerates, which would result in decreasing both available catalytic surface and activity. This was observed in our pure Ru study, and diffusion was reduced by decreasing the deposition rate. However, only applying a lower deposition rate is neither enough, nor useful in large scale production, since it does not improve the adhesion of the NPs to the substrate and takes a much longer time, which is not tolerable for the commercialization of fuel cells. Therefore, pre-treatment of the substrate is the way that we suggest for future works. This could be done by creating nucleation sites, such as using magnetron sputtering, Ar^+ bombardment or thermal treatment prior to NP deposition. It is very important to assure the strong adhesion of electrocatalyst NPs to their substrate, and to maintain it over the lifetime of the electrocatalyst.

3) The electrocatalyst surface composition is important to its catalytic activity. However, it may change under the electrochemical environment. *In-situ* XPS, which is quantitative, integrated with electrochemical cells, appears to be an ideal tool to investigate the surface composition of the electrocatalyst before and after catalysis activity. This makes a more accurate correlation between catalytic activity and the composition of the electrocatalysts.

4) In our experiments, the amount of prepared PtRu alloy NPs is too small for practical fuel cell applications. It is important to synthesize these NPs on a larger scale (~ 100 g or more). Taking advantage of what we know about the NP surface chemistry as a function of the deposition method, we should consider large scale evaporative production that gives the same surface chemistry.

BIBLIOGRAPHY

[1] G. Zhang, D.-Q. Yang, and E. Sacher, "X-ray Photoelectron Spectroscopic Analysis of Pt Nanoparticles on Highly Oriented Pyrolytic Graphite, Using Symmetric Component Line Shapes," *Journal of Physical Chemistry C*, vol. 111, pp. 565-570, 2007.

[2] S. Murphy, C. Strebel, S. B. Vendelbo, C. Conradsen, Y. Tison, K. Nielsen, *et al.*, "Probing the crossover in CO desorption from single crystal to nanoparticulate Ru model catalysts," *Physical Chemistry Chemical Physics,* vol. 13, pp. 10333-10341, 2011.

[3] P.-C. Huang, H.-S. Chen, Y.-T. Liu, I. L. Chen, S.-Y. Huang, H. M. Nguyen, *et al.*, "Oxidation triggered atomic restructures enhancing the electrooxidation activities of carbon supported platinum-ruthenium catalysts," *CrystEngComm,* vol. 16, pp. 10066-10079, 2014.

[4] A. G. Harris, C. M. Lukehart, and H. J. Grönbeck, "Anchoring of Pt and PtRu to carbon nanofibers studied by density functional theory calculations," *Carbon,* vol. 77, pp. 880-885, 2014.

[5] B. Prasai, Y. Ren, S. Shan, Y. Zhao, H. Cronk, J. Luo, *et al.*, "Synthesis-atomic structure-properties relationships in metallic nanoparticles by total scattering experiments and 3D computer simulations: case of Pt-Ru nanoalloy catalysts," *Nanoscale,* vol. 7, pp. 8122-8134, 2015.

[6] S. Alayoglu, P. Zavalij, B. Eichhorn, Q. Wang, A. I. Frenkel, and P. Chupas, "Structural and Architectural Evaluation of Bimetallic Nanoparticles: A Case Study of Pt−Ru Core−Shell and Alloy Nanoparticles," *ACS Nano,* vol. 3, pp. 3127-3137, 2009.

[7] P. K. Babu, H. S. Kim, S. T. Kuk, J. H. Chung, E. Oldfield, A. Wieckowski, *et al.*, "Activation of Nanoparticle Pt−Ru Fuel Cell Catalysts by Heat Treatment: A 195Pt NMR and Electrochemical Study," *The Journal of Physical Chemistry B,* vol. 109, pp. 17192-17196, 2005.

[8] R. Devanathan, "Recent developments in proton exchange membranes for fuel cells," *Energy & Environmental Science,* vol. 1, pp. 101-119, 2008.

[9] Y. Lu, S. Du, and R. Steinberger-Wilckens, "One-dimensional nanostructured electrocatalysts for polymer electrolyte membrane fuel cells—A review," *Applied Catalysis B: Environmental,* vol. 199, pp. 292-314, 2016.

[10] J. Wang, B. Li, T. Yersak, D. Yang, Q. Xiao, J. Zhang, *et al.*, "Recent advances in Pt-based octahedral nanocrystals as high performance fuel cell catalysts," *Journal of Materials Chemistry A,* vol. 4, pp. 11559-11581, 2016.

[11] P. J. Ferreira, G. J. la O', Y. Shao-Horn, D. Morgan, R. Makharia, S. Kocha, *et al.*, "Instability of Pt/C Electrocatalysts in Proton Exchange Membrane Fuel Cells: A Mechanistic Investigation," *Journal of The Electrochemical Society,* vol. 152, pp. A2256-A2271, 2005.

[12] S. Litster and G. McLean, "PEM fuel cell electrodes," *Journal of Power Sources,* vol. 130, pp. 61-76, 2004.

[13] H. Liu, C. Song, L. Zhang, J. Zhang, H. Wang, and D. P. Wilkinson, "A review of anode catalysis in the direct methanol fuel cell," *Journal of Power Sources,* vol. 155, pp. 95-110, 2006.

[14] S. Wasmus and A. Küver, "Methanol oxidation and direct methanol fuel cells: a selective review," *Journal of Electroanalytical Chemistry,* vol. 461, pp. 14-31, 1999.

[15] F. J. Rodríguez-Nieto, T. Y. Morante-Catacora, and C. R. Cabrera, "Sequential and simultaneous electrodeposition of Pt–Ru electrocatalysts on a HOPG substrate and the electro-oxidation of methanol in aqueous sulfuric acid," *Journal of Electroanalytical Chemistry,* vol. 571, pp. 15-26, 9/15/ 2004.

[16] V. R. Stamenkovic, B. Fowler, B. S. Mun, G. Wang, P. N. Ross, C. A. Lucas, *et al.*, "Improved Oxygen Reduction Activity on Pt₃Ni(111) via Increased Surface Site Availability," *Science,* vol. 315, pp. 493-497, 2007.

[17] K. Qadir, S. H. Joo, B. S. Mun, D. R. Butcher, J. R. Renzas, F. Aksoy, *et al.*, "Intrinsic Relation between Catalytic Activity of CO Oxidation on Ru Nanoparticles and Ru Oxides Uncovered with Ambient Pressure XPS," *Nano Letters,* vol. 12, pp. 5761-5768, 2012.

[18] S. Mukerjee, S. Srinivasan, M. P. Soriaga, and J. McBreen, "Role of Structural and Electronic Properties of Pt and Pt Alloys on Electrocatalysis of Oxygen Reduction: An In Situ XANES and EXAFS Investigation," *Journal of The Electrochemical Society,* vol. 142, pp. 1409-1422, 1995.

[19] V. R. Stamenkovic, B. Fowler, B. S. Mun, G. Wang, P. N. Ross, C. A. Lucas, *et al.*, "Improved Oxygen Reduction Activity on Pt3Ni(111) via Increased Surface Site Availability," *Science,* vol. 315, pp. 493-497, 2007.

[20] R. M. Darling and J. P. Meyers, "Kinetic Model of Platinum Dissolution in PEMFCs," *Journal of The Electrochemical Society,* vol. 150, pp. A1523-A1527, 2003.

[21] Y. Hu, A. Zhu, Q. Zhang, and Q. Liu, "Preparation of PtRu/C core–shell catalyst with polyol method for alcohol oxidation," *International Journal of Hydrogen Energy,* vol. 41, pp. 11359-11368, 2016.

[22] M. Watanabe and S. Motoo, "Electrocatalysis by ad-atoms: Part II. Enhancement of the oxidation of methanol on platinum by ruthenium ad-atoms," *Journal of Electroanalytical Chemistry and Interfacial Electrochemistry,* vol. 60, pp. 267-273, 4/25/ 1975.

[23] M. Krausa and W. Vielstich, "Study of the electrocatalytic influence of Pt/Ru and Ru on the oxidation of residues of small organic molecules," *Journal of Electroanalytical Chemistry,* vol. 379, pp. 307-314, 12/12/ 1994.

[24] R. Liu, H. Iddir, Q. Fan, G. Hou, A. Bo, K. L. Ley, *et al.*, "Potential-Dependent Infrared Absorption Spectroscopy of Adsorbed CO and X-ray Photoelectron Spectroscopy of Arc-Melted Single-Phase Pt, PtRu, PtOs, PtRuOs, and Ru Electrodes," *The Journal of Physical Chemistry B,* vol. 104, pp. 3518-3531, 2000/04/01 2000.

[25] R. Atanasoski, L. Atanasoska, D. Cullen, G. Haugen, K. More, and G. Vernstrom, "Fuel Cells Catalyst for Start-Up and Shutdown Conditions: Electrochemical, XPS, and STEM Evaluation of Sputter-Deposited Ru, Ir, and Ti on Pt-Coated Nanostructured Thin Film Supports," *Electrocatalysis,* vol. 3, pp. 284-297, 2012.

[26] J. Y. Shen, A. Adnot, and S. Kaliaguine, "An ESCA study of the interaction of oxygen with the surface of ruthenium," *Applied Surface Science,* vol. 51, pp. 47-60, 1991.

[27] R. M. Nielsen, S. Murphy, C. Strebel, M. Johansson, J. H. Nielsen, and I. Chorkendorff, "A comparative STM study of Ru nanoparticles deposited on HOPG by mass-selected gas aggregation versus thermal evaporation," *Surface Science,* vol. 603, pp. 3420-3430, 2009.

[28] R. M. Nielsen, S. Murphy, C. Strebel, M. Johansson, I. Chorkendorff, and J. H. Nielsen, "The morphology of mass selected ruthenium nanoparticles from a magnetron-sputter gas-aggregation source," *Journal of Nanoparticle Research,* vol. 12, pp. 1249-1262, 2010.

[29] X. Liu, K. X. Yao, C. Meng, and Y. Han, "Graphene substrate-mediated catalytic performance enhancement of Ru nanoparticles: a first-principles study," *Dalton Transactions,* vol. 41, pp. 1289-1296, 2012.

[30] S. Guo, X. Pan, H. Gao, Z. Yang, J. Zhao, and X. Bao, "Probing the Electronic Effect of Carbon Nanotubes in Catalysis: NH3 Synthesis with Ru Nanoparticles," *Chemistry – A European Journal,* vol. 16, pp. 5379-5384, 2010.

[31] Z. Song, T. Cai, J. C. Hanson, J. A. Rodriguez, and J. Hrbek, "Structure and Reactivity of Ru Nanoparticles Supported on Modified Graphite Surfaces: A Study of the Model Catalysts for Ammonia Synthesis," *Journal of the American Chemical Society,* vol. 126, pp. 8576-8584, 2004.

[32] G. Zhang, D.-Q. Yang, and E. Sacher, "Structure and Morphology of Co Nanoparticles Deposited onto Highly Oriented Pyrolytic Graphite," *Journal of Physical Chemistry C,* vol. 111, pp. 17200-17205, 2007.

[33] Y. Shao, G. Yin, and Y. Gao, "Understanding and approaches for the durability issues of Pt-based catalysts for PEM fuel cell," *Journal of Power Sources,* vol. 171, pp. 558-566, 2007.

[34] G. X. Wang, L. Yang, J. Z. Wang, H. K. Liu, and S. X. Dou, "Enhancement of Ionic Conductivity of PEO Based Polymer Electrolyte by the Addition of Nanosize Ceramic Powders," *Journal of Nanoscience and Nanotechnology,* vol. 5, pp. 1135-1140, 2005.

[35] J. Xie, D. L. Wood, K. L. More, P. Atanassov, and R. L. Borup, "Microstructural Changes of Membrane Electrode Assemblies during PEFC Durability Testing at High Humidity Conditions," *Journal of The Electrochemical Society,* vol. 152, pp. A1011-A1020, 2005.

[36] E. Antolini, J. R. C. Salgado, and E. R. Gonzalez, "The stability of Pt–M (M = first row transition metal) alloy catalysts and its effect on the activity in low temperature fuel cells: A literature review and tests on a Pt–Co catalyst," *Journal of Power Sources,* vol. 160, pp. 957-968, 2006.

[37] H. A. Gasteiger, S. S. Kocha, B. Sompalli, and F. T. Wagner, "Activity benchmarks and requirements for Pt, Pt-alloy, and non-Pt oxygen reduction catalysts for PEMFCs," *Applied Catalysis B: Environmental,* vol. 56, pp. 9-35, 2005.

[38] P. Waszczuk, A. Wieckowski, P. Zelenay, S. Gottesfeld, C. Coutanceau, J. M. Léger, *et al.,* "Adsorption of CO poison on fuel cell nanoparticle electrodes from methanol solutions: a radioactive labeling study," *Journal of Electroanalytical Chemistry,* vol. 511, pp. 55-64, 2001.

[39] G.-H. An, E.-H. Lee, and H.-J. Ahn, "Ruthenium and ruthenium oxide nanofiber supports for enhanced activity of platinum electrocatalysts in the methanol oxidation reaction," *Physical Chemistry Chemical Physics,* vol. 18, pp. 14859-14866, 2016.

[40] M. Rahsepar and H. Kim, "Microwave-assisted synthesis and characterization of bimetallic PtRu alloy nanoparticles supported on carbon nanotubes," *Journal of Alloys and Compounds,* vol. 649, pp. 1323-1328, 2015.

[41] J.-L. Mi, P. Norby, M. Bremholm, J. Becker, and B. B. Iversen, "The formation mechanism of bimetallic PtRu alloy nanoparticles in solvothermal synthesis," *Nanoscale,* vol. 7, pp. 16170-16174, 2015.

[42] E. N. El Sawy, H. A. El-Sayed, and V. I. Birss, "Clarifying the role of Ru in methanol oxidation at Rucore@Ptshell nanoparticles," *Physical Chemistry Chemical Physics,* vol. 17, pp. 27509-27519, 2015.

[43] Y.-C. Wei, C.-W. Liu, W.-J. Chang, and K.-W. Wang, "Promotion of Pt–Ru/C catalysts driven by heat treated induced surface segregation for methanol oxidation reaction," *Journal of Alloys and Compounds,* vol. 509, pp. 535-541, 2011.

[44] Z. Yang, S. Pedireddy, H. K. Lee, Y. Liu, W. W. Tjiu, I. Y. Phang*, et al.*, "Manipulating the d-Band Electronic Structure of Platinum-Functionalized Nanoporous Gold Bowls: Synergistic Intermetallic Interactions Enhance Catalysis," *Chemistry of Materials,* vol. 28, pp. 5080-5086, 2016.

[45] W. T. Cahyanto, W. Widanarto, M. Effendi, and H. Kasai, "Stability of atomic oxygen chemisorption on Pt-alloy surfaces," *Surface and Interface Analysis,* vol. 48, pp. 181-185, 2016.

[46] Y. Ishikawa, M.-S. Liao, and C. R. Cabrera, "Oxidation of methanol on platinum, ruthenium and mixed Pt–M metals (M=Ru, Sn): a theoretical study," *Surface Science,* vol. 463, pp. 66-80, 2000.

[47] Y. Zhang, Y. Wang, L. Bian, R. Lu, and J. Zang, "Functional separation of oxidation–reduction reactions and electron transport in PtRu/ND and conductive additive hybrid electrocatalysts during methanol oxidation," *Applied Surface Science,* vol. 364, pp. 645-650, 2016.

[48] E. Antolini and F. Cardellini, "Formation of carbon supported PtRu alloys: an XRD analysis," *Journal of Alloys and Compounds,* vol. 315, pp. 118-122, 2001.

[49] S.-Y. Huang, S.-M. Chang, and C.-t. Yeh, "Characterization of Surface Composition of Platinum and Ruthenium Nanoalloys Dispersed on Active Carbon," *The Journal of Physical Chemistry B,* vol. 110, pp. 234-239, 2005.

[50] M. Ramos, A. E. Martínez, and H. F. Busnengo, "Dissociative Adsorption of H2 on PtRu Bimetallic Surfaces," *The Journal of Physical Chemistry C,* vol. 120, pp. 7201-7212, 2016.

[51] L. Catherine, "Deposition-Precipitation Synthesis of Supported Metal Catalysts," in *Catalyst Preparation*, ed: CRC Press, 2006, pp. 319-339.

[52] E. S. Steigerwalt, G. A. Deluga, and C. M. Lukehart, "Pt−Ru/Carbon Fiber Nanocomposites: Synthesis, Characterization, and Performance as Anode Catalysts of

Direct Methanol Fuel Cells. A Search for Exceptional Performance," *The Journal of Physical Chemistry B*, vol. 106, pp. 760-766, 2002.

[53] J.-H. Choi, K.-W. Park, B.-K. Kwon, and Y.-E. Sung, "Methanol Oxidation on Pt/Ru, Pt/Ni, and Pt/Ru/Ni Anode Electrocatalysts at Different Temperatures for DMFCs," *Journal of The Electrochemical Society*, vol. 150, pp. A973-A978, 2003.

[54] T. Iwasita, H. Hoster, A. John-Anacker, W. F. Lin, and W. Vielstich, "Methanol Oxidation on PtRu Electrodes. Influence of Surface Structure and Pt−Ru Atom Distribution," *Langmuir*, vol. 16, pp. 522-529, 2000.

[55] A. Rockett, "Physical Vapor Deposition," in *The Materials Science of Semiconductors*, ed Boston, MA: Springer US, 2008, Chapter 11, pp. 505-572.

[56] D. M. Mattox, "Physical vapor deposition (PVD) processes," *Metal Finishing*, vol. 99, pp. 409-423, 2001.

[57] Electron Beam Evaporation by MIDWEST TUNGSTEN SERVICE [Online]. Available: http://www.tungsten.com/wp-content/uploads/2014/03/tipsbeam.pdf

[58] Website of University of Texas at El Paso, Fabrication Techniques [Online]. Available: http://wwwold.ece.utep.edu/research/webedl/cdte/Fabrication/

[59] M. Salmeron and R. Schlögl, "Ambient pressure photoelectron spectroscopy: A new tool for surface science and nanotechnology," *Surface Science Reports*, vol. 63, pp. 169-199, 2008.

[60] N. H. Turner and J. A. Schreifels, "Surface Analysis: X-ray Photoelectron Spectroscopy and Auger Electron Spectroscopy," *Analytical Chemistry*, vol. 66, pp. 163R-185R, 1994.

[61] D. Briggs, *Surface Analysis of Polymers by XPS and Static SIMS*. Cambridge: Cambridge University Press, 1998, chapter 2.

[62] M. Shafer. Lecture notes on Surface Chemical Shifts by XPS [Online]. Available: http://www.cem.msu.edu/~cem924sg/MikeShafer.pdf

[63] D. Briggs and J. T. Grant, "Surface analysis by Auger and x-ray photoelectron spectroscopy," ed Chichester, UK: IMPublications, 2003, chapter 1.

[64] H. N. Russell and F. A. Saunders, "New Regularities in the Spectra of the Alkaline Earths," *Astrophysical Journal*, vol. 61, p. 38, 1925.

[65] D. A. Shirley, "High-Resolution X-Ray Photoemission Spectrum of the Valence Bands of Gold," *Physical Review B*, vol. 5, pp. 4709-4714, 1972.

[66] M. P. Seah and M. T. Brown, "Validation and accuracy of software for peak synthesis in XPS," *Journal of Electron Spectroscopy and Related Phenomena*, vol. 95, pp. 71-93, 1998.

[67] CasaXPS. A note on X-ray Photoelectron Spectroscopy Spectra [Online]. Available: http://www.casaxps.com/help_manual/manual_updates/xps_spectra.pdf

[68] E. Sacher, "Asymmetries in Transition Metal XPS Spectra: Metal Nanoparticle Structure, and Interaction with the Graphene-Structured Substrate Surface," *Langmuir*, vol. 26, pp. 3807-3814, 2009.

[69] D.-Q. Yang and E. Sacher, "s–p Hybridization in highly oriented pyrolytic graphite and its change on surface modification, as studied by X-ray photoelectron and Raman spectroscopies," *Surface Science*, vol. 504, pp. 125-137, 2002.

[70] G. Zhang, D.-Q. Yang, and E. Sacher, "X-ray Photoelectron Spectroscopic Analysis of Pt Nanoparticles on Highly Oriented Pyrolytic Graphite, Using Symmetric Component Line Shapes," *Journal of Physical Chemistry C*, vol. 111, pp. 565-570, 2007/01/01 2006.

[71] L. Chen, A. Yelon, and E. Sacher, "X-ray Photoelectron Spectroscopic Studies of Pd Nanoparticles Deposited onto Highly Oriented Pyrolytic Graphite: Interfacial Interaction, Spectral Asymmetry, and Size Determination," *Journal of Physical Chemistry C*, vol. 115, pp. 7896-7905, 2011.

[72] A. Rochefort, D.-Q. Yang, and E. Sacher, "Stabilization of platinum nanoparticles on graphene by non-invasive functionalization," *Carbon*, vol. 47, pp. 2233-2238, 2009.

[73] S. Doniach and M. Šunjić, "Many-electron singularity in X-ray photoemission and X-ray line spectra from metals," *Journal of Physics C: Solid State Physics*, vol. 3, pp. 285-291, 1970.

[74] D.-Q. Yang and E. Sacher, "Carbon 1s X-ray Photoemission Line Shape Analysis of Highly Oriented Pyrolytic Graphite: The Influence of Structural Damage on Peak Asymmetry," *Langmuir*, vol. 22, pp. 860-862, 2006.

[75] M. K. McManus, Memoire de Maitrise. M.Sc. Thesis, University of Montreal, 1992, Chapter 3.4.

[76] Website of Physical Electronics: A Division of ULVAC-PHI [Online]. Available: https://www.phi.com/surface-analysis-techniques/tof-sims.html

[77] ionTOF. A note on Time-of-Flight Secondary Ion Mass Spectrometry [Online]. Available: https://www.iontof.com/tof-sims-secondary-ion-mass-spectrometry.html

[78] D. W. Mogk. Website of Geochemical Instrumentation and Analysis [Online]. Available: http://serc.carleton.edu/research_education/geochemsheets/techniques/ToFSIMS.html

[79] J. P. Hofmann, M. Rohnke, and B. M. Weckhuysen, "Recent advances in secondary ion mass spectrometry of solid acid catalysts: large zeolite crystals under bombardment," *Physical Chemistry Chemical Physics*, vol. 16, pp. 5465-5474, 2014.

[80] D. B. Williams and B. C. Carter, "Transmission Electron Microscopy - A Textbook for Material Science," ed: Springer, 2009, Chapters 1 and 11.

[81] JEOL. A note on Field Emission Transission Electron Microscopy [Online]. Available: http://www.jeol.de/electronoptics-en/products/electron-and-ion-optics/transmission-electron-microscopes/200-kv-tem-feg-tem/jem-2100f.php

[82] Wikipedia on Energy-dispersive X-ray Spectroscopy [Online]. Available: https://en.wikipedia.org/wiki/Energy-dispersive_X-ray_spectroscopy

[83] Website of MyScope: training for advanced research [Online]. Available: http://li155-94.members.linode.com/myscope/tem/introduction/

[84] Website of FEI: A Note on An Introduction to Electron Microscopy - The Scanning Transmission Electron Microscope [Online]. Available: https://www.fei.com/introduction-to-electron-microscopy/stem/

[85] S. J. Pennycook and P. D. Nellist, "Scanning Transmission Electron Microscopy: Imaging and Analysis," ed New York: Springer 2011, Chapters 1 and 2.

[86] S. Utsunomiya and R. C. Ewing, "Application of High-Angle Annular Dark Field Scanning Transmission Electron Microscopy, Scanning Transmission Electron Microscopy-Energy Dispersive X-ray Spectrometry, and Energy-Filtered Transmission Electron Microscopy to the Characterization of Nanoparticles in the Environment," *Environmental Science & Technology,* vol. 37, pp. 786-791, 2003.

[87] M. T. Otten, "High-Angle annular dark-field imaging on a tem/stem system," *Journal of Electron Microscopy Technique,* vol. 17, pp. 221-230, 1991.

[88] F. Hofer, F. P. Schmidt, W. Grogger, and G. Kothleitner, "Fundamentals of electron energy-loss spectroscopy," *IOP Conference Series: Materials Science and Engineering,* vol. 109, p. 012007, 2016.

[89] E. Ray, "Electron energy-loss spectroscopy," *Physics World,* vol. 10, p. 47, 1997.

[90] Gatan. A note on Energy Electron Loss Spectroscopy [Online]. Available: http://www.eels.info/about/overview

[91] The ImageJ Features Online, http://imagej.nih.gov/ij/features.html, (accessed December 2014).

[92] J. Kibsgaard, J. V. Lauritsen, E. Lægsgaard, B. S. Clausen, H. Topsøe, and F. Besenbacher, "Cluster−Support Interactions and Morphology of MoS2 Nanoclusters in a Graphite-Supported Hydrotreating Model Catalyst," *Journal of the American Chemical Society,* vol. 128, pp. 13950-13958, 2006.

[93] M. Rohmer, F. Ghaleh, M. Aeschlimann, M. Bauer, and H. Hövel, "Mapping the femtosecond dynamics of supported clusters with nanometer resolution," *The European Physical Journal D,* vol. 45, pp. 491-499, 2007.

[94] B. Hinnemann, P. G. Moses, J. Bonde, K. P. Jørgensen, J. H. Nielsen, S. Horch, *et al.*, "Biomimetic Hydrogen Evolution: MoS2 Nanoparticles as Catalyst for Hydrogen Evolution," *Journal of the American Chemical Society,* vol. 127, pp. 5308-5309, 2005.

[95] D.-Q. Yang and E. Sacher, "Characterization and Oxidation of Fe Nanoparticles Deposited onto Highly Oriented Pyrolytic Graphite, Using X-ray Photoelectron Spectroscopy," *Journal of Physical Chemistry C,* vol. 113, pp. 6418-6425, 2009.

[96] C. J. Pelliccione, E. V. Timofeeva, J. P. Katsoudas, and C. U. Segre, "In Situ Ru K-Edge X-ray Absorption Spectroscopy Study of Methanol Oxidation Mechanisms on Model Submonolayer Ru on Pt Nanoparticle Electrocatalyst," *Journal of Physical Chemistry C,* vol. 117, pp. 18904-18912, 2013.

[97] S. Kim, K. Qadir, S. Jin, A. Satyanarayana Reddy, B. Seo, B. S. Mun, *et al.*, "Trend of catalytic activity of CO oxidation on Rh and Ru nanoparticles: Role of surface oxide," *Catalysis Today,* vol. 185, pp. 131-137, 2012.

[98] S. Lizzit, A. Baraldi, A. Groso, K. Reuter, M. Ganduglia-Pirovano, C. Stampfl, *et al.*, "Surface core-level shifts of clean and oxygen-covered Ru(0001)," *Physical Review B,* vol. 63, p. 205419, 2001.

[99] J. Weissenrieder, A. Mikkelsen, J. Andersen, P. Feibelman, and G. Held, "Experimental Evidence for a Partially Dissociated Water Bilayer on Ru{0001}," *Physical Review Letters,* vol. 93, p. 196102, 2004.

[100] P. Buffat and J.-P. Borel, "Size effect on the melting temperature of gold particles," *Phys. Rev. A,* vol. 13, pp. 2287-2298, 1976.

[101] T. Lin, J. Chen, H. Bi, D. Wan, F. Huang, X. Xie, *et al.*, "Facile and economical exfoliation of graphite for mass production of high-quality graphene sheets," *Journal of Materials Chemistry A,* vol. 1, pp. 500-504, 2013.

[102] D. W. Pashley, M. J. Stowell, M. H. Jacobs, and T. J. Law, "The growth and structure of gold and silver deposits formed by evaporation inside an electron microscope," *Philosophical Magazine,* vol. 10, pp. 127-158, 1964.

[103] M. José-Yacamán, C. Gutierrez-Wing, M. Miki, D.-Q. Yang, K. N. Piyakis, and E. Sacher, "Surface Diffusion and Coalescence of Mobile Metal Nanoparticles," *Journal of Physical Chemistry B,* vol. 109, pp. 9703-9711, 2005.

[104] P. Datt, "Latent Heat of Vaporization/Condensation," in *Encyclopedia of Snow, Ice and Glaciers*, V. P. Singh, P. Singh, and U. K. Haritashya, Eds., ed Dordrecht: Springer Netherlands, 2011, pp. 703-703.

[105] D.-Q. Yang and E. Sacher, "Coalescence kinetics of copper clusters on highly oriented pyrolytic graphite and Dow Cyclotene, as determined by x-ray photoelectron spectroscopy," *Journal of Applied Physics,* vol. 90, pp. 4768-4771, 2001.

[106] D.-Q. Yang, K. N. Piyakis, and E. Sacher, "The manipulation of Cu cluster dimensions on highly oriented pyrolytic graphite surfaces by low energy ion beam irradiation," *Surface Science,* vol. 536, pp. 67-74, 6/20/ 2003.

[107] D. Q. Yang, M. Meunier, and E. Sacher, "The estimation of the average dimensions of deposited clusters from XPS emission intensity ratios," *Applied Surface Science,* vol. 173, pp. 134-139, 3/22/ 2001.

[108] B. Herd, J. C. Goritzka, and H. Over, "Room Temperature Oxidation of Ruthenium," *Journal of Physical Chemistry C,* vol. 117, pp. 15148-15154, 2013.

[109] F. A. Cotton and G. Wilkinson, "Advanced Inorganic Chemistry," 4th ed New York: Wiley, 1980, pp. 920-926.

[110] SciFinder Scholar, queried on 07/28/14, returned 15 references to the unbroken phrase, “mixed-valence ruthenium complexes”.

[111] S. Blomberg, R. Westerström, N. M. Martin, E. Lundgren, J. N. Andersen, M. E. Messing, *et al.*, "A high pressure X-ray photoelectron spectroscopy study of oxidation and reduction of Rh(100) and Rh nanoparticles," *Surface Science,* vol. 628, pp. 153-158, 2014.

[112] K. S. Kim and N. Winograd, "X-Ray photoelectron spectroscopic studies of ruthenium-oxygen surfaces," *Journal of Catalysis,* vol. 35, pp. 66-72, 1974.

[113] The NIST Index Online, http://webbook.nist.gov/cgi/cbook.cgi?ID=B1001896&Mask=800, (accessed December 2014).

[114] R. Kubo, "Electronic Properties of Metallic Fine Particles. I," *Journal of the Physical Society of Japan,* vol. 17, pp. 975-986, 1962.

[115] S. K. Ghosh, "Kubo Gap as a Factor Governing the Emergence of New Physicochemical Characteristics of the Small Metallic Particulates," *Assam Univ. J. Sci. Technol.: Phys. Sci. Technol,* vol. 7, pp. 114-121, 2011.

[116] V. Vijayakrishnan, A. Chainani, D. D. Sarma, and C. N. R. Rao, "Metal-insulator transitions in metal clusters: a high-energy spectroscopy study of palladium and silver clusters," *Journal of Physical Chemistry,* vol. 96, pp. 8679-8682, 1992.

[117] D.-Q. Yang and E. Sacher, "Initial- and final-state effects on metal cluster/substrate interactions, as determined by XPS: copper clusters on Dow Cyclotene and highly oriented pyrolytic graphite," *Applied Surface Science,* vol. 195, pp. 187-195, 2002.

[118] A. Liebsch, "Electronic Excitations at Metal Surfaces," ed: Springer, 1997, pp. 49-144.

[119] S. Dhara, B. Sundaravel, T. R. Ravindran, K. G. M. Nair, C. David, B. K. Panigrahi*, et al.*, ""Spillout" effect in gold nanoclusters embedded in c-Al2O3(0001) matrix," *Chemical Physics Letters,* vol. 399, pp. 354-358, 2004.

[120] J. Lermé, M. Pellarin, E. Cottancin, M. Gaudry, M. Broyer, N. Del Fatti*, et al.*, "Influence of lattice contraction on the optical properties and the electron dynamics in silver clusters," *The European Physical Journal D - Atomic, Molecular, Optical and Plasma Physics,* vol. 17, pp. 213-220, 2001.

[121] C. Liewhiran, N. Tamaekong, A. Wisitsoraat, and S. Phanichphant, "H2 Sensing Response of Flame-spray-made Ru/SnO2 Thick Films Fabricated from Spin-Coated Nanoparticles," *Sensors,* vol. 9, pp. 8996-9010, 2009.

[122] Y. Yang, C. Sun, Y. Ren, S. Hao, and D. Jiang, "New route toward building active ruthenium nanoparticles on ordered mesoporous carbons with extremely high stability," *Sci. Rep.,* vol. 4, 2014.

[123] B. Sun, P. Munroe, and G. Wang, "Ruthenium nanocrystals as cathode catalysts for lithium-oxygen batteries with a superior performance," *Sci. Rep.,* vol. 3, 2013.

[124] R. Bavand, A. Yelon, and E. Sacher, "X-ray photoelectron spectroscopic and morphologic studies of Ru nanoparticles deposited onto highly oriented pyrolytic graphite," *Applied Surface Science,* vol. 355, pp. 279-289, 2015.

[125] L. Chen, A. Yelon, and E. Sacher, "Formation of FePt Alloy Nanoparticles on Highly Oriented Pyrolytic Graphite: A Morphological and In Situ X-ray Photoelectron Spectroscopic Study," *Journal of Physical Chemistry C,* vol. 116, pp. 6902-6912, 2012.

[126] M. Kawasaki, C. N. Hsiao, J. R. Yang, and M. Shiojiri, "Structural investigation of Ru/Pt nanocomposite films prepared by plasma-enhanced atomic layer depositions," *Micron,* vol. 74, pp. 8-14, 2015.

[127] E. Lust, E. Härk, J. Nerut, and K. Vaarmets, "Pt and Pt–Ru catalysts for polymer electrolyte fuel cells deposited onto carbide derived carbon supports," *Electrochimica Acta,* vol. 101, pp. 130-141, 2013.

[128] S. Alayoglu, A. U. Nilekar, M. Mavrikakis, and B. Eichhorn, "Ru-Pt core-shell nanoparticles for preferential oxidation of carbon monoxide in hydrogen," *Nat Mater*, vol. 7, pp. 333-338, 2008.

[129] A. Christensen, A. V. Ruban, P. Stoltze, K. W. Jacobsen, H. L. Skriver, J. K. Nørskov, *et al.*, "Phase diagrams for surface alloys," *Physical Review B,* vol. 56, pp. 5822-5834, 1997.

[130] F. Calvo, "Thermodynamics of nanoalloys," *Physical Chemistry Chemical Physics,* vol. 17, pp. 27922-27939, 2015.

[131] P.-F. Paradis, "Thermophysical Properties of Platinum Group Metals in their Liquid Undercooled and Superheated Phases," *Johnson Matthey Technol. Rev.,* vol. 58, pp. 124-136, 2014.

[132] G. Zhang, S. Sun, M. I. Ionescu, H. Liu, Y. Zhong, R. Li, *et al.*, "Controlled Growth/Patterning of Ni Nanohoneycombs on Various Desired Substrates," *Langmuir,* vol. 26, pp. 4346-4350, 2010.

[133] M. S. Saha, R. Li, X. Sun, and S. Ye, "3-D composite electrodes for high performance PEM fuel cells composed of Pt supported on nitrogen-doped carbon nanotubes grown on carbon paper," *Electrochemistry Communications,* vol. 11, pp. 438-441, 2009.

[134] K. Zhang, W. Yang, C. Ma, Y. Wang, C. Sun, Y. Chen, *et al.*, "A highly active, stable and synergistic Pt nanoparticles/Mo2C nanotube catalyst for methanol electro-oxidation," *NPG Asia Mater,* vol. 7, p. e153, 2015.

[135] E. I. Santiago, M. S. Batista, E. M. Assaf, and E. A. Ticianelli, "Mechanism of CO Tolerance on Molybdenum-Based Electrocatalysts for PEMFC," *Journal of The Electrochemical Society,* vol. 151, pp. A944-A949, 2004.

[136] N. Tsiouvaras, M. A. Peña, J. L. G. Fierro, E. Pastor, and M. V. Martínez-Huerta, "The effect of the Mo precursor on the nanostructure and activity of PtRuMo electrocatalysts for proton exchange membrane fuel cells," *Catalysis Today,* vol. 158, pp. 12-21, 2010.

[137] S. Mukerjee, S. J. Lee, E. A. Ticianelli, J. McBreen, B. N. Grgur, Markovic, N. M., *et al.*, "Investigation of Enhanced CO Tolerance in Proton Exchange Membrane Fuel Cells by Carbon Supported PtMo Alloy Catalyst," *Electrochemical and Solid-State Letters,* vol. 2, pp. 12-15, 1999.

[138] N. Tsiouvaras, M. V. Martínez-Huerta, O. Paschos, U. Stimming, J. L. G. Fierro, and M. A. Peña, "PtRuMo/C catalysts for direct methanol fuel cells: Effect of the pretreatment on the structural characteristics and methanol electrooxidation," *International Journal of Hydrogen Energy,* vol. 35, pp. 11478-11488, 2010.

[139] M. V. Martínez-Huerta, N. Tsiouvaras, M. A. Peña, J. L. G. Fierro, J. L. Rodríguez, and E. Pastor, "Electrochemical activation of nanostructured carbon-supported PtRuMo electrocatalyst for methanol oxidation," *Electrochimica Acta,* vol. 55, pp. 7634-7642, 2010.

[140] F. Alcaide, G. Álvarez, N. Tsiouvaras, M. A. Peña, J. L. G. Fierro, and M. V. Martínez-Huerta, "Electrooxidation of H2/CO on carbon-supported PtRu-MoOx nanoparticles for polymer electrolyte fuel cells," *International Journal of Hydrogen Energy,* vol. 36, pp. 14590-14598, 2011.